Development of a Novel Method to Estimate Kinetic Micro-Parameters in Dynamic Whole-Body PET Imaging Protocols

by

Kyung-Nam Lee

B.Sc. in Physics, Yonsei University, 2007

A THESIS SUBMITTED IN PARTIAL FULLFILLMENT OF
THE REQUIREMENTS FOR THE DEGREE OF

MASTER OF SCIENCE

in

The Faculty of Graduate and Postdoctoral Studies

(Medical Physics)

THE UNIVERSITY OF BRITISH COLUMBIA
(Vancouver)
August 2023

The following individuals certify that they have read, and recommend to the Faculty of Graduate and Postdoctoral Studies for acceptance, the thesis entitled:

Development of a Novel Method to Estimate Kinetic Micro-Parameters in Dynamic Whole-Body PET Imaging Protocols

Submitted by Kyung-Nam Lee in partial fulfillment of the requirements for

the degree of Master of Science

in Medical Physics

Examining Committee:

Carlos Uribe Munoz, Clinical Assistant Professor, Radiology, UBC
Co-Supervisor

Arman Rahmim, Professor, Physics and Astronomy, UBC
Co-supervisor

Abstract

For whole-body (WB) kinetic modeling based on a typical Positron Emission Tomography (PET) scanner, a multi-pass multi-bed scanning protocol is necessary because of the limited axial field of view. Such a protocol introduces loss of early dynamics in the time-activity curves (TACs) and sparsity in TAC measurements; thus inducing uncertainty in parameter estimation when using least squares estimation (LSE) (i.e., common standard), especially for kinetic micro-parameters.

To address the issue above, this thesis proposes a method that can estimate micro-parameters by building a reference TAC database, and selecting optimal parameters based on analysis of multiple aspects of the TACs, while in our assessment of performance compared to conventional methods we focus on general image qualities, overall visibility, and tumor detectability.

To achieve the research goal above, we developed a novel parameter estimation method called parameter combination-driven estimation (PCDE), which has two distinctive characteristics:1) improved capability of finding a correct correlation between early and late TACs at the cost of the resolution of the estimated parameter, and 2) exploitation of multiple aspects of TAC. To compare the general image quality between the two methods, we plotted tradeoff curves for the normalized bias (NBias) and the normalized standard deviation (NSD). We also evaluated the impact of different iteration numbers of the ordered-subset expectation maximization (OSEM) reconstruction algorithm on the tradeoff curves. In addition, for overall visibility, which is a measure of the capability of identifying suspicious lesions in WB (i.e., global inspection), the overall signal-to-noise ratio (SNR) and spatial noise ($NSD_{spatial}$) were calculated and compared. Furthermore, the contrast-to-noise ratio (CNR) and relative error of the tumor-to-background ratio (RE_{TBR}) were calculated to compare tumor detectability within a specific organ (i.e., local inspection).

Through the proposed method, the improved general image quality, overall visibility, and tumor detectability were verified in micro-parametric images with OSEM reconstructions. We expect our work to contribute to opening the door to use of a typical PET scanner to reliably estimate kinetic

micro-parameters in WB imaging, which has been so far very challenging owing to significant uncertainties in estimates when using LSE methods.

Lay Summary

We compared the performance of kinetic parameter estimation between the common standard, least squares estimation (LSE), and our proposed parameter combination-driven estimation (PCDE) method, focusing on general image quality, overall visibility, and tumor detectability. Significant improvements in micro-parameters estimates were demonstrated. PCDE can open the door to typical PET scanner-based WB kinetic modeling for kinetic micro-parameters, which has been so far very challenging owing to significant uncertainties in estimates when using LSE methods.

Preface

Chap. 1 covers the general overview of Nuclear Medicine Imaging.: 1) Nuclear Medicine, 2) Radioactive Decay, and 3) Interactions of Photons with Matter.

Chap. 2 introduces the Fundamentals of Kinetic Modeling so that the reader can be familiar with technical terminologies and basic assumptions/principles in kinetic modeling area, which would be practically helpful to understand our research performed during my Masters studies at here UBC. The sub-categories are as follows: 1) Rationale of Kinetic Modeling, 2) Brief Review of Current Kinetic Modeling Methodologies, 3) Necessity of Whole-Body Kinetic Modeling, and 4) Current Pitfalls and Challenges.

Chapter 3 and 4 represent original unpublished material that we are working to publish as journal papers. Parts of these works were presented in conferences:

1) K.N. Lee, C. Uribe, A. Rahmim
A Matlab-based kinetic modeling tool for fast and robust estimation of Patlak-based parameters with uncertainty information
Proc. Society of Nuclear Medicine & Molecular Imaging (SNMMI), Annual Meeting, 2022

2) K. N. Lee, A. Rahmim, C. Uribe
Novel kinetic micro-parameter estimation from dynamic whole-body PET images
Proc. Society of Nuclear Medicine & Molecular Imaging (SNMMI), Annual Meeting, 2023

For these works, I was responsible for designing the project, realization of ideas as a form of MATLAB code, performing validation and comparison study, and manuscript composition and writing. Dr. Carlos Uribe was research advisor and Dr. Arman Rahmim was academic advisor. They are the supervisory authors involved throughout the project by introducing kinetic modeling area to me.

Chap. 3 and 4 covers actual research contents performed for my Masters studies. A novel micro kinetic parameter estimation method is introduced and proposed by building a reference TAC

database and selecting optimal parameters based on analysis of multiple aspects of the TACs. The performance of parametric imaging via the proposed method was compared to a current common standard (i.e., least squares estimation), focusing on general image qualities, overall visibility, and tumor detectability. However, each chapter has a different focus as aspect as follows.: chap. 3: comparison study based on virtually simulated dataset, and chap. 4: comparison study based on actual patient dataset.

Chap. 5 briefly summarizes meaningful contributions of our research to a typical PET scanner-based kinetic modeling and discusses future studies that need to be performed in the near future.

In brief, this thesis covers introduction to nuclear medicine (i.e., chap. 1) and fundamentals of kinetic modeling (i.e., chap. 2), while main focus is to introduce and investigate a novel micro kinetic parameter estimation method for a typical PET scanner-based whole-body kinetic modeling and to propose the method for micro parametric imaging.

Table of Contents

List of Tables

List of Figures

List of Abbreviations

1TCM one-tissue compartment model

2D two-dimensional

2TCM two-tissue compartment model

3D three-dimensional

4D four-dimensional

AC attenuation correction

AUC area under the curve

BW body weight

CNR contrast-to-noise ratio

CT computed tomography

CV coefficient of variation

$d_{PETSTEP}$ dynamic PET simulator of tracer via emission projection

FBP filtered back-projection

FDG fluoredeoxyglucose

FOV field of view

FT Fourier transform

GPU graphical processing unit

LOR line of response

LSE least squares estimation

MAP maximum a posteriori

MI mutual information

MLEM maximum likelihood expectation maximization

MRI magnetic resonance imaging

NBias normalized bias

NM nuclear medicine

NRMSE normalized root mean squared error

NSD normalized standard deviation

OSEM ordered-subset expectation maximization

PCDE parameter-combination driven estimation

PET positron emission tomography

PET/CT positron emission tomography integrated with computed tomography

PGA Patlak graphical analysis

PI post-injection

PMT photo-multiplier tube

PSF post-smoothing filter

PSMA prostate-specific membrane antigen

ROA ratio of overlapped area

ROI region of interest

RPT radiopharmaceutical therapy

SNR signal-to-noise ratio

SPECT single photon emission computed tomography

SSE sum of squared error

SSTR2 somatostatin receptor 2

SUV standardized uptake value

TAC time-activity curve

TBR tumor-to-background ratio

TSS total similarity score

WB whole-body

XCAT extended cardiac-torso

Acknowledgements

Most of all, I would like to thank my research advisor, Dr. Carlos Uribe, for the kind guidance throughout my M.Sc. years at UBC and BCCRC, and also my academic advisor, Dr. Arman Rahmim, for providing me the valuable opportunity to work with diverse types of researchers in the QURIT lab. Continuously exposing myself into different types of insights and perspectives was really great because it allowed me to better understand not only other scientists but also more importantly myself, which definitely was and will be consistently helpful for my continual growth as a scientist and person.

In addition, I would also like to thank many colleagues and senior scientists in our lab. Although we sometimes had a limited chance to discuss some scientific things, congenial and amicable environment in the lab from all of you enabled me to focus on my work well, a critical factor that can impact the performance of a researcher in the lab in the long run. Thank you all!

Last but not least, I sincerely wish the best for all of you! Further I wish everyone in the world could be able to recognize and appreciate others in an objective way, which could be realized by cultivating critical thinking power; I end by sharing the impressive quote below:

Don't worry about others not recognizing you; worry about me not recognizing others.

- Confucius -

Dedication

This thesis is dedicated to my loving parents and rest of my family members who always believe and support my decision in a positive way.

Chapter 1. Introduction

1.1. General Overview of Nuclear Medicine Imaging

1.1.1. Nuclear Medicine

Nuclear medicine (NM) is a medical specialty that exploits radioisotopes for diagnostic and/or therapeutic purpose[1–5]. To achieve this, compounds labeled with radionuclides (e.g., ^{18}F, ^{68}Ga, ^{177}Lu, et al.), known as radiopharmaceuticals, are introduced into the patient via an injection or oral administration.

Diagnostic imaging takes advantage of the radioactive decay of the radionuclides that emit gamma rays either in a direct or indirect way. These gammas must have enough energy to exit the patient's body. By equipping with gamma detectors around the patient, it is possible to quantitatively measure the emitted photons and generate images of the distribution of the radiotracer within the patient, either in a static (i.e., distribution at a single time point) or dynamic (i.e., distributions as a function of time) way[1].

NM has two main modalities for imaging:

1) Single Photon Imaging[6–11]

Some radionuclides emit only one gamma when they decay. If images are generated using those individual photons, the modality is known as single photon imaging. If two-dimensional (2D) images are generated, the method is called scintigraphy or planar imaging. This is done by placing the detector in one position near the patient. If tomographic imaging (i.e. three-dimensional (3D)) is used, it is called single photon emission computed tomography (SPECT) in which several planar views obtained at different positions (i.e., multiple angles) around the patient are combined to form a 3D image. Compared to 2D planar images, SPECT images are advantageous because they provide depth information with better contrast, and importantly it does not contain overlapping organs, which makes it better suited for diagnosis and dosimetry[1].

2) Positron Imaging[12–16]

The technique uses radiotracers that emit a positron when decaying (i.e., positron emitter). The positron annihilates with a nearby electron, which creates two annihilation photons (i.e., 511 keV) traveling almost completely opposite directions. These photons are detected at different angles around the patient, and tomographic images are generated in 3D. It is called as positron emission tomography (PET).

Compared to other medical imaging modalities that can provide anatomical information such as magnetic resonance imaging (MRI)[17–21] or computed tomography (CT)[22–25] with X-ray, NM imaging can provide biological/physiological information of tissues at the molecular level (i.e. nano-molar concentrations of the radiopharmaceutical); an advantage of NM imaging[1]. Table 1-1 shows some examples of clinical use of nuclear medicine imaging.

Table 1- 1. Selected clinical nuclear medicine procedures (cited from table 1-1[1] in Cherry SR, Sorenson JA, Phelps ME. *Physics in Nuclear Medicine*. 4th ed. Elsevier/Saunders; 2012).

Radiopharmaceuticals	Imaging	Measurement	Examples of Clinical Use
^{99m}Tc-MDP	Planar	Bone metabolism	Metastatic spread of cancer, osteomyelitis vs. cellulitis
^{99m}Tc-sestamibi (Cardiolite) ^{99m}Tc-tetrofosmin (Myoview) ^{99m}Tc-thallous chloride	SPECT or planar	Myocardial perfusion	Coronary artery disease
^{99m}Tc-MAG3 ^{99m}Tc-DTPA	Planar	Renal function	Kidney disease
^{99m}Tc-HMPAO (Ceretec)	SPECT	Cerebral blood flow	Neurologic disorders
^{99m}Tc-ECD	SPECT	Cerebral blood flow	Neurologic disorders
^{123}I-sodium iodide ^{131}I-sodium iodide	Planar	Thyroid function	Thyroid disorders Thyroid cancer
^{67}Ga-gallium citrate	Planar	Sequestered in tumors	Tumor localization
^{99m}Tc-macroaggregated albumin and ^{138}Xe gas	Planar	Lung perfusion/ventilation	Pulmonary embolism
^{111}In-labeled white blood cells	Planar	Sites of infection	Detection of inflammation

^{18}F-fluorodeoxyglucose	PET	Glucose metabolism	Cancer, neurological disorders, and myocardial diseases
^{82}Rb-rubidium chloride	PET	Myocardial perfusion	Coronary artery disease

MDP, methylene diphosphonate; MAG3, mercapto-acetyl-triglycine; DTPA, diethylenetriaminepenta-acetic acid; HMPAO, hexamethylpropyleneamine oxime; ECD, ethyl-cysteine-dimer, SPECT, single photon emission computed tomography; PET, positron emission tomography.

1.1.2. Radioactive Decay

A radioactive isotope has an unstable nucleus. The nucleus is comprised of a densely packed arrangement of protons and neutrons. By undergoing radioactive decay, the nucleus changes its composition and moves to a more stable configuration.

The decay process follows an exponential law as follows.

$$\mathrm{A(t)} = A_0 \cdot e^{-\lambda \cdot t} = A_0 \cdot e^{-\frac{ln2}{t_{\frac{1}{2}}} \cdot t} \tag{1.1}$$

where A_0, λ, and $t_{1/2}$ denote initial activity, decay constant, and half-life, respectively. The activity denotes the number of nuclei that decay per unit of time. The SI is the Becquerel (i.e., $1\mathrm{Bq} = 1\ \mathrm{decay/sec}$) but the Curie (i.e., $1\mathrm{Ci} = 3.7 \times 10^{10}\ decays/sec$) has also been commonly used. The relation between the two is $1\mathrm{mCi} = 37\mathrm{MBq}$[1].

Depending on which particle is emitted by a decay, the decay can be categorized into three modes.: 1) Alpha decay, 2) Beta decay, or 3) Gamma decay.

1) Alpha (α) decay

Ernest Rutherford found that some heavy nuclei were emitting particles that did not penetrate deep in materials and were positively charged. Later it was identified as a Helium nucleus, which is also known as an alpha particle. The alpha decay follows the equation below.

$${}^{A}_{Z}X_N \rightarrow {}^{A-4}_{Z-2}Y_{N-2} + {}^{4}_{2}He_2$$

where X and Y denote the symbols of the element shown in the periodic table, respectively, and Z, A, and N represent atomic number, mass number (i.e. sum of neutrons and protons), and the number of neutrons, respectively[1–3].

2) Beta decay

This type of decay is the most common and can be categorized into two sub-types: β^- decay and β^+ decay, as we discuss next.

2-1) β^- decay

One of the neutrons in the nucleus is transformed into a proton, and a β^- particle and an antineutrino are ejected as follows.

$$\mathrm{n} \rightarrow \mathrm{p} + \beta^- + \overline{\nu_e}$$

where n, p, and $\overline{\nu_e}$ denote a neutron, proton, and antineutrino, respectively.

It should be noted that β^- energy spectrum from the decay is continuous because the available energy is split between the β^- and antineutrino[1].

2-2) β^+ decay

In this case, one proton in the nucleus is transformed into a neutron. A positron β^+ and a neutrino are ejected as follows.

$$\mathrm{p} \rightarrow \mathrm{n} + \beta^+ + \nu_e$$

where n, p, and ν_e denote a neutron, proton, and neutrino, respectively.

PET imaging takes advantage of this type of decay[1]. Once the isotope emits the positron through β^+decay, the positron interacts with the surrounding media and at the end of its path it annihilates with an atomic electron. The average positron range in a material depends on the positron's energy

and medium characteristics (e.g., mass density, electron density, atomic number, et al.), but for ^{18}F the ranges are quite short.; the average kinetic energy and its range (i.e., continuously slowing down approximation) is 250 keV and 0.62 mm, respectively[26].

In the annihilation, the masses of electron and positron are converted into energy and produce a pair of 511 keV photons traveling in opposite directions to each other (i.e., Figure 1-1). The 511 keV photon energy comes from Einstein's mass-energy equivalence principle "" (i.e., $E = mc^2$), where m is the mass of the electron or positron and c is the speed of light in a vacuum (i.e., $c \approx 3 \times 10^8 \ m/s$). Importantly, the two annihilation photons are what are detected and used to form images of the radioisotope's activity/concentration in the human body or phantom.

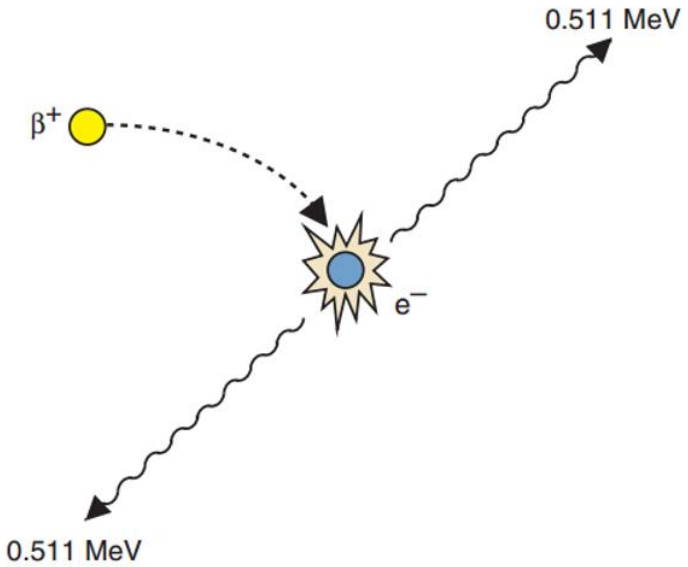

Figure 1- 1. Schematic representation of annihilation reaction between a positron and electron. A pair of 0.511 MeV annihilation photons are emitted "back-to-back" at 180 degrees to each other (cited from figure 3-7[1] in Cherry SR, Sorenson JA, Phelps ME. *Physics in Nuclear Medicine*. 4th ed. Elsevier/Saunders; 2012).

2-3) Electron Capture

Electron capture is a process that competes with β^+decay. In the process, an electron from an inner atomic shell is captured by the nucleus, and a proton is transformed into a neutron and a neutrino is emitted from the nucleus as follows.

$$\mathrm{p} + \beta^- \rightarrow \mathrm{n} + \nu_e$$

where n, p, and ν_e denote a neutron, proton, and neutrino, respectively.

Although the parent nucleus follows the similar transmutation as in the β^+decay, this type of decay is only allowed if the mass of the parent is greater than the mass of the daughter plus the electron ionization energy. Once the electron is captured by a proton, another electron from an outer shell fills the gap and thus emits a photon (i.e., characteristic X-ray), or the energy is used to emit another orbital electron (i.e., Auger electron).

3) Gamma (γ) decay

In this type of decay, a nucleus is in an excited state and releases some of its energy by emitting electromagnetic radiation. This decay is not a transmutation (i.e. the atomic element does not change) and it follows the equation below.

$${}^{A}_{Z}X^* \rightarrow {}^{A}_{Z}X + \gamma$$

where X^* denotes the excited state of a nucleus.

A process competing with γ emission is the emission of a conversion electron. In the process, the excited nucleus can also interact with an electron of the atom and the energy can be released by ejecting an electron rather than emitting a photon, which is called as internal conversion.

1.1.3. Interactions of Photons with Matter

1) Coherent Scattering

Coherent or Rayleigh scattering is a type of scattering interaction that occurs between a photon and an atom as a whole[1–3]. By coherent scattering, the photon is deflected with essentially no loss of energy. This type of interaction is important only at relatively low energies (e.g., $\ll 50$ keV). It can be significant in some precise photon transmission measurements such as X-ray crystallography. However, since it is not an effective mechanism for transferring photon energy to matter, it is of little practical importance in nuclear medicine.

2) Photoelectric Effect

The photoelectric effect is an atomic absorption process in which an atom absorbs totally the energy of an incident photon as follows[1–3].

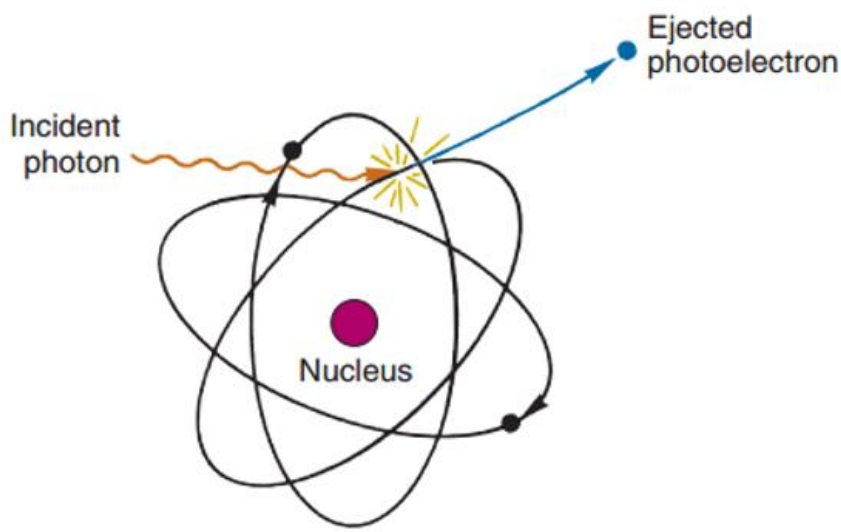

Figure 1- 2. Schematic representation of the photoelectric effect. The incident photon transfers its energy to a photoelectron and disappears (cited from figure 6-11[1] in Cherry SR, Sorenson JA, Phelps ME. *Physics in Nuclear Medicine*. 4th ed. Elsevier/Saunders; 2012.).

The photon disappears and the energy absorbed is used to eject an orbital electron from the atom, which is called a photoelectron. Its kinetic energy E_{pe} is equal to the difference between the incident photon energy E_0 and the binding energy of the electron shell from which it was ejected, as follows.

$$E_{pe} = E_0 - E_B \tag{1.2}$$

where E_{pe}, E_0, and E_B denote the kinetic energy of the photoelectron, initial incident photon energy, and the binding energy of the electron shell.

Photoelectrons cannot be ejected from an electron shell unless the incident photon energy exceeds the binding energy of that shell. If sufficient photon energy is available, the photoelectron is most likely to be ejected from the innermost possible shell, rather than outmost shell. The photoelectric effect generates a vacancy in an orbital electron shell, which results in the emission of characteristic X-ray or Auger electron.

3) Compton Scattering

Compton scattering is an interaction between a photon and a loosely bound orbital electron of an atom (i.e. an electron in the outer shells)[1–3]. In Compton scattering, since the incident photon energy greatly exceeds the binding energy of the electron shell, it can be assumed that the interaction between a photon and a free electron, as follows.

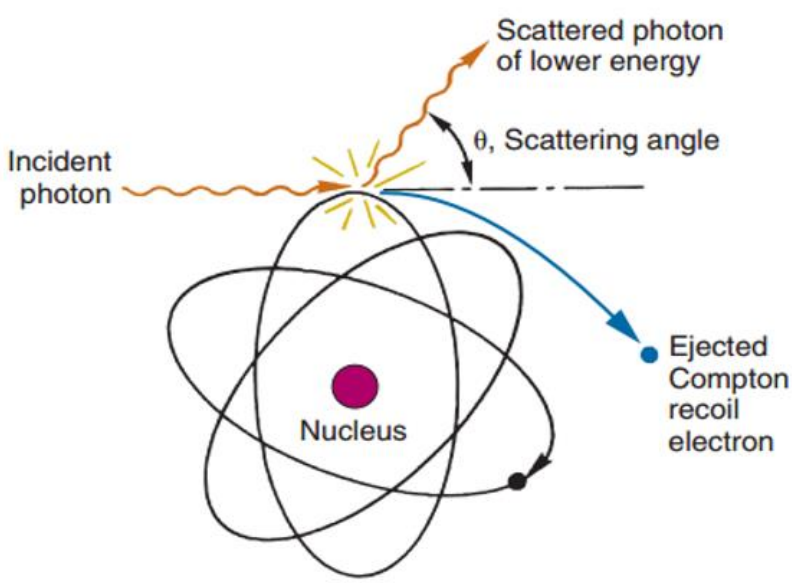

Figure 1- 3. Schematic representation of Compton scattering. The incident photon transfers part of its energy to a Compton recoil electron and is scattered in another direction of travel (cited

from figure 6-12[1] in Cherry SR, Sorenson JA, Phelps ME. *Physics in Nuclear Medicine*. 4th ed. Elsevier/Saunders; 2012.).

Contrary to photoelectric effect, here, the photon does not disappear and instead it is deflected through a scattering angle θ with lower energy compared to the incident energy. Part of energy is transferred electron. The relationship between the scattering angle θ and the energy of scattered photon is below.

$$E_{sc} = \frac{E_0}{1 + \frac{E_0}{m_e c^2}(1 - cos\theta)} \tag{1.3}$$

where E_{sc} and E_0 denote the energy of scattered photon and initial incident photon energy, respectively, and m_e and c represent the mass of electron (i.e., $m_e \approx 9.11 \times 10^{-31} kg$) and the speed of light (i.e., $c \approx 3 \times 10^8 m/s$) in vacuum, respectively.

By conservation of energy, the energy of the electron can be derived as follows.

$$E_{re} = E_0 - E_{sc} \tag{1.4}$$

where E_{re} denotes the energy of the recoil electron.

Because of the energy of the annihilation photon (i.e., 511 keV), the dominant interaction with the medium is through Compton scattering. This interaction ejects the electron from its atomic shell and the scattered photon now has a lower energy and deflected direction, compared to the original 511 keV photon. The nature of deflection is one of inherent factors to lower the detection efficiency of the annihilation photons originally generated.

Another important factor that lowers the detection efficiency is attenuation. The different interactions of photons in matter lead to an attenuation of the annihilation photons. The number of photons that are transmitted through the media decreases exponentially with increasing length of the material traversed.

The thickness of soft tissue required to reduce the intensity by one half is approximately 7 cm for 511 keV photons[27], and thus after ~14 cm of soft tissue the intensity would be reduced to one quarter of its original intensity. Hence, the attenuation is considered one of dominant factors that affect PET image quality, and thus should be corrected, especially for thicker patients.

4) Pair Production

Pair production occurs when a photon having a higher energy than the rest mass energy of a positron-electron pair (i.e., ≥ 1.022 MeV) interacts with an atomic nucleus[1–3]. In pair production, the photon disappears and its energy is used to create a positron-electron pair, as follows.

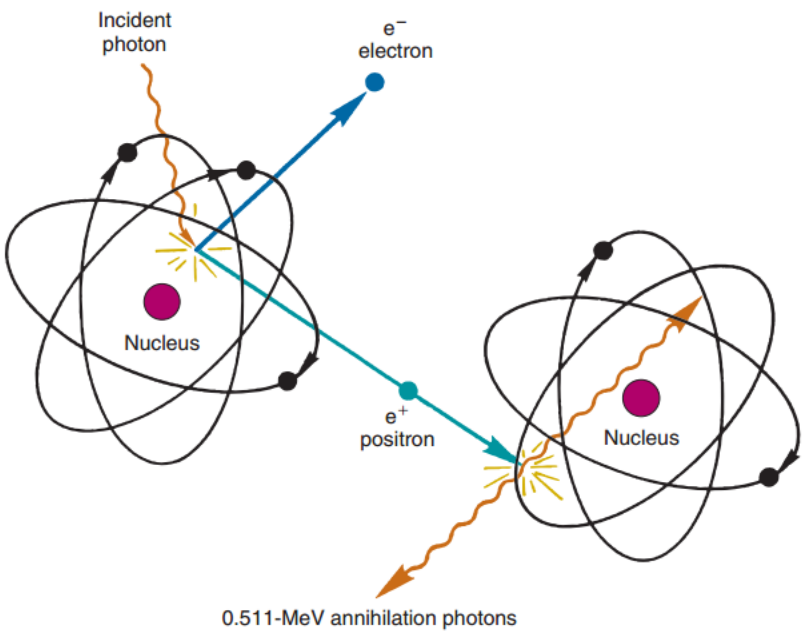

Figure 1- 4. Schematic representation of pair production. Energy of incident photon is converted into an electron and a positron (total 1.022 MeV mass-energy equivalent) plus their kinetic energy. The positron eventually undergoes mutual annihilation with a different electron, producing two 0.511 MeV annihilation photons (cited from figure 6-14[1] in Cherry SR, Sorenson JA, Phelps ME. *Physics in Nuclear Medicine*. 4th ed. Elsevier/Saunders; 2012.).

Since the positron and electron both have a rest mass equivalent to 0.511 MeV, a minimum photon energy of 1.022 MeV must be available for pair production to occur. The difference between the incident photon energy E_0 and the 1.022 MeV is transferred as kinetic energy to the positron and the electron as follows.

$$E_{e^+} + E_{e^-} = E_0 - 1.022 \ \ MeV \tag{1.5}$$

where E_{e^+} and E_{e^-} denote the kinetic energy of positron and electron, respectively.

1.2. PET Data Acquisition

1.2.1. Photon Detection and Scintillation Detectors

The general goal of photon detection is to measure the total energy deposited by the photon when it interacts in the detector (e.g., scintillator)[1–3]. In most PET scanners today, scintillation detectors are used. Whenever an interaction with the high energy photons (e.g., 511 keV photons) occurs, the scintillation crystal emits optical photons (i.e., ~eV photons), and thus the number of optical photons produced in the crystal is proportional to the energy deposited by the high energy photons.

Scintillation material (i.e., crystal) can be rated based on four characteristics.: 1) stopping power, 2) decay constant, 3) light output, and 4) energy resolution.

The stopping power is the energy loss of the high energy photon per unit length in the crystal. It depends on mass/electron density and effective atomic number of the material. Typically, the high stopping power is desirable because it would yield more intense interactions with high energy photons and thus a better efficiency for detecting them in the crystal of fixed size.

The decay constant represents how long the scintillation flash lasts in the crystal. Typically, higher decay constant is favorable because it allows for counting higher photon rates and lower background rates.

The light output denotes the number of optical photons produced by each incident high energy photon. When considering the statistical counting error (i.e., Poisson noise), higher output (i.e. higher number of emitted scintillator photons) is desirable for better spatial and energy resolution.

The energy resolution indicates the capability in differentiating each energy and can be quantified by measuring fluctuations in the energy measurement. Usually, the concept of full width at half-maximum is used to quantify the energy resolution of the device or system. In our application, it means the capability in distinguishing the annihilation photon (i.e., 511 keV) from Compton scattered photon (i.e., less than 511 keV). The resolution depends on the light output and intrinsic energy resolution of the crustal.

With the scintillator, the photo-multiplier tubes (PMTs) are commonly used as a set of detector system to convert the optical signal (i.e., optical photons from crystal) into electrical signal (i.e., electric current) and to amplify the signal using a photocathode and dynodes. Certainly, the resulting electric current is proportional to the number of initial optical photons and thus to the energy deposited in the crystal by the high energy photon.

By including many small PMTs, the location of the photon detection can be determined. To determine the interaction position of the annihilation photon from the spread-out scintillation photon signals, the relative signals from the PMTs are compared. Typically, a few millimeters of spatial resolution are possible. A full PET scanner consists of a cylindrical assembly of block detectors with multiple rings[27].

1.2.2. Sinogram

In the scanner, coincidence events are detected along their lines of response (LORs) between pairs of detector elements, and the set of projection profiles is defined as a sinogram[1–3]. Historically, the reason why it is called as sinogram is the fact that the shape of a set of projection profiles for an off-center point source is a sinusoid (i.e., Figure 1-5).

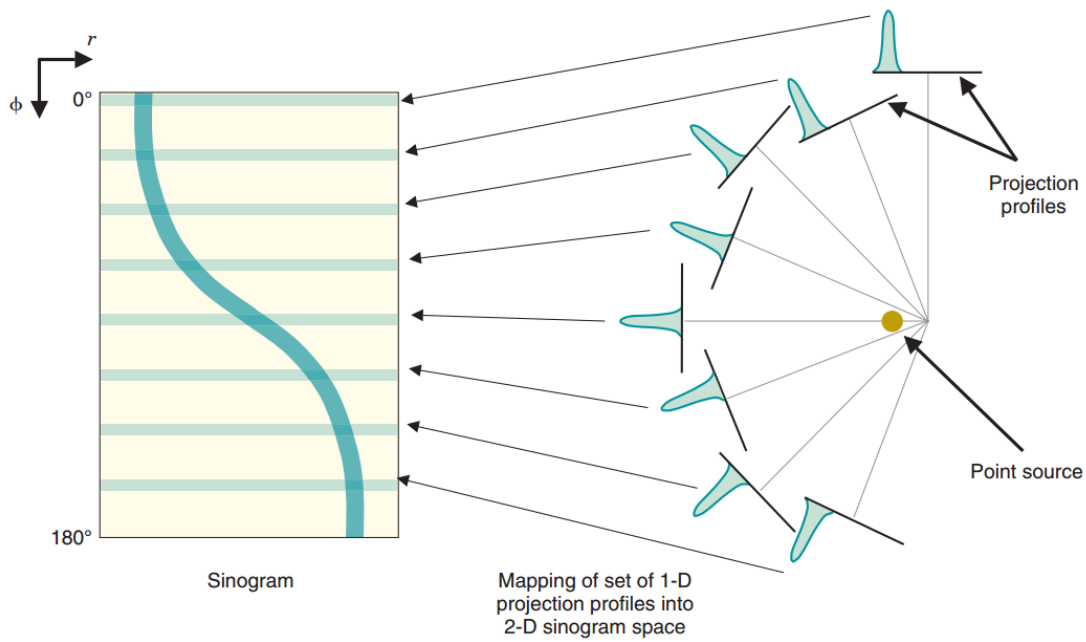

Figure 1- 5. Two-dimensional (2-D) intensity display of a set of projection profiles, known as a sonogram. Each row in the display corresponds to an individual projection profile, sequentially displayed from top to bottom. A point source of radioactivity traces out a sinusoidal path in the sinogram (cited from figure 16-4[1] in Cherry SR, Sorenson JA, Phelps ME. *Physics in Nuclear Medicine*. 4th ed. Elsevier/Saunders; 2012).

Since necessary corrections are typically performed at the sinogram-domain, rather than the image-domain, the formation of sinograms is an important step in PET data acquisition process.

1.2.3. Data Corrections

All measurements always come with errors caused by the image degrading effects like scatter and attenuation that have been discussed above. This means the PET data acquisition is not a perfect process. For instance, interactions in the patient will attenuate the number of emitted photons from the patient compared to the total number of annihilation photons generated from the source inside the body. Each detector element can have different detection efficiency, and random and scattered coincidences can be recorded along with the true coincidence events. These kind of effects need

to be corrected to extract clinically useful and quantitatively accurate information from PET images[1–3,27].

One of the most important corrections is attenuation correction (AC). Photons that travel denser materials on their path are more likely to be absorbed or scattered, compared to photons that travel less dense materials. If images are reconstructed without AC, the less dense areas (e.g., lung) can be shown as higher activity/concentration areas in PET images than surrounding denser tissue (e.g., mediastinum)[27].

To apply attenuation correction, it is necessary to determine the attenuation through the patient for all LORs. In these days, the acquired computed tomographic (CT) image is used for the attenuation correction to provide the attenuation coefficient information through the patient.

1.3. PET Image Reconstruction

The objective of quantitative PET imaging is to obtain the activity/concentration of radiotracers in the body. Once sinograms are acquired, the PET images can be generated by reconstruction process[1] (i.e., Figure 1-6).

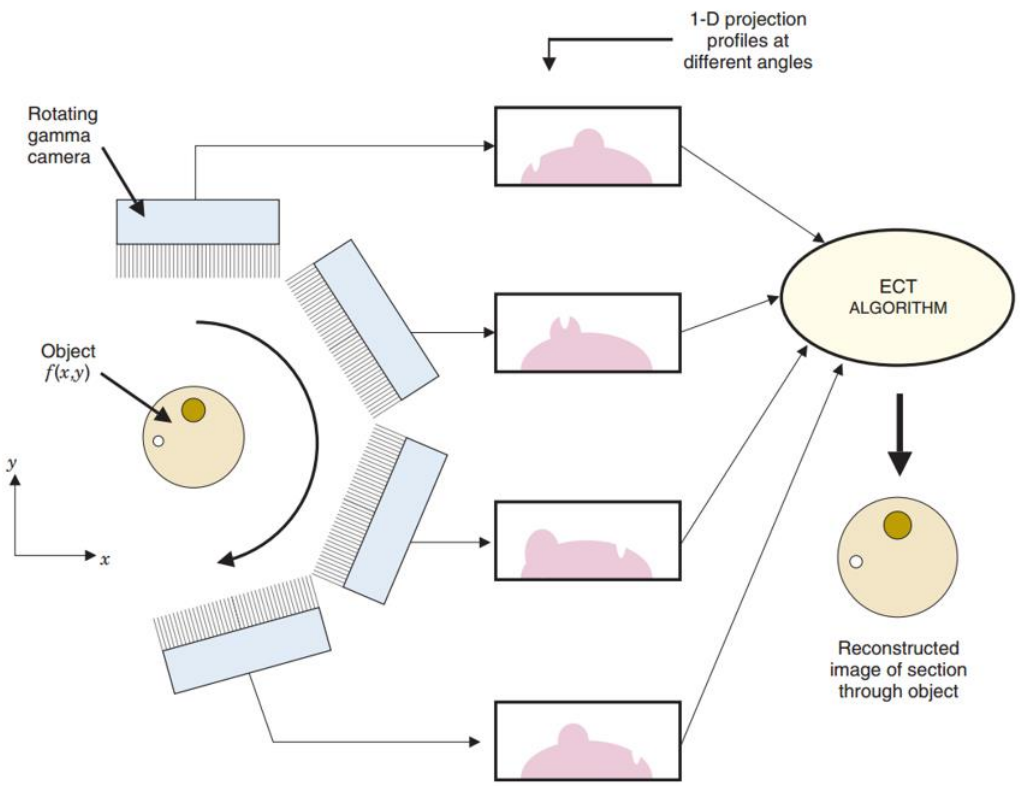

Figure 1- 6. Rotating the gamma camera around the object provides a set of one-dimensional projection profiles for a two-dimensional object, which are used to calculate the two-dimensional distribution of radioactivity in the object. ECT: emission computed tomography (cited from figure 16-2[1] in Cherry SR, Sorenson JA, Phelps ME. *Physics in Nuclear Medicine*. 4th ed. Elsevier/Saunders; 2012).

There are two types of reconstruction algorithms: 1) analytic, and 2) iterative reconstructions[1–3].

Analytic methods reconstruct PET images by applying inverse transform (e.g., inverse radon transform) to the projection data (i.e., sinogram). Iterative methods, on the other hand, acquires improved image estimates by updating the estimates iteratively. The estimates can be updated using a statistical model of the coincidence events acquisition process. Iterative algorithms do not necessarily assume the line-integral model, and enable modeling of statistical noise, non-uniform resolution, positron range, and other physical effects directly in the image reconstruction process. More details of representative methods for each type will be followed. Here, only most widely

used algorithms for each type will be discussed.: 1) Filtered Back-Projection as an analytic method, and 2) Ordered-Subset Expectation Maximization as an iterative method.

1.3.1. Filtered Back-Projection (FBP)

The FBP can be easily understood through a simple back-projection example. The figure below shows how through simple back-projections of LORs, the original object can be reconstructed.

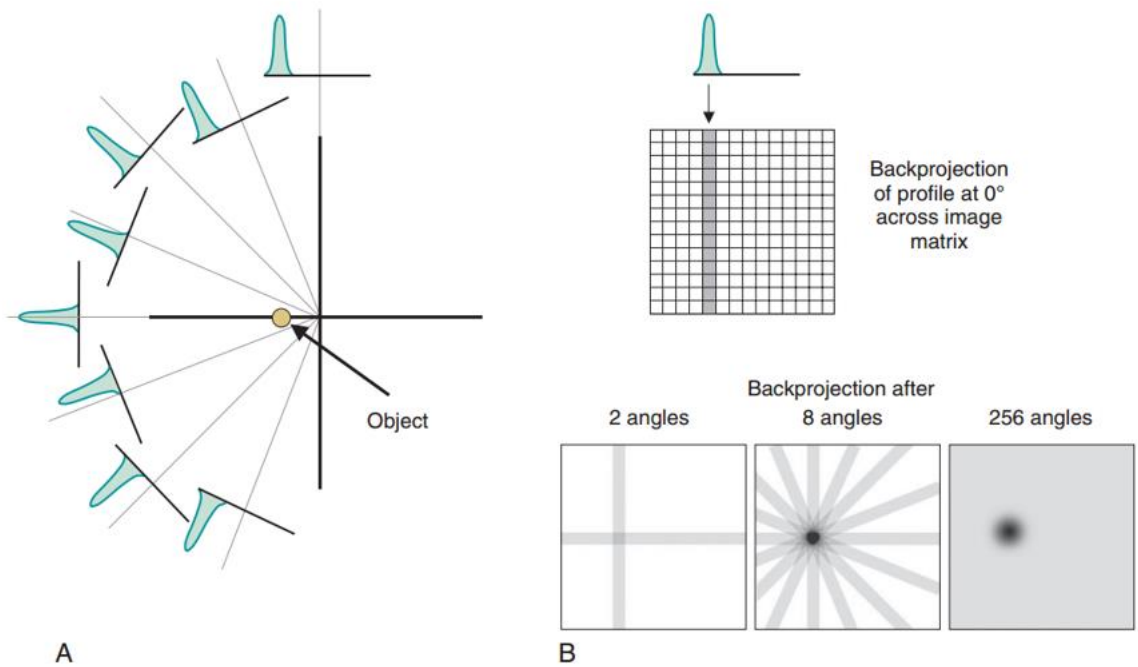

Figure 1- 7. Illustration of the steps in simple back-projection. A: Projection profiles for a point source of radioactivity for different projection angles. B: Back-projection of one intensity profile across the image at the angle corresponding to the profile. This is repeated for all projection profiles to build up the back-projected image (cited from figure 16-5[1] in Cherry SR, Sorenson JA, Phelps ME. *Physics in Nuclear Medicine*. 4th ed. Elsevier/Saunders; 2012).

Mathematically, the process can be expressed as follows.

$$f'(x,y) = \frac{1}{N}\sum_{i=1}^{N} p(xcos\phi_i + ysin\phi_i, \phi_i) \tag{1.6}$$

where ϕ_i denotes the ith projection angle and $f'(x,y)$ represents an approximation to the true radioactivity distribution, $\mathrm{f(x,y)}$.

As illustrated in Figure 1-7(b), the image built up by simple back-projection resembles the true source distribution. However, there is an obvious artifact in that counts are projected outside of the true location of the object and thus there is a blurring of its resulting image.

Certainly, the quality of image can be improved by increasing the number of projection angles and the number of samples along the profile. To be specific, this can suppress the "spoke-like" artifacts in the image, but even with an infinite number of views, the final image still is blurred. No matter how finely the data are sampled, simple back-projection always causes some apparent activity outside the true location of the source.

Mathematically, the relationship between the true image (i.e., $\mathrm{f}(x,y)$) and the image reconstructed by the simple back-projection (i.e., $f'(x,y)$) can be expressed as follows[1].

$$f'(x,y) = f(x,y) \otimes \frac{1}{r} \tag{1.7}$$

where $\otimes$ denotes the process of convolution and r represents the distance from the center of the point-source location. Because of this behavior, the effect is called as 1/r blurring.

Thankfully, the 1/r blurring effect can be completely removed using Fourier transform (FT) and applying what is typically known as the ramp filter. When considering the fact that the "convolution" operator in image-domain can be replaceable with "multiplication" in frequency-domain, and the fact that FT of 1/r is equal to $1/k_r$, where $k_r = \sqrt{{k_x}^2 + {k_y}^2}, k_x = k_r cos\phi, k_y = k_r sin\phi$, mathematically, in frequency-domain, the relationship between filtered projection profile (i.e., $P^{filtered}(k_r,\phi)$) and the measured projection profile (i.e., $\mathrm{P}(k_r,\phi)$) can be expressed as follows:

$$\begin{aligned} \mathrm{FT}\left[f(x,y)|_{\phi_i}\right] = k_r \cdot \mathrm{FT}\left[f'(x,y)|_{\phi_i}\right] &= k_r \cdot \mathrm{FT}[p(xcos\phi_i + ysin\phi_i, \phi_i)] \\ &= k_r \cdot \mathrm{P}(k_r,\phi_i) \end{aligned} \tag{1.8}$$

$$f(x,y) = \frac{1}{N}\sum_{i=1}^{N} p^{filtered}(xcos\phi_i + ysin\phi_i, \phi_i) \tag{1.9}$$

where $\mathrm{P}^{\mathrm{filtered}}(k_r, \phi) = |k_r| P(k_r, \phi)$.

In brief, by applying "ramp filter" in frequency domain to measured projection profile and sequentially doing back-projection, the 1/r blurring can be completed omitted. Because the method is using the filtered projection profile, it is called as filtered back-projection.

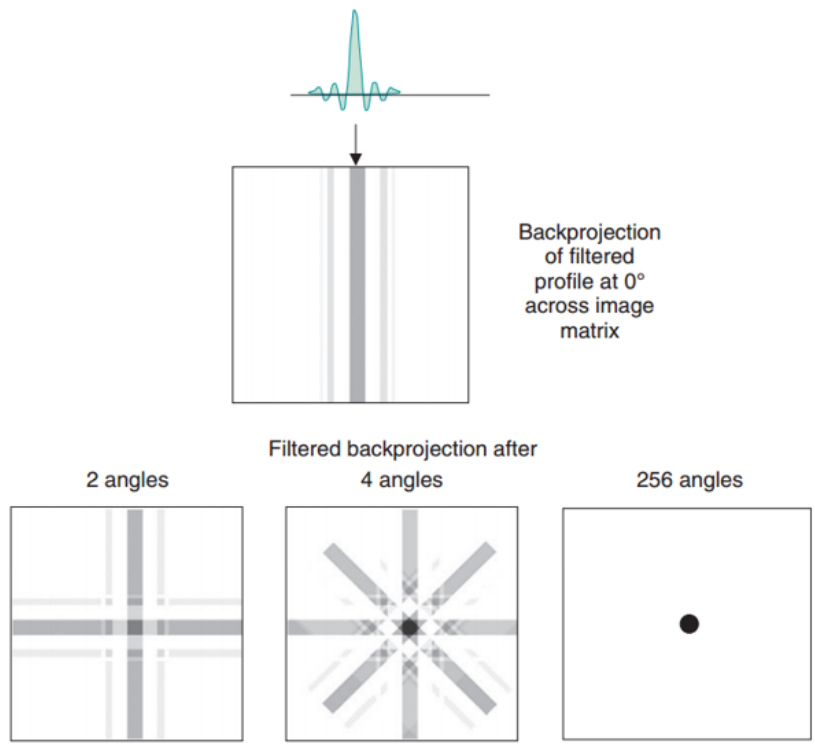

Figure 1- 8. Illustration of the steps in filtered back-projection. The one-dimensional Fourier transforms of projection profiles recorded at different projection angles are multiplied by the ramp filter. After taking the inverse Fourier transform of the filtered transforms, the filtered profiles are back-projected across the image, as in simple back-projection (cited from figure 16-9[1] in Cherry SR, Sorenson JA, Phelps ME. *Physics in Nuclear Medicine*. 4th ed. Elsevier/Saunders; 2012).

Although using the "ramp filter" can completely remove the 1/r blurring, it can also enhance the noise contribution to real image because of the fact that the noise tends to have high frequency in

frequency-domain. Thus, there are a lot of variants of the ramp filter (e.g., Shepp-Logan, Hann, et al.) to minimize the adverse effect.

The advantages of FBP includes relative ease of implementation and its high speed[1,28]. On the other hand, it has very limited ability to take into account various physical and statistical aspects of imaging system and data acquisition such as limited spatial resolution of the detector, scattered radiation, statistical nature of the coincidence events collection, positron range, and non-uniform resolution. In addition, due to the incompleteness of the projection data, it tends to produce images with high level of noise and streak artifacts[28]. Therefore, currently it is very rare to routinely use the FBP in clinic.

1.3.2. Ordered-Subset Expectation Maximization (OSEM)

The general concepts of iterative reconstruction are outlined in Figure 1-9. In essence, the algorithm approaches the true image by means of successive approximations or estimates[1–3,28].

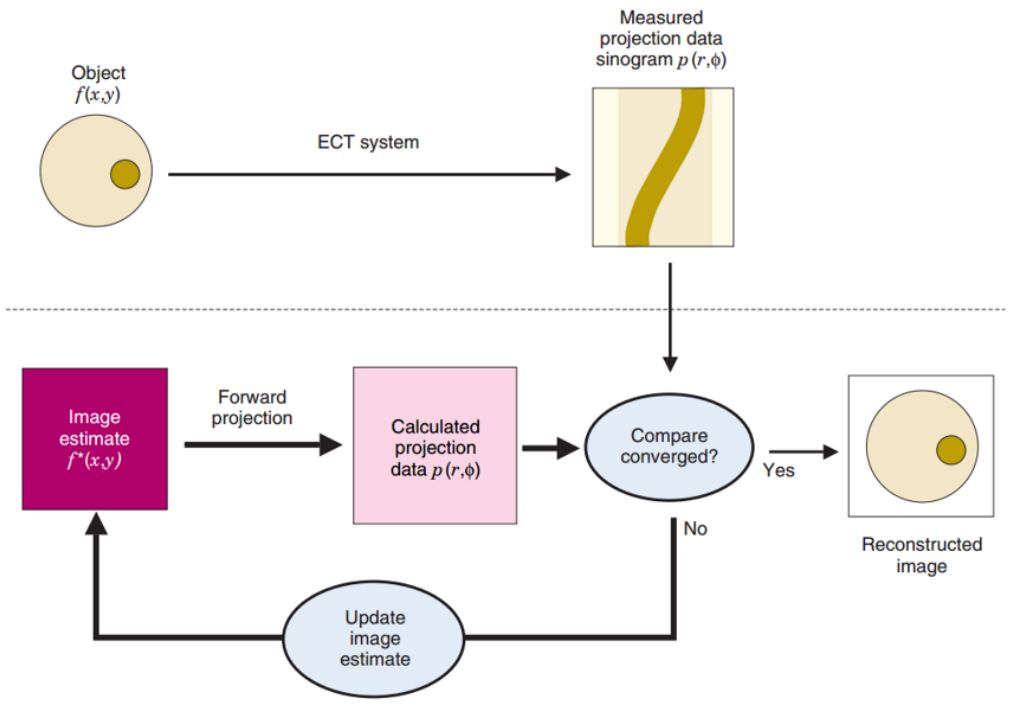

Figure 1- 9. Schematic illustration of the steps in iterative reconstruction. An initial image estimate is made and projections that would have been recorded from the initial estimate then are

calculated by forward projection. The calculated forward projection profiles for the estimated image are compared to the profiles actually recorded from the object and the difference is used to modify the estimated image to provide a closer match. The process is repeated until the difference between the calculated profiles for successively estimated images and the actually observed profiles reaches some acceptably small level (cited from figure 16-17[1] in Cherry SR, Sorenson JA, Phelps ME. *Physics in Nuclear Medicine*. 4th ed. Elsevier/Saunders; 2012)

Often the initial estimate is assumed as uniform image (i.e. all pixels have the value of one). The next step is to do forward projections to compute the projections that would have been measured for the estimated image, which is the inverse process of back-projections. It is performed by summing up the intensities along the ray paths for all projections through the estimated image. Then, the set of projections (i.e., sinogram) is compared to the measured projections. By using the difference between estimated and measured sinograms, the estimated image can be updated by back-projecting the difference. The update-and-compare process is repeated until the difference between the forward-projected profiles for the estimated image and the actually measured profiles falls below some specified level, or until the iteration numbers given by user. With proper design of the image updating procedure, the estimated image progressively converges toward the true image in terms of bias. (i.e., Figure 1-10); instead, noise level tends to increase in general due to the bias-variance tradeoff[29,30].

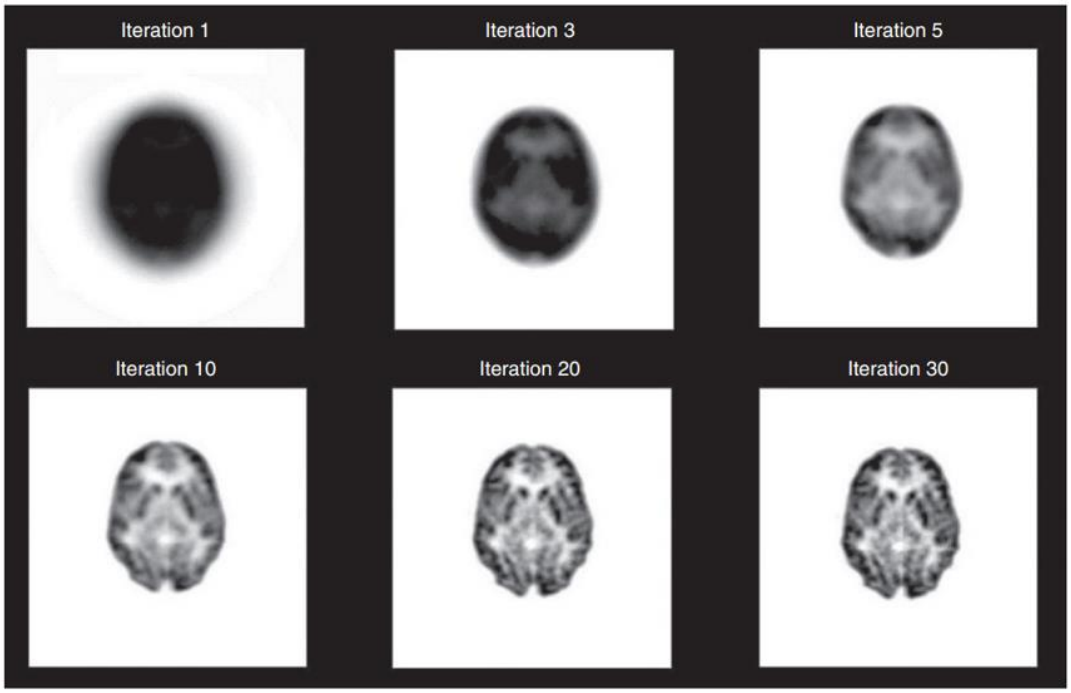

Figure 1- 10. Brain images generated for different numbers of iterations by an iterative reconstruction algorithm. Image resolution progressively improves as the number of iterations increases (cited from figure 16-18[1] in Cherry SR, Sorenson JA, Phelps ME. *Physics in Nuclear Medicine*. 4th ed. Elsevier/Saunders; 2012).

Iterative methods are the most widely used approach in PET image reconstruction and include iteratively solving the maximum Poisson likelihood or solving the maximum a posteriori (MAP) estimate. Poisson-based methods are a natural choice for PET because the measurements can be modeled as Poisson counting statistics.

The maximum likelihood expectation maximization (MLEM) algorithm[31–34] is a well-known method and is used to maximize the Poisson log-likelihood as follows.

$$\mathrm{L}(\mathbf{p}|\mathbf{f}) = \sum_{i=1}^{M} p_i \cdot ln(E[p_i]) - E[p_i] - \ln(p_i!) \tag{1.10}$$

where **f**, **p**, and M is the estimated image, the measured projections, and the number of projection elements (i.e., in 2-D reconstruction, the number of pixels for a sinogram per slice: the number of

projection angles × the number of elements in a profile per projection), and $E[p_i] = \sum_{j=1}^{N} A_{ij} f_j + r_i + \zeta_i$. N is the number of pixels in image per slice (i.e., in 2-D reconstruction), r_i is the estimated random coincidences in the ith projection element, and ζ_i is the scattered coincidences in the ith projection element. Importantly, **A** denotes system matrix of imaging system and A_{ij} represents the probability that the radiation (i.e., annihilation photon) emitted from the jth pixel will be detected in the ith projection element. Thus, technically, the system matrix **A** acts as a forward-projecting operator when applying to the matrix for a single image (i.e., matrix multiplication with the image matrix).

In MLEM, the updated image is obtained by a formula as follows.

$$f_j^{k+1} = \frac{f_j^k}{\sum_{i=1}^{M} A_{ij}} \sum_{i=1}^{M} A_{ij} \frac{p_i}{\sum_{l=1}^{N} A_{il} f_l^k + r_i + \zeta_i} \tag{1.11}$$

In matrix form, this can be expressed as follows.

$$\boldsymbol{f}^{k+1} = \frac{\boldsymbol{f}^k}{\boldsymbol{A}^T \boldsymbol{1}} \boldsymbol{A}^T \frac{\boldsymbol{p}}{\boldsymbol{A}\boldsymbol{f}^k + \boldsymbol{r} + \boldsymbol{\zeta}} \tag{1.12}$$

where $\sum_{i=1}^{M} A_{ij} = \boldsymbol{A}^T \boldsymbol{1}$ is the sensitivity image and k is the iteration number. Importantly, $\boldsymbol{A}\boldsymbol{f}^k$ corresponds to the forward-projection and $\boldsymbol{A}^T \boldsymbol{v}^k$ is the back-projection (i.e., $\boldsymbol{v}^k \equiv \frac{\boldsymbol{p}}{\boldsymbol{A}\boldsymbol{f}^k + \boldsymbol{r} + \boldsymbol{\zeta}}$). Particularly, the version with the inclusion of r and ζ is called ordinary Poisson method.

One of critical disadvantages of MLEM is its slow convergence (i.e., computational speed, compared to FBP method). As a one of variants of MLEM, the ordered-subset expectation maximization (OSEM)[35–37] is typically used to enhance a convergence speed by dividing the projection data into q subsets as follows.

$$f_j^{k+1} = \frac{f_j^k}{\sum_{i \in S_q} A_{ij}} \sum_{i \in S_q} A_{ij} \frac{p_i}{\sum_{l=1}^{N} A_{il} f_l^k + r_i + \zeta_i} \tag{1.13}$$

where S_q contains the projection data in the qth subset. Currently, OSEM is the reconstruction method of most popular usage in routine practice in clinic.

In brief, the advantages of analytic reconstruction include relative easiness of implementation and high speed. However, due to the reliance on the line-integral projection model, analytic method has a limited capability to take into account various physical and statistical effects such as the random nature of the coincidence data collection, positron range, and non-uniform resolution. Unlike analytic method, iterative method does not necessarily assume the line-integral model, and enable 1) accurate modeling of statistical noise, 2) complex detector geometries, and 3) the ability to include corrections for various degradation effects (e.g., detection of scattered events, detection of random events, positron range, photon non-collinearity, detection dead time, detector blurring, variations in detector sensitivity, patient motion, et al.) These are the main reasons why the iterative methods are generally more desirable in routine practice in clinic, compared to analytic methods. Especially, OSEM is the most popular choice in clinic because of its fast convergence speed, compared to MLEM.

In the next chapter, we briefly cover the fundamentals of kinetic modeling, from the basics (e.g., mathematical expression of kinetic models, benefits of using kinetic modeling, et al.) to the rationale of the research for this thesis (e.g., the necessity of whole-body kinetic modeling, current pitfalls and challenges, etc.).

Chapter 2. Fundamentals of Kinetic Modeling

2.1. Introduction and Rationale for Kinetic Modeling

The spatial distribution of a radiotracer in the body is time-varying and depends on a number of factors such as tracer delivery and extraction from the vasculature, binding to cell surface receptors, diffusion or transport into cells, metabolism, and wash-out effect[38–42]. Thus the analysis of temporal component often is very important in nuclear medicine studies because of its direct or indirect relationship with bio-chemical and physiological status of tissue. The mathematical models that describe the time-varying distribution of radiopharmaceuticals in the body are called as tracer kinetic models, and the analysis of the kinetics based on the models (e.g., estimation of transport rate constants) is known as kinetic modeling[1–3,38–44].

The analysis of bio-distribution and kinetics of radiopharmaceuticals through kinetic modeling can add additional benefits of using nuclear medicine images. Indeed, a number of studies have highlighted the potential effectiveness of kinetic modeling for better diagnosis and treatment response monitoring[45–49] by providing additional parameters that are closely related to the underlying biological, physiological, and pathological characteristics of tissues. In brief, there are two beneficial aspects of kinetic modeling.

The first is that the kinetic parameters can provide a new dimension for to obtain better information of the disease from PET images. For instance, for ^{18}F-FDG, the tracer remains in the blood at notable concentrations for several hours after injection. In conventional static images the standardized uptake value (SUV) reflects a mixture of un-metabolized ^{18}F-FDG exchanged with the blood and ^{18}F-FDG-6-P trapped by tumor glucose metabolism. The static image cannot distinguish between ^{18}F-FDG and ^{18}F-FDG-6-P since both have the same isotope detected by the scanner. However, kinetic modeling through dynamic scanning can distinguish the two different states (i.e., ^{18}F-FDG v.s. ^{18}F-FDG-6-P) and provide a much more specific estimate of tumor glucose metabolism[50,51].

Another aspect is that the kinetic modeling can help avoid pitfalls in interpreting standard clinical static uptake images. For instance, the persistence of ^{18}F-FDG in the blood after injection can lead to ongoing ^{18}F-FDG-6-P accumulation over time. For tumors with high glucose metabolic rates, SUV can increase over 30 % in as little as 15 min at 1 hour after injection[50]. Therefore, the variability of uptake can considerably confound the assessment of therapeutic response both in the clinic and in clinical trials[50]. The kinetic modeling enables to avoid the pitfall.

In brief, with additional use of tracer kinetic modeling, there is the potential for a substantial improvement in the kind and quality of information that can be extracted from the given PET images.

Mathematical models for kinetic modeling defines the relationship between measureable data (i.e., activity and concentration) and the bio-chemical parameters (i.e., kinetic parameters). The understanding of the mathematical models is one of critical pre-requisites to correctly exploit the benefits of kinetic modeling. Therefore, in this chapter, the basic mathematical models for kinetic modeling are briefly introduced.

2.2. Brief Review of Current Kinetic Modeling Methodologies

2.2.1. Basic Assumptions underlying the Kinetic Modeling

There are two basic assumptions for kinetic modeling:

1) Assumption #1[1,43,44,52]: a PET radiotracer is administered in such small amounts that it does not have any pharmacological effects (i.e., nonexistence of drug-effect).

2) Assumption #2[1,43,44,52]: biological functions that we are studying exist at a steady state (are not altered in the course of study).

The first assumption is known as “tracer principle” or “nonexistence of drug-effect”, which represents the nonexistent or negligible effect of a radiotracer on the bio-chemical process of interest Bio-chemical processes tend to be mainly influenced by concentration of a ligand (e.g.,

substrate) and the number of available receptors (e.g., enzyme) to the binding of interest. Thus, it is important to minimize the changes in the level of concentration of a ligand and the number of available receptors by injecting a small amount of radiotracers as much as possible. We should note that our inherent interest is the bio-chemical process before injecting the radiotracer, rather than the process changed after the injection, and that the analogue molecules (i.e., injected radiotracers) will be competing with original molecules (i.e., existent naturally) in the human or animal body in binding with the same type of receptors. Therefore, the exceptionally high sensitivity of PET scanner combined with the high specific activity of radiotracers are desirable to minimize the drug-effect by allowing for the usage of a small amount of radiotracers as much as possible.

In addition to that, it should be noted that the assumption #1 (i.e., nonexistence of drug-effect) cannot be applicable to radiopharmaceutical therapy (RPT) that typically requires much larger amount of injection per cycle[53] (e.g., 10 times larger than the activity injected for diagnosis). Hence, for the application of kinetic modeling into RPT, the established kinetic model should be modified to take the changes in concentration induced by radiopharmaceutical injected and the significantly reduced number of available receptors (i.e., the level of saturation of ligand-receptor binding) into consideration. The Delforge model[43,54–57] would be a good starting point to deal with the issue.

The second assumption is known as a “steady-state assumption”, which means that the biological process in the body will not change at least during the time of the PET scan. This is the reason why the transport rate constants between compartments can be assumed as time-invariant parameters.

However, depending on a specific application or situations deviated from the steady-state (e.g., unwanted changes in blood flow, a high amount of radiopharmaceuticals injected, et al), the research focus could be the study of transient change. For instance, there has been growing interest in detecting and quantifying transient changes in neurotransmitter concentrations that may be useful for better understanding of the etiology of neuropsychiatric diseases[58,59]. To deal with the violation from the steady-state assumption, the Delforge model[43,54–57] could be used.

In following subsections, we review a number of popular kinetic modeling techniques.

2.2.2. One-Tissue Compartment Model (1TCM)

The 1TCM (i.e., Figure 2-1) is comprised of two compartments.: 1) compartment for blood or plasma (i.e., C_p) and 2) a tissue compartment (i.e., C_R). Since there is no limitation to the definition of a compartment, basically a compartment can represent any physical or bio-chemical status of tissue. In other words, it could be any organs (e.g., blood plasma, liver, lung,etc) and any bio-chemical status (e.g., specific-binding, nonspecific-binding, etc).Depending on the radiotracer used and the bio-chemical/physiological process of interest for your research, the definitions of each compartment can be varied and should be re-defined by user.

Under the assumption that a transport rate of a radiotracer between two compartments is following the first-order kinetics (i.e., $\frac{d[A]}{dt} = \mathrm{k} \cdot [A]^1$, where [A] is the concentration of A, and k an arbitrary constant), the 1TCM can be mathematically expressed as follows[60].

$$\frac{dC_R(t)}{dt} = K_1 C_p(t) - k_2 C_R(t) \tag{2.1}$$

$$C_R = K_1 C_p(t) \otimes e^{-k_2 t} \tag{2.2}$$

K_1 and k_2 denote the influx and efflux rate constants between the blood plasma and the compartment.

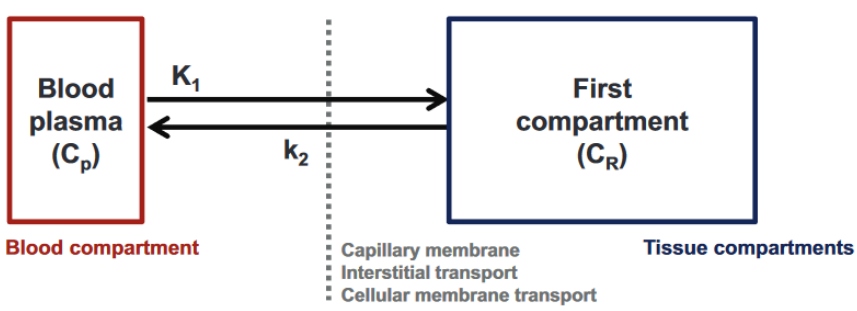

Figure 2- 1. Kinetic model for generic one-tissue compartment model (this figure was originally published in *JNM*. Pantel AR, Viswanath V, Muzi M, Doot RK, Mankoff DA. Principles of Tracer Kinetic Analysis in Oncology, Part I: Principles and Overview of Methodology. J Nucl Med. 2022; 63:342-352.).

2.2.3. Two-Tissue Compartment Model (2TCM)

The 2TCM (i.e., Figure 2-2) is comprised of three compartments.: 1) compartment for blood plasma (i.e., C_p), 2) a first compartment that can represent the interstitial space in tissue (i.e., C_R), and 3) a second compartment that can represent the tissue of interest (i.e., C_B). Based on the same assumption as in the 1TCM (i.e., first-order kinetics), the concentrations of radiotracer for each compartment can be expressed as follows[60].

$$\frac{dC_R(t)}{dt} = K_1 C_p(t) + k_4 C_B(t) - (k_2 + k_3) C_R(t) \tag{2.3}$$

$$\frac{dC_B(t)}{dt} = k_3 C_R(t) - k_4 C_B(t) \tag{2.4}$$

The Laplace transformation and the relationship shown below can be used to solve the differential equations.

$$\mathrm{L}[\mathrm{f}'(\mathrm{t})] = \mathrm{sL}[\mathrm{f}(\mathrm{t})] - \mathrm{f}(0) \tag{2.5}$$

$$\mathrm{L}[\mathrm{f}''(\mathrm{t})] = s^2\mathrm{L}[\mathrm{f}(\mathrm{t})] - \mathrm{sf}(0) - \mathrm{f}'(0) \tag{2.6}$$

where $\mathrm{L}[\mathrm{f}(\mathrm{t})]$, $\mathrm{f}'(\mathrm{t})$, $\mathrm{f}''(\mathrm{t})$, and s denote the Laplace transformation of an arbitrary function f(t), the first derivative of f(t), the second derivative of f(t), and s-variable in s-domain that is well known as a complex frequency variable with the unit of [1/sec.] if the unit of t is [sec]. All the mathematical details for the solution of the differential equations can be found in Appendix A.

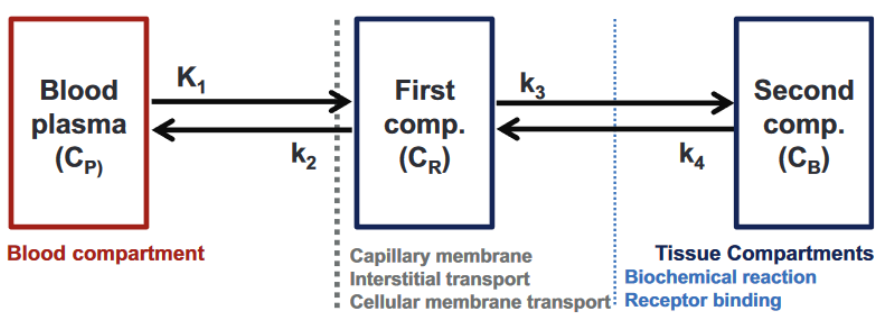

Figure 2- 2. Kinetic model for generic two-tissue compartment model (this figure was originally published in *JNM*. Pantel AR, Viswanath V, Muzi M, Doot RK, Mankoff DA. Principles of Tracer

Kinetic Analysis in Oncology, Part I: Principles and Overview of Methodology. J Nucl Med. 2022; 63:342-352.).

From the solution of the differential equations, the measured concentration from PET can be expressed as follows.

$$C_{PET}(t) = C_R + C_B = \frac{K_1}{\alpha_2 - \alpha_1}[(k_3 + k_4 - \alpha_1)e^{-\alpha_1 t} + (\alpha_2 - k_3 - k_4)e^{-\alpha_2 t}] \otimes C_p(t) \quad (2.7)$$

$$\alpha_{1,2} = \frac{k_2 + k_3 + k_4 \ \mp \ \sqrt{(k_2 + k_3 + k_4)^2 - 4k_2k_4}}{2} \quad (2.8)$$

where C_{PET} and C_p denote the measured PET concentration/activity and plasma input function, respectively, and $\otimes$ represents convolution. K_1 and k_2 are influx and efflux rate constants between plasma and the first tissue compartment, respectively, and k_3 and k_4 represent influx and efflux rate constants between the first and the second tissue compartment.

Each kinetic parameter (i.e.K_1, k_2, k_3, k_4) is called as micro-parameter..

2.2.4. Patlak Graphical Analysis (PGA): Linearized Model

The solutions of all of the systems of differential equations describing the compartments models above require nonlinear regression to estimate the individual parameters (i.e., rate constants: K_1, k_2, k_3, and k_4). Nonlinear regression is performed by an iterative method that requires considerable computational time, making it difficult to perform a voxel-wise calculation[52].

However, by a linearization of the compartment model, more rapid calculation of parameters at the voxel level can be performed. In this thesis, among the linearized models (i.e., Figure 2-3), the PGA[60,61] is presented.

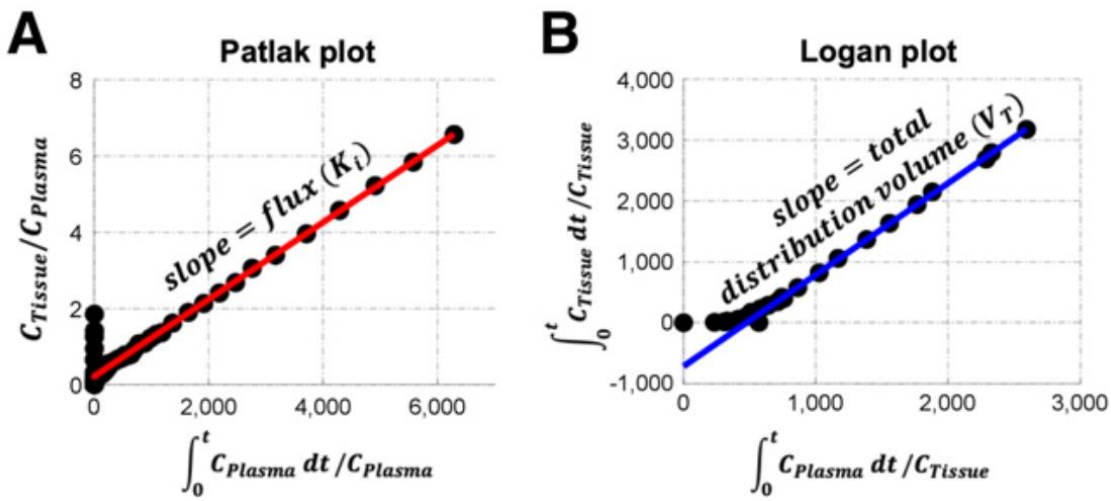

Figure 2- 3. Graphical methods of data analysis, including Patlak (A) and Logan (B) plots, where C_{Plasma} is blood time-activity curve and C_{Tissue} is tissue time-activity curve. t: time. (this figure was originally published in *JNM*. Pantel AR, Viswanath V, Muzi M, Doot RK, Mankoff DA. Principles of Tracer Kinetic Analysis in Oncology, Part I: Principles and Overview of Methodology. J Nucl Med. 2022; 63:342-352.).

Basically, the mathematical formulas for PGA can be derived from the 2TCM. If an irreversible or nearly-irreversible uptake process is assumed (i.e., $k_4 \approx 0$), the measured concentration via PET can be derived as follows from the general formulas for 2TCM.

$$C_{PET}(t)|_{k_4=0} = \frac{K_1 k_2}{k_2 + k_3} e^{-(k_2+k_3)t} \otimes C_p(t) + \frac{K_1 k_3}{k_2 + k_3} \otimes C_p(t) \tag{2.9}$$

Also, if the equilibrium between the plasma and first compartment is reached, final formulas for PGA can be derived as follows.

$$\frac{C_{PET}(t)}{C_p(t)} = K_i \cdot \frac{\int_0^t C_p(\tau)d\tau}{C_p(t)} + V_d, \qquad t > t^* \tag{2.10}$$

wheret^*denotes the time required for the equilibrium between plasma and the first compartment in 2TCM.

Further, under the assumption that blood volume fraction is negligible (i.e., $V_b \approx 0$), we can define a net influx rate constant K_i and a volume of distribution V_d as follows.

$$K_i = \frac{K_1 k_3}{k_2 + k_3} \tag{2.11}$$

$$V_d = \frac{K_1 k_2}{(k_2 + k_3)^2} \tag{2.12}$$

The K_i and V_d are called a PGA parameter and categorized as macro-parameter because of the fact that it is comprised of several micro-parameters. The derivation of the PGA formulas from the 2TCM (i.e., line-by-line derivations) and conceptual meaning of PGA parameters are shown in Appendix A and B .

2.3. The Necessity for Whole-Body Kinetic Modeling

Clinical diagnosis and treatment response monitoring of localized and metastatic cancers have benefited remarkably from the advent of whole-body (WB) positron emission tomography (PET) integrated with computed tomography (PET/CT) imaging[16,62–67]. Currently, the standardized uptake value (SUV) is widely employed as a surrogate for metabolic activity. The SUV is defined as follows.

$$\mathrm{SUV(t)} = \frac{A(t)}{D \cdot 2^{\frac{-\Delta t}{T_{\frac{1}{2}}}}} \cdot BW \tag{2.13}$$

where A(t), D, and BW denote activity [Bq/ml] at time t, injected dose [Bq], and body weight (g), respectively. Δt and $T_{\frac{1}{2}}$ represent time delay between the injection time and the scan time [sec.] and the half-life of radiotracers [sec.], respectively.

However, the PET tracer distribution is a dynamic process altered by several factors that vary considerably depending on the organ, region of interest (ROI), patient, and time of scan[62,68]. Hence, static SUV images are time-dependent, which is a huge limitation and undesirable for use in

quantitative studies. As an example, to make PET images comparable between patients and for the same patient scanned at different times, they are usually collected at 60 minutes after the administration of ^{18}F-FDG. Comparing images acquired at different times post-injection would not result in a fair comparison.

However, compared to the static image (i.e., SUV), parametric images via kinetic modeling are not time-dependent and can provide a variety of types and qualities of information of the bio-chemical and physiological status of tissues and/or ROIs in whole-body[62,63]; definitely allowing further clinical benefits from PET images through quantitative analysis. A huge number of studies have shown that kinetic compartment modeling can improve both tumor characterization and treatment response monitoring[45–49,63].

2.4. Current Pitfalls and Challenges

With a typical PET scanner, dynamic PET protocols have been confined to a single-bed position, limiting the axial field-of-view of parametric images to ~15-25 cm. However, protocols that perform fast multi-pass multi-bed acquisitions have been increasing attention[16,64–67].

To achieve four-dimensional (4D) PET acquisition for WB kinetic modeling, the following three challenges must be addressed: (1) long acquisition time, (2) few dynamic frames at each bed (i.e., sparsity of data), and (3) noninvasive quantification of rapid early kinetics in the plasma.

Karakatsanis et al. optimized the scanning protocol through extensive Monte Carlo simulation studies and proposed a method for input function estimation and dynamic WB dataset generation[68,69]. It comprises two sequential scanning steps: (1) an initial 6 min single-bed dynamic scan over the cardiac region to generate an image-derived input function and (2) a sequence of six multi-pass WB scans to capture the late dynamics of the tracer in the blood plasma and WB tissues. This is the same protocol that we have implemented in this thesis for patient data acquisition (i.e., chap. 3 and 4).

Although the optimal protocol allows for WB kinetic modeling, we should note the fact that it was optimized based on a macro-parameter, specifically the net influx rate from the plasma into the second compartment in the two-tissue compartment model (i.e., K_i); thus, it might not be an appropriate protocol for micro-parameter estimation if least squares estimation (LSE) is exploited, which is the current common standard of parameter estimation for kinetic modeling.

Unlike macro-parameter estimation, there are two factors that can contribute to uncertainty in micro-parameter estimation: (1) the loss of early dynamics of time activity (i.e., the loss of near-peak data), and (2) sparsity of measured data (i.e., 5-6 min of time interval of measurement). Due to these factors, the estimation of micro-parameter for whole-body kinetic modeling has not been attempted in cases where a typical PET scanner is the only available option for dynamic scans.

Given that the detailed explanatory power of micro-parameter in assessing the bio-chemical and physiological status of tissues can significantly enhance effectiveness and flexibility in clinical applications, surpassing the capabilities of macro-parameters, there is a need to develop a novel method that can open the door to a typical PET-based WB kinetic modeling for micro-kinetic parameters.

In the next chapter, we will present a novel parameter estimation method that enables typical PET-based WB kinetic modeling for micro-kinetic parameters by addressing the issues above. Further, we will show the improved performance in image quality, visibility, and tumor detectability, compared to the current common standard (i.e., LSE).

Chapter 3. Development and Validation of the PCDE method

3.1. Introduction

Clinical diagnosis and treatment response monitoring of localized and metastatic cancers have benefited remarkably from the advent of whole-body (WB) positron emission tomography (PET) integrated with computed tomography (PET/CT) imaging.[16,62–67] Currently, the standardized uptake value (SUV) is the metric used to measure metabolic activity from quantitative images. PET tracer distribution is a dynamic process altered by several factors that vary considerably depending on the organ, region of interest (ROI), patient, and time of scan[62,68]. Hence, static SUV images are time-dependent, which is undesirable for use in quantitative studies. With the additional use of tracer kinetic modeling techniques that require dynamic PET scanning, there is the potential for substantially improving the type and quality of information of the biological and physiological processes in tissue [62,63] that is not time-dependent. This can enable further clinical benefits from PET images through quantitative analysis. Many studies have shown that kinetic compartment modeling can improve both tumor characterization and treatment response monitoring[45–49,63].

Nonetheless, dynamic PET protocols have been confined to a single-bed position, limiting the axial field-of-view of parametric images to ~15-25 [cm], and have not been translated to multi-bed positions (i.e., WB). However, it is more desirable to inspect disseminated diseases and this has been gaining increasing attention[16,64–67].

To achieve four-dimensional (4D) WB PET acquisition, the following three challenges present themselves: (1) long acquisition times, (2) few dynamic frames at each bed (i.e., sparsity of data), and (3) noninvasive quantification of rapid early kinetics in the plasma. Karakatsanis et al. optimized the scanning protocol through extensive Monte Carlo simulation studies. [68,69] They proposed an optimal protocol for input function estimation and dynamic WB dataset generation, which comprises two sequential scanning steps: (1) an initial 6 min single-bed dynamic scan over

the cardiac region to generate an image-derived input function (addressing challenge number 3) and (2) a sequence of six multi-bed multi-pass WB scans to capture the late dynamics of the tracer in the blood plasma and tissue.

Although the optimal protocol allows for WB kinetic modeling, it was optimized for the measurement of macro-parameters, specifically the net influx rate from the plasma into the 2nd compartment in the two-tissue compartment model (i.e., K_i).; macro-parameters are lumped constants comprised of several micro-parameters. Hence, this method is not the most appropriate protocol for micro-parameter estimation if least squares estimation (LSE) is exploited.

Two factors can contribute to uncertainty in micro-parameter estimation: (1) the loss of early dynamics of time activity (i.e., the loss of near-peak data), except for the chest region in the FOV of the first 6 minutes of the acquisition, and (2) sparsity of measured data (i.e., 5-6 min between scans of the same anatomical region). Due to these factors, the estimation of micro-parameters for whole-body kinetic modeling has not been fully implemented in cases where a typical PET scanner (i.e. axial FOV between 15-25 cm) is the only available option for dynamic scans. However, the detailed explanatory power of micro-parameter estimation in assessing the biochemical status of tissues can significantly enhance effectiveness and flexibility in clinical applications, surpassing the capabilities of macro-parameters.

We aimed to develop a novel method to enable accurate kinetic modeling including estimation of micro-parameters using multi-pass protocols in typical PET scanner-based WB imaging. We refer to this new method as parameter combination-driven estimation (PCDE). We evaluated the method in terms of image quality, overall visibility, and tumor detectability compared to LSE (i.e., common standard).

3.2. Methods

3.2.1. Generating Simulated Data

3.2.1.1. Noise-free Images

To generate ground-truth PET images, we employed the 4D extended cardiac-torso (XCAT) phantom[70], which is well-validated and widely used for performance testing of new algorithms or approaches in numerous areas of medical imaging. The dynamics of the activity distribution assigned to each ROI in the XCAT phantom were based on actual fluorodeoxyglucose (FDG) kinetic micro-parameters, as reported in the literature[68,71] and are presented in Tables 3-1 and 2. In this study, the irreversible uptake process so k_4 is assumed to be zero.

Table 3- 1. Ground truths of kinetic micro-parameters for normal whole-body organs.

	K_1	k_2	k_3
Brain	0.13	0.63	0.19
Thyroid	0.97	1.00	0.07
Myocardium	0.82	1.00	0.19
Spleen	0.88	1.00	0.04
Pancreas	0.36	1.00	0.08
Kidney	0.70	1.00	0.18
Liver	0.86	0.98	0.01
Lung	0.11	0.74	0.02

Table 3- 2. Ground truths of kinetic macro-parameters for tumors.

	K_1	k_2	k_3
Lung	0.3	0.86	0.05
Liver	0.24	0.78	0.1

*Tumor shape and size: sphere with 1.5 cm diameter.

A plasma input function was created based on Feng's model[72], and the basic formula of the two-tissue compartment model (2TCM) was used to calculate true activities over time as follows:

$$C_{PET}(t) = \frac{K_1}{\alpha_2 - \alpha_1}[(k_3 + k_4 - \alpha_1)e^{-\alpha_1 t} + (\alpha_2 - k_3 - k_4)e^{-\alpha_2 t}] \otimes C_p(t) \qquad (3.1)$$

$$\alpha_{1,2} = \frac{k_2 + k_3 + k_4 \mp \sqrt{(k_2 + k_3 + k_4)^2 - 4k_2k_4}}{2} \tag{3.2}$$

where C_{PET} and C_p denote the measured PET concentration and plasma concentration input function, respectively, and $\otimes$ is the convolution operator. K_1 and k_2 are the influx and efflux rate constants between the plasma and first tissue compartments, and k_3 and k_4 represent the influx and efflux rate constants between the first and second tissue compartments, respectively.

To alleviate the long scan time (i.e., one of the disadvantages of dynamic acquisition), we limited the total acquisition duration to 40 min after injection. We also only used the data between 10-40 min post-injection (PI) to simulate the loss of early dynamics due to first-phase scanning of the cardiac region. Based on true kinetic parameters (i.e., Tables 3-1 and 2) and the predefined scanning protocol for virtual dynamic set (i.e., Table 3-3), the calculated concentrations with time were assigned for each ROI in the XCAT input files to generate noise-free XCAT phantom images.

Table 3- 3. Scanning protocol for virtual dynamic dataset.

Item	Value
Total acquisition time (cardiac + whole-body)	40 min
Image acquisition for whole-body	*10-40 min
Time interval	5 min
# of passes	7
# of beds	5

*10 min was assumed to simulate a scenario worse than that of the protocol proposed by Karakatsanis. Time: Post-injection time.

3.2.1.2. Noise Realizations

To add realistic noise, we employed a Dynamic PET Simulator of Tracers via Emission Projection[73,74] ($d_{PETSTEP}$), which is a fast and simple tool to simulate dynamic PET as an alternative to Monte Carlo simulation. Noise-free XCAT phantom images and attenuation maps were used as

input data to generate a realistic (i.e., noisy) dynamic PET dataset. The validated settings for the GE Discovery LS scanner[73] were used with the ordered subset expectation maximization (OSEM) algorithm. Table 3-4 summarizes the reconstruction settings for $d_{PETSTEP}$.

Table 3- 4. Summary of reconstruction settings.

Item	Value
Sensitivity	$5.27\ \text{cps} \cdot kBq^{-1} \cdot ml$
Radial bins	283
Projection angles	336
OSEM iterations	1-5
OSEM subsets	24
PSF	5.1 mm
Post-filter XY	6 mm Gaussian
Post-filter Z	[1 2 1]/4
*Reconstructed matrix per bed	165 x 165 x 35
Reconstructed voxel size	2 x 2 x 4.25 mm
Noise realizations	10

*Reconstructed matrix for the entire body: 165 × 165 × 175.

3.2.2. Proposed Parameter Combination-Driven Estimation Method

3.2.2.1. Basic Concepts and Assumptions

PCDE is a novel method for micro-parameter estimation. This method has two distinctive characteristics compared to LSE: 1) the allowance of an one-on-one correlation between early (e.g., ≤ 10 min PI) and late (e.g., > 10 min PI) dynamics of TACs by limiting the resolution of the estimated kinetic parameter (e.g., up to 2nd decimal place), and 2) employment of multi-aspect time-activity curve (TAC) in selection of best fits.

The first characteristic is based on two assumptions: 1) each micro-parameter has a finite range[68,71], and 2) the imaging system has a finite level of precision in the determination of a micro-parameter (i.e., step size of a micro-parameter). Under these assumptions, only a finite number of TACs are available for a given range and precision, which enables to improve the probability of having a

one-on-one relationship between early and late dynamics by filtering out similar TACs. Indeed, with the parameter resolution of 2nd decimal place (i.e., step size: 0.01), almost all TACs from 2TCM are most likely to be unique with the unit of [kBq/ml] and thus have a higher probability of having a one-to-one correlation between early and late dynamics for each TAC. Importantly, this improved uniqueness enables to predict a full TAC (i.e., early + late) even in the situation where the early dynamics is missing.

The second characteristic is a finer and more consistent comparison between the measured and true TACs, compared to LSE. Inherently, the sum of squared error (SSE) cannot account for positive and negative errors differently[75–79]. Therefore, minimizing the SSE of concentration/activity (i.e., LSE) might not capture very small TAC trends well; something critical for micro-parameter estimation. Instead, other aspects of TAC (e.g., its 1st and 2nd derivatives) can be effective criteria for further finely assessing curve trends. Additionally, a comprehensive comparison of various aspects of TACs would yield more stable and balanced results. Relying solely on a single aspect for comparison could lead to significantly varied and unstable outcomes, influenced by factors such as noise level, type, number of passes in whole-body scans, measurement time intervals, and voxel positions within the body[80–82]. Thus, a comprehensive consideration of the multiple aspects of TAC would allow for a more consistent comparison. The details are presented in the next section.

3.2.2.2. Workflow and Similarity Measure

The workflow of the proposed method comprises three steps:1) building a true TAC database by setting each micro-parameter range and a resolution of estimated parameters, 2) selecting the top-300 optimal parameter combinations with respect to SSE in ascending order and sequentially, selecting the top-10 using the absolute difference of area under the curve (AUC) between the measured and ground truths in ascending order, and 3) selecting the best parameter combination using a comprehensive comparison based on multiple TAC aspects. Figure 3-1 shows the workflow of the proposed method.

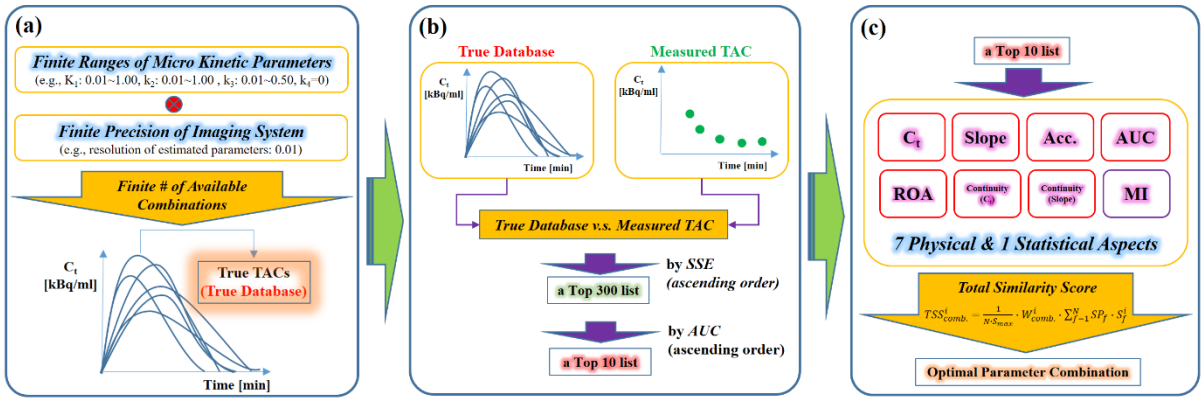

Figure 3- 1. PCDE workflow. (a): Building a true TAC database. (b): Selecting the top 300 combinations followed by top 10 by comparing measured and true TAC databases. (c): Selecting the optimal combination using comprehensive comparison based on multi-aspect of TAC.

For the comprehensive comparison, a total similarity score (TSS) is defined as follows.

$$TSS^{i}_{comb.} = \frac{1}{N \cdot S_{max}} \cdot W^{i}_{comb.} \cdot \sum_{f=1}^{N} SP_f \cdot S^{i}_{f} \tag{3.3}$$

where i, f, and N denote an index for a parameter combination in the top-10 list, an index for an aspect of TAC, and the total number of aspects considered, respectively. $W^{i}_{comb.}$, SP_f, S^{i}_{f}, and S_{max} represent the relative weight of the ith combination, selection power for aspect f, a scaled score of the ith combination for aspect f, and the maximum scaled score, respectively. Table 3-5 shows the similarity metric and the order for assigning the scaled scores to each parameter combination set. Depending on the raw score ranking in the top-10 list, scaled scores for each combination were assigned from 10 to 1 in descending order (i.e., maximum score: 10, step size: 1).

Table 3- 5. Similarity measure and order to assign scaled scores to each combination.

Aspect	Similarity Metric	Order
C_t	SSE	Ascending
Slope	SSE	Ascending
Acc.	SSE	Ascending
AUC	AD	Ascending
ROA	Itself	Descending
Continuity (C_t)	SE	Ascending
Continuity (slope)	SE	Ascending
MI	Itself	Descending

C_t, concentration; Acc., acceleration; ROA, ratio of overlapped area; MI, mutual information; SSE, sum of squared error; SE, squared error; AD, absolute difference; Scaled score: 10 to 1 depending on the ranking among the top-10 lists (step size: 1).

In the current version, we consider eight physical and statistical aspects of TAC: 1) concentration/activity, 2) slope and 3) acceleration of TAC to consider a fine TAC trend, 4) AUC, 5) ratio of overlapped area (ROA) to compensate for a limitation of simple AUC comparison, continuities of 6) concentration and 7) slope at the earliest measurement time between true and measured quantities for each to account for the relatively higher importance of data at an early time after injection, and 8) mutual information as a statistical similarity measure[83,84].

In addition, to quantitatively account for the different capabilities of each TAC aspect in how well an aspect can distinguish parameter combinations in the top-10 list separately, we defined the relative selection power (SP_f) as follows:

$$SP_f \equiv \frac{CV_f}{\sum_{f=1}^{N} CV_f} \tag{3.4}$$

where f and N denote the index for an aspect of the TAC and total number of aspects considered, respectively, and CV_f represents the coefficient of variation for aspect f. Figure 3-2 shows the calculation process for the relative selection powers.

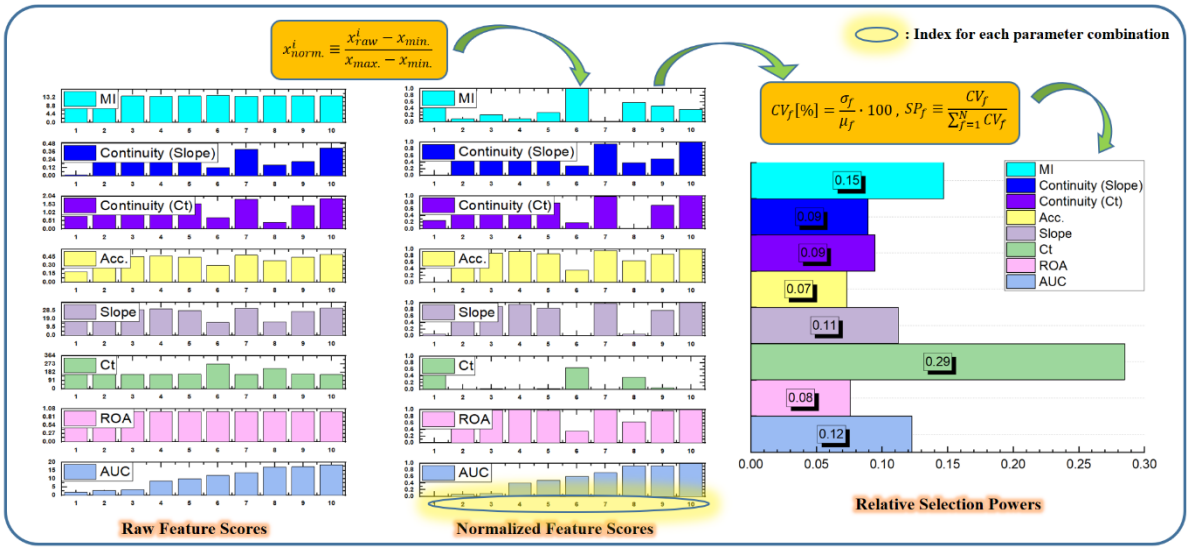

Figure 3- 2. Calculation of relative selection powers for each aspect of TAC. (1) Calculate normalized scores for each aspect by min-max normalization. (2) Calculate coefficients of variation for each aspect and the relative values that represent selection powers for each aspect.

Furthermore, we defined a parameter combination weight (i.e., $W^{i}_{comb.}$) to account for the relative occurrence probability of a parameter combination in the top-10 list so that the more probable combination can contribute more to the TSS, assuming that each micro-parameter is independent of the others. The formulas are as follows:

$$W^{i}_{comb.} \equiv \frac{P^{i}_{comb.}}{\sum_{i=1}^{10} P^{i.}_{comb.}} \tag{3.5}$$

$$P^{i}_{comb.} \equiv P_{K1}^{K1\ of\ ith\ comb.} \cdot P_{k2}^{k_2\ of\ ith\ comb.} \cdot P_{k3}^{k_3\ of\ ith\ comb.} \tag{3.6}$$

where i denotes an index for a parameter combination, and $P_{K1}^{K1\ of\ ith\ comb.}$, $P_{k2}^{k_2\ of\ ith\ comb.}$, and $P_{k3}^{k_3\ of\ ith\ comb.}$ represent the probabilities of having K_1, k_2, k_3 for the ith combination, respectively. $P^{i}_{comb.}$ is the probability of occurrence of the ith combination. Figure 3-3 shows the calculation process for the parameter combination weights.

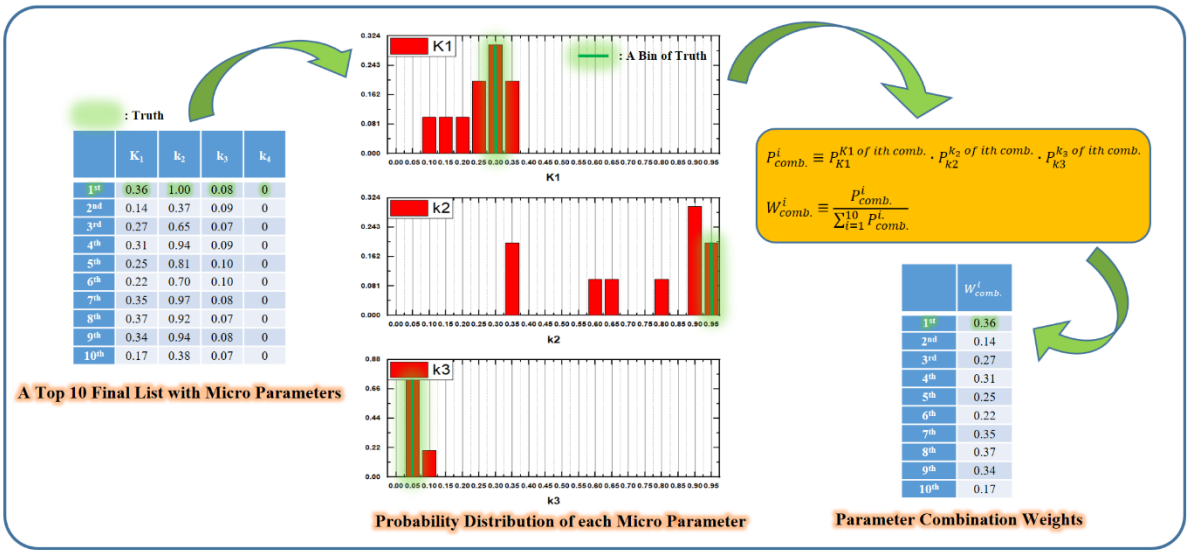

Figure 3- 3. Calculation of parameter combination weights for each combination in the top-10 list. (1) Acquire probability distributions of micro-parameters from the top 10 list. (2) Calculate occurrence probabilities for each combination in the top-10 list and relative values that represent the weights for each parameter combination.

3.2.3. Kinetic Parameters of Interest for Comparison Study

On the noisy virtual dynamic dataset, kinetic modeling was performed through each method (i.e., LSE and PCDE) and the kinetic parameters of interest for comparison are defined as follows.

3.2.3.1. Kinetic Micro-parameters.

For the micro-parameters, we compared the LSE-based 2TCM[60] with the proposed PCDE method. Because we focused on the irreversible uptake process, only the parametric K_1, k_2, and k_3 images were compared.

3.2.3.2. Kinetic Macro-parameters

For the macro-parameters, we compared the parametric images of the LSE-based Patlak graphical analysis (PGA)[60,61] with those of PCDE. Assuming an irreversible or nearly irreversible uptake process in 2TCM (i.e., $k_4 \approx 0$), the PGA formula can be derived as follows:

$$\frac{C_{PET}(t)}{C_p(t)} = K_i \cdot \frac{\int_0^t C_p(\tau)d\tau}{C_p(t)} + V_d, \qquad t > t^* \tag{3.7}$$

where t^* denotes the time required to reach equilibrium between the plasma and the first compartment in the 2TCM.

Furthermore, assuming that the blood volume fraction was negligible (i.e., $V_b \approx 0$), we defined the net influx rate constant K_i and volume of distribution V_d as follows:

$$K_i = \frac{K_1 k_3}{k_2 + k_3} \tag{3.8}$$

$$V_d = \frac{K_1 k_2}{(k_2 + k_3)^2} \tag{3.9}$$

3.2.4. Quantitative Evaluation Criteria

3.2.4.1. General Image Quality

Normalized Bias (NBias). As a measure of accuracy, NBias is determined by first calculating NBias_i for the ith voxel of an ROI over all R noise realizations and subsequently averaging over all voxels of that ROI as follows:

$$\text{NBias} = \frac{1}{n}\sum_{i=1}^{n}\left(\frac{\left|\overline{f_i} - \mu_i\right|}{\mu_i}\right) = \frac{1}{n}\sum_{i=1}^{n} NBias_i \tag{3.10}$$

where $\overline{f_i} = \left({}^{1}/_{R}\right)\sum_{r=1}^{R} f_i^r$; f_i^r denotes the ith voxel value from the rth noise realization, and μ_i, n, and R represent the truth of the ith voxel, the number of voxels in an ROI, and the number of noise realizations, respectively.

Normalized Standard Deviation (NSD). As a precision measure, the NSD_i of the ith voxel was first calculated over all R realizations, followed by averaging over all n voxels of an ROI to calculate the NSD of the ROI as follows:

$$\mathrm{NSD} = \frac{1}{n}\sum_{i=1}^{n}\frac{\sqrt{\frac{1}{R-1}\sum_{r=1}^{R}\left(f_i^r - \overline{f_i}\right)^2}}{\overline{f_i}} = \frac{1}{n}\sum_{i=1}^{n} NSD_i \tag{3.11}$$

Normalized Root Mean Squared Error (NRMSE). As a measure of comprehensive performance (i.e., combined measure of accuracy and precision), $NRMSE_i$ was first calculated for each ith voxel over all realizations, followed by spatial averaging over all voxels of an ROI to calculate the NMSE for an ROI as follows:

$$\mathrm{NRMSE} = \frac{1}{n}\sum_{i=1}^{n}\frac{\sqrt{\frac{1}{R}\sum_{r=1}^{R}(f_i^r - \mu_i)^2}}{\mu_i} = \frac{1}{n}\sum_{i=1}^{n} NRMSE_i \tag{3.12}$$

For each ROI of interest (Table 3-1), the calculations of all three quantities were repeated by changing the number of OSEM iterations, as listed in Table 3-4. To compare the general image quality between each estimation method (i.e., LSE vs. PCDE), we plotted the NBias-NSD tradeoff curves. In addition, NRMSEs were plotted against the number of iterations.

3.2.4.2. Overall Visibility and Tumor Detectability

Signal to Noise Ratio (SNR). As a measure of the overall visibility relevant to the identification of suspicious lesions in WB (i.e., global inspection), the SNR of an ROI was determined by averaging the SNRs over all noise realizations as follows:

$$\mathrm{SNR} = \frac{1}{R}\sum_{r=1}^{R}\frac{\overline{f_r}}{\sqrt{\frac{1}{n-1}\sum_{i=1}^{n}\left(f_i^r - \overline{f_r}\right)^2}} = \frac{1}{R}\sum_{r=1}^{R} SNR_r \tag{3.13}$$

where $\overline{f_r} = \left({}^{1}/_{n}\right) \sum_{i=1}^{n} f_i^r$.

A Spatial Noise ($NSD_{spatial}$). As another measure of overall visibility, the $NSD_{spatial}$ of an ROI was calculated by averaging the NSDs over all realizations as follows:

$$NSD_{spatial} = \frac{1}{R}\sum_{r=1}^{R} \frac{\sqrt{\frac{1}{n-1}\sum_{i=1}^{n}\left(f_i^r - \overline{f_r}\right)^2}}{\overline{f_r}} = \frac{1}{R}\sum_{r=1}^{R} NSD_{spatial}^{r} \tag{3.14}$$

By comparing Equations (11) and (14), it should be noted that NSD quantifies the average level of noise across multiple realizations at each voxel for an ROI, whereas $NSD_{spatial}$ known as ROI roughness, measures the average of the spatial noise across multiple realizations for an ROI[68].

Tumor to Background Ratio (TBR). As a measure of tumor detectability within a particular organ (i.e., local inspection), TBR was determined as follows:

$$\text{TBR} = \frac{1}{R}\sum_{r=1}^{R} \frac{\overline{f_r^{Tumor}}}{\overline{f_r^{BKG.}}} = \frac{1}{R}\sum_{r=1}^{R} TBR_r \tag{3.15}$$

where $\overline{f_r^{Tumor}}$ and $\overline{f_r^{BKG.}}$ denote $\overline{f_r}$ of tumor and background ROI, respectively.

Contrast to Noise Ratio (CNR). As a measure of tumor detectability within a specific organ (i.e., local inspection), the CNR was calculated as follows:

$$\text{CNR} = \frac{1}{R}\sum_{r=1}^{R} \frac{\left|\overline{f_r^{Tumor}} - \overline{f_r^{BKG.}}\right|}{\sigma_r^{BKG.}} = \frac{1}{R}\sum_{r=1}^{R} CNR_r \tag{3.16}$$

where $\sigma_r^{BKG.} = \sqrt{\frac{1}{n-1}\sum_{i=1}^{n}\left(f_i^r - \overline{f_r^{BKG.}}\right)^2}$.

Relative Error of TBR (RE_{TBR}*)*. It is possible to have a misleading (i.e., erroneously higher) TBR and/or CNR originating from a high bias (i.e., the wrongly increased/decreased mean ROI) and/or zero-like noise (i.e., the noise is approximately zero) owing to the local minimum issue of the LSE. Hence, the RE_{TBR} was also calculated as an auxiliary measure.

$$RE_{TBR} = \frac{|TBR_{Measured} - TBR_{Truth}|}{TBR_{Truth}} \tag{3.17}$$

where $TBR_{Measured}$ and TBR_{Truth} denote a measured and true TBR, respectively.

3.2.4.3. Overall Performance Metrics

To verify the overall performance of each parametric image, the overall NBias, NSD, NRMSE, SNR, and $NSD_{spatial}$ metrics were defined as the volume-weighted averages of the individual ROIs metrics[68].

3.3. Results

3.3.1. NBias-NSD Tradeoff and NRMSE

3.3.1.1. Kinetic Micro-parameters

Figures 3-4, 5, and 6 show the ROI-based NBias-NSD tradeoff and NRMSE results for the parametric K_1, k_2, and k_3 images, respectively. Overall the proposed PCDE method showed lower NBias and NSD compared to the LSE-based 2TCM, which allows much lower NRMSEs for all normal WB organs of interest; the common standard shows smaller NSDs in K_1 images. However, significantly high levels of NBias result in larger NRMSEs for all ROIs.

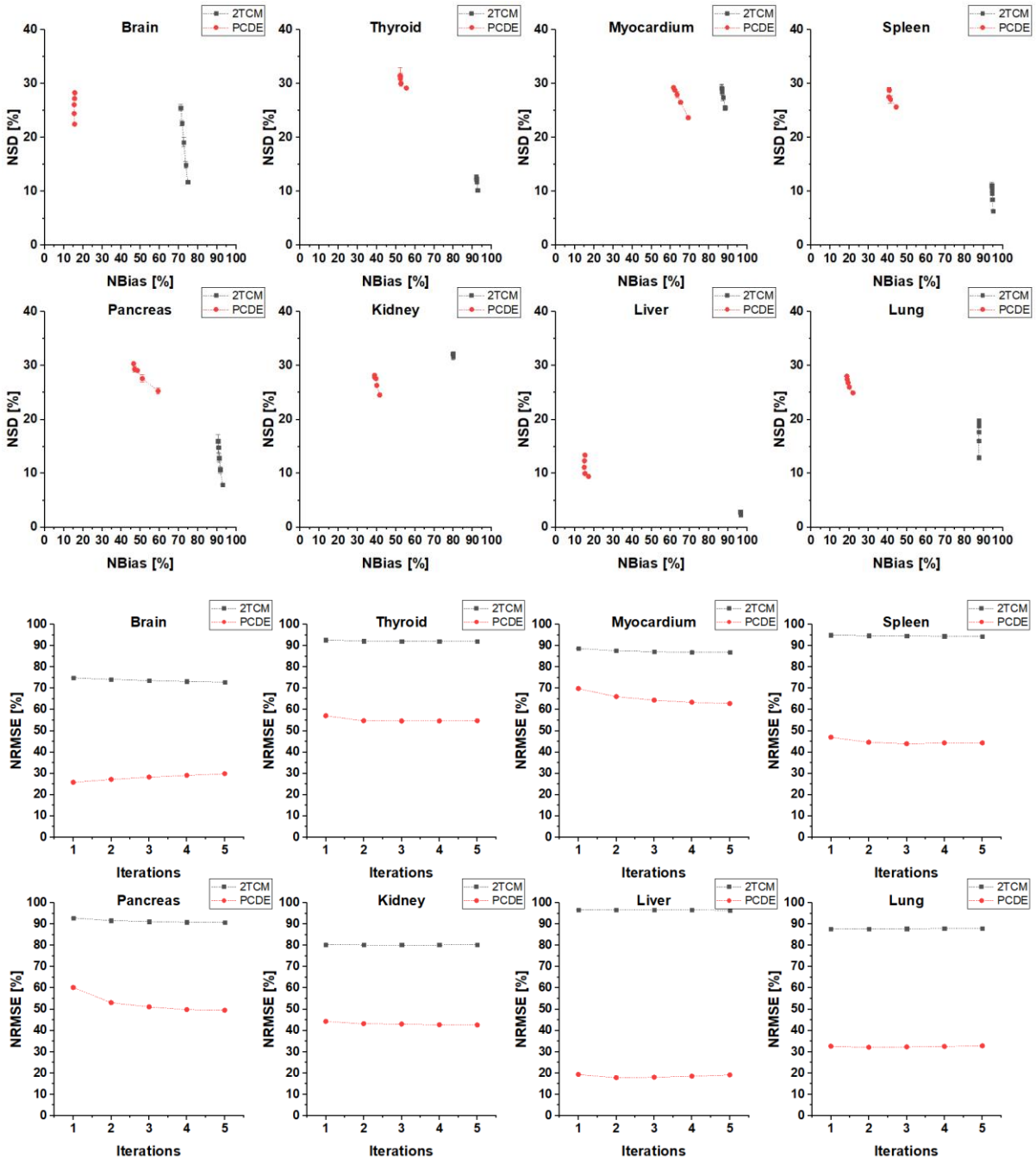

Figure 3- 4. ROI-based NBias-NSD tradeoff (i.e., upper two rows) and NRMSE with OSEM iterations (i.e., lower two rows) for parametric K_1 images.

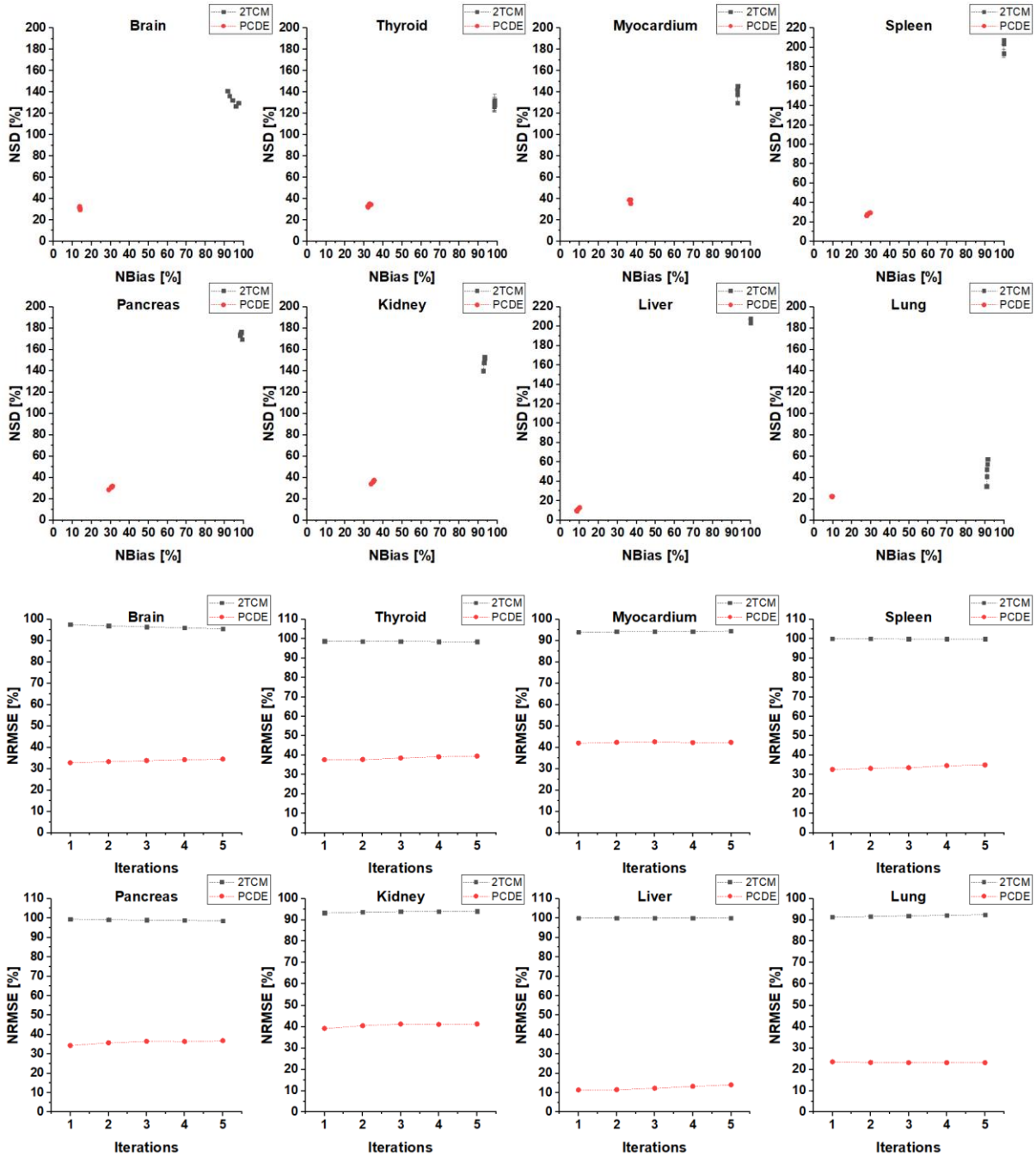

Figure 3- 5. ROI-based NBias-NSD tradeoff (i.e., upper two rows) and NRMSE with OSEM iterations (i.e., lower two rows) for parametric k_2 images.

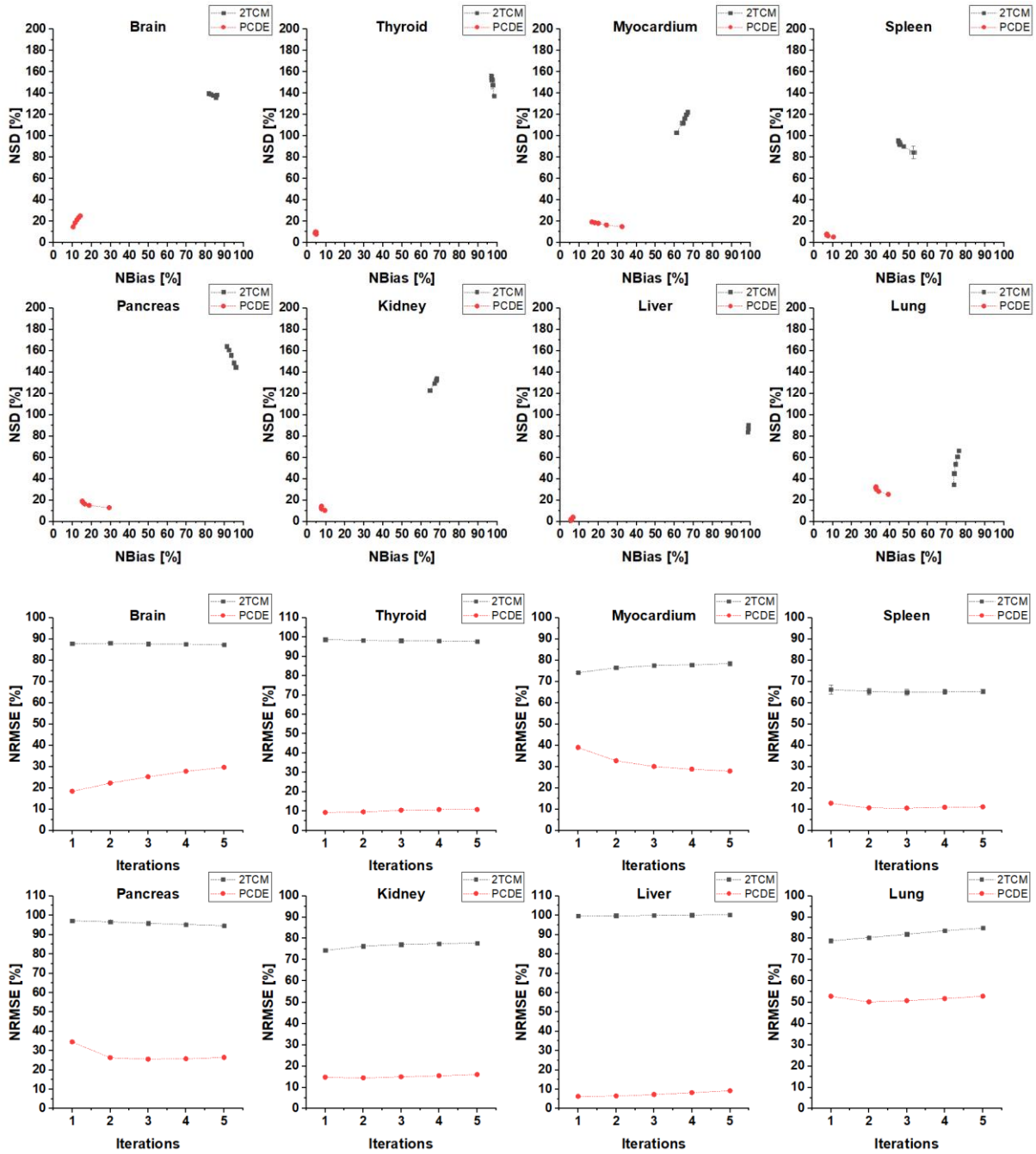

Figure 3- 6. ROI-based NBias-NSD tradeoff (i.e., upper two rows) and NRMSE with OSEM iterations (i.e., lower two rows) for parametric k_3 images.

Figure 3-7 shows the overall NBias-NSD tradeoff and NRMSE results. At five OSEM iterations, using our PCDE method, the overall NRMSEs were considerably reduced by 57.5, 71.1, and 56.1 [%] in the parametric K_1, k_2, and k_3 images, respectively.

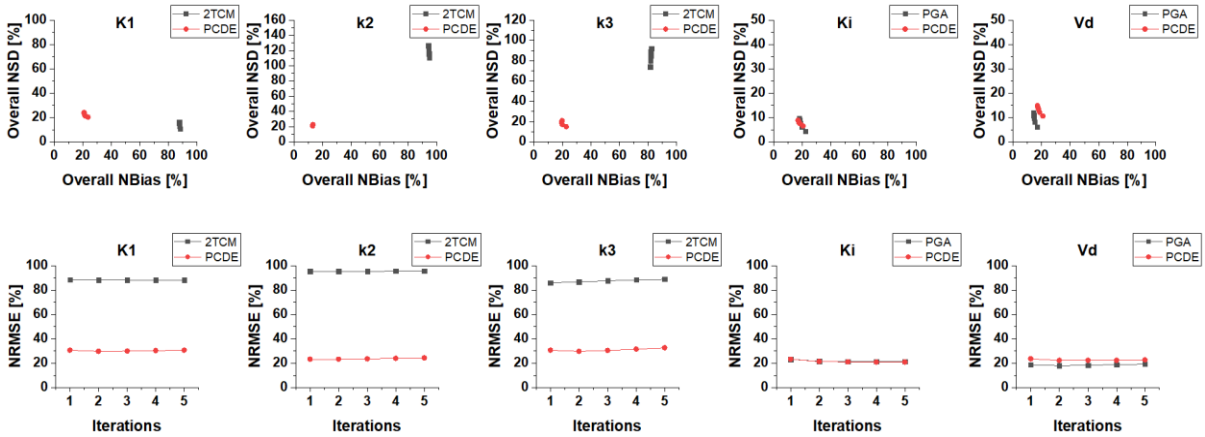

Figure 3- 7. Overall NBias-NSD tradeoff (i.e., first row) and NRMSE with OSEM iterations (i.e., second row) for each parametric image. Micro-parameters: first three columns; Macro-parameters: last two columns.

3.3.1.2. Kinetic Macro-parameters

Figures 3-8 and 9 show the ROI-based NBias-NSD tradeoff and NRMSE results for the parametric K_i and V_d images, respectively. No significant differences between the LSE-based PGA and PCDE were observed. For V_d, the PGA shows a slightly better performance, but the differences are less than 10 [%] in most cases.

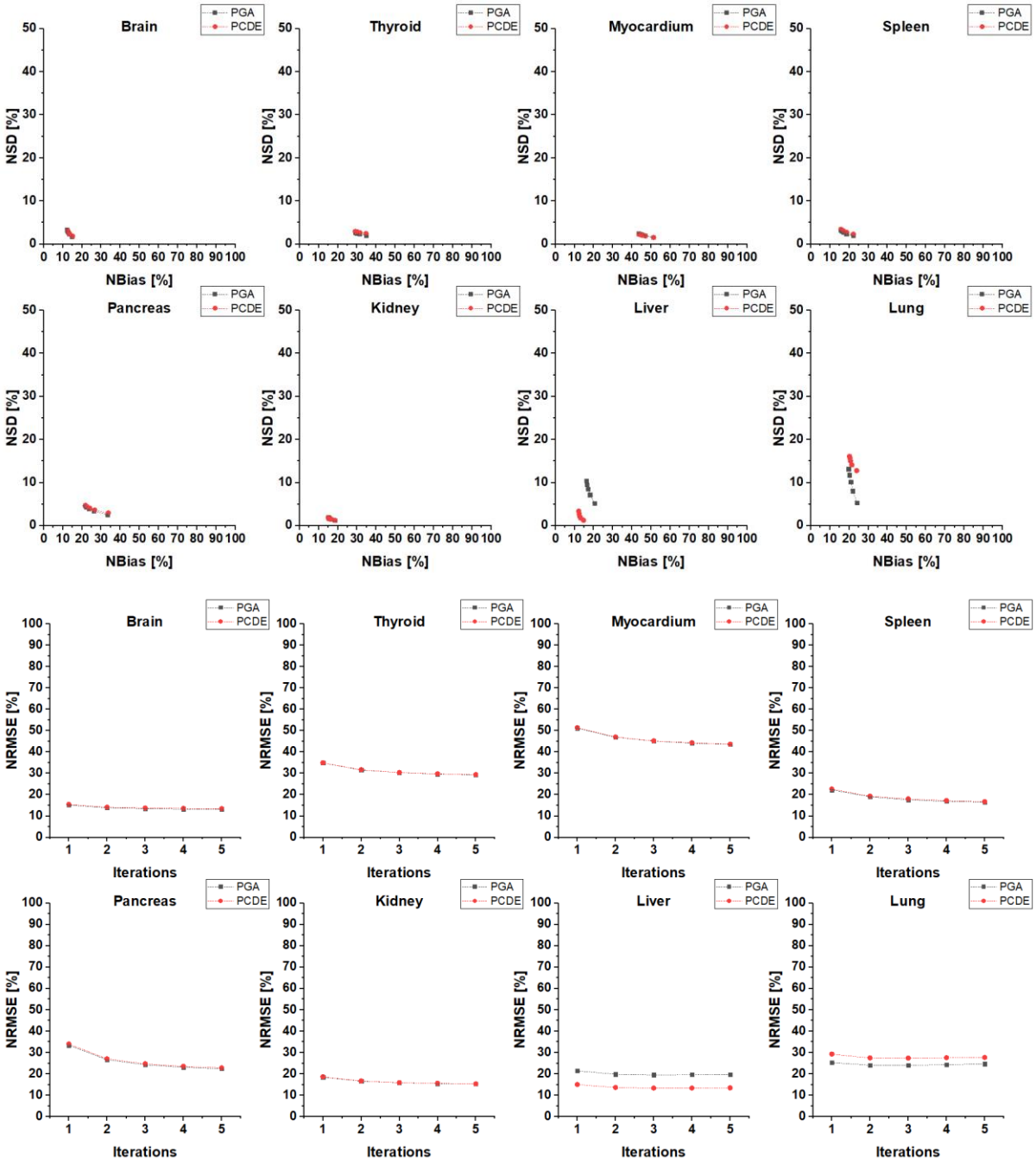

Figure 3- 8. ROI-based NBias-NSD tradeoff (i.e., upper two rows) and NRMSE with OSEM iterations (i.e., lower two rows) for parametric K_i images.

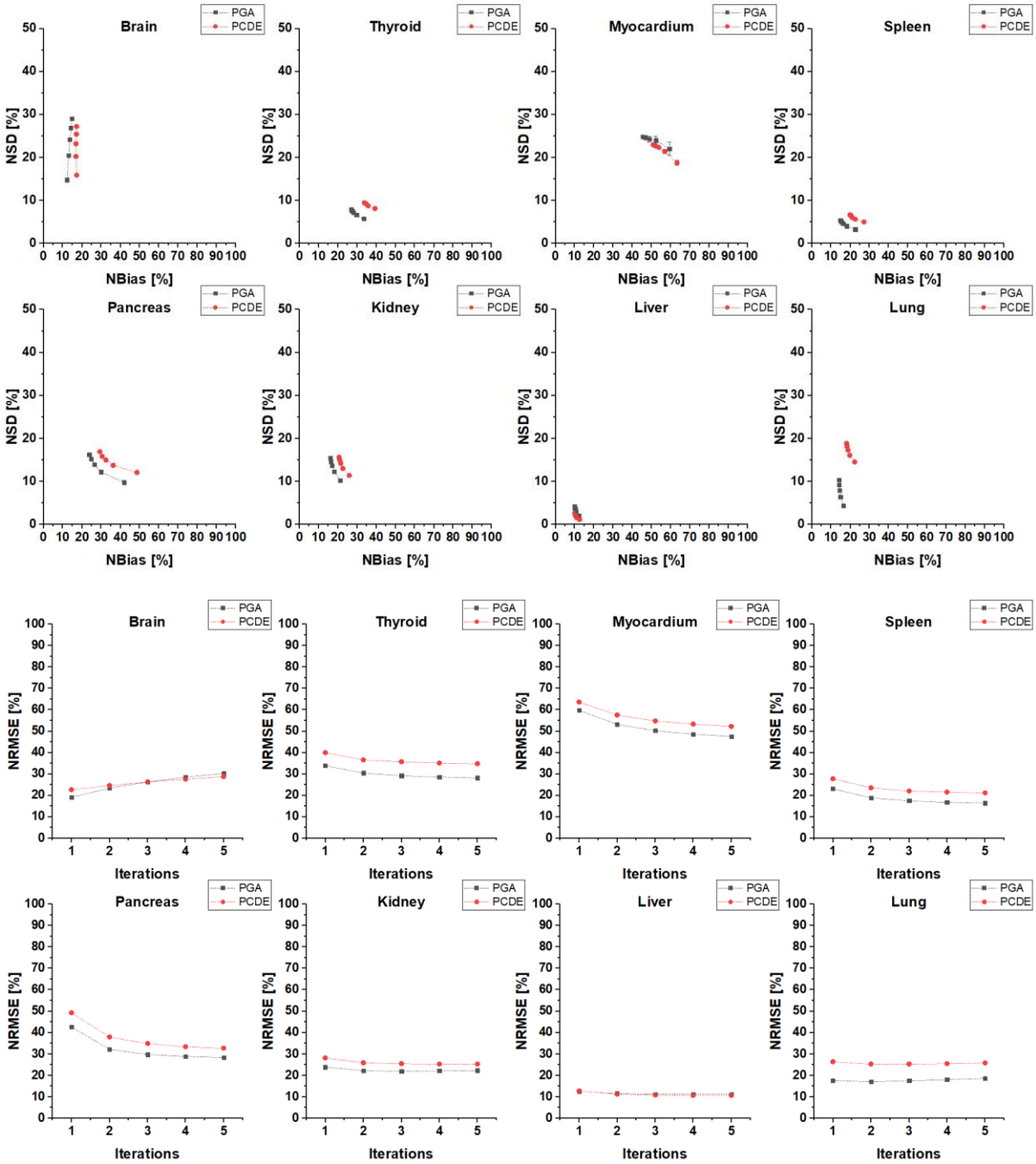

Figure 3- 9. ROI-based NBias-NSD tradeoff (i.e., upper two rows) and NRMSE with OSEM iterations (i.e., lower two rows) for parametric V_d images.

Figure 3-7 shows the overall NBias-NSD tradeoff and NRMSE. At five OSEM iterations, using our proposed PCDE method, the overall NRMSE for K_i was reduced by 0.4 [%]. However, the overall NRMSE for V_d was increased by 3.3 [%], indicating no significant difference between the two methods.

3.3.2. Overall Visibility and Tumor Detectability

3.3.2.1. Kinetic Micro-parameters

The first three columns of Figure 3-10 show the overall visibility results for the parametric K_1, k_2, and k_3 images. After five OSEM iterations, the overall SNR increased by 0.2, 4.1, and 2.4, and the overall $NSD_{spatial}$ decreased by 0.2, 5.4, and 4.1 for the parametric K_1, k_2, and k_3 images, respectively, indicating excellent performance of our proposed method in both aspects simultaneously.

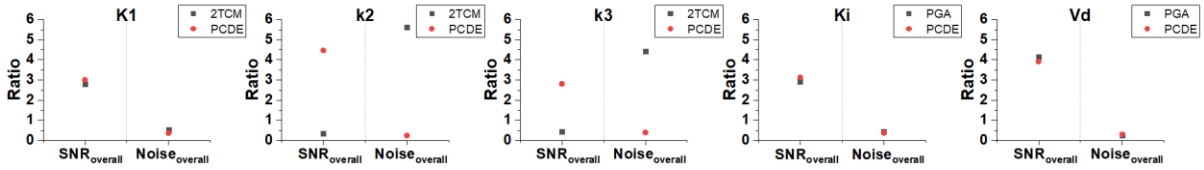

Figure 3- 10. Overall visibility in each parametric image. Micro-parameters: first three columns; Macro-parameters: last two columns. (OSEM iterations=5). Matrices: overall SNR and $NSD_{spatial}$.

The first three columns of Figure 3-11 show the tumor detectability results for each tumor in the parametric K_1, k_2, and k_3 images. After five OSEM iterations, although there was no clear improvement in CNR in the k_2 images from the proposed method, the CNR for a lung tumor increased by 1.3 and 1.0, and that for a liver tumor increased by 1.2, and 9.8 in the K_1 and k_3 images, respectively. In addition, the RE_{TBR} of a lung tumor decreased by 17.5, 82.2, and 68.4, and that of the liver tumor decreased by 255.8, 1733.5, and 80.3 [%] in the K_1, k_2, and k_3 images, respectively.

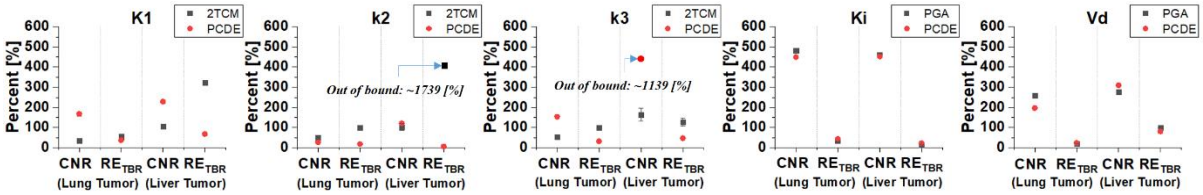

Figure 3- 11. Tumor detectability in each parametric image. Micro-parameters: first three columns; Macro-parameters: last two columns. Matrices: CNR [%] and RE_{TBR} [%]. (OSEM iterations=5).

3.3.2.2. Kinetic Macro-parameters

The last two columns of the figure 3-10 show the overall visibility results for the parametric K_i and V_d images. There were no substantial differences between the two methods in either aspect. The last two columns of Figure 3-11 show the tumor detectability results for each tumor in the parametric K_i and V_d images. For both tumors, the differences in CNR were within 0.5, and the differences in RE_{TBR} were within 10 [%] in most cases, except for the case with a decrease in RE_{TBR} by 19.6 [%] for a liver tumor in the V_d images using the proposed method.

3.4. Discussion

This study introduces our proposed method (i.e., PCDE) and compares it to the common standard parameter estimation method for kinetic modeling invoking LSE. The comparison study was performed on virtual dynamic dataset and focusing on two aspects:1) general image quality for major normal organs in WB, and 2) overall visibility and tumor detectability.

First, we verified that PCDE could improve the quality of micro-parametric images (i.e., NBias, NSD, and NRMSE). For the K_1 image, the LSE-based 2TCM showed better results in terms of NSD. However, the considerably higher level of bias compared to PCDE resulted in a larger NRMSE, reducing the overall performance compared to PCDE. Moreover, because multiple local minima can cause variability (e.g., NSD or $NSD_{spatial}$) with high bias, the lower level of NSD from

the LSE-based 2TCM could be due to the local minimum issue of LSE[85–87] instead of the actual benefit of LSE for K_1 images. Figure 3-12 shows the example of an erroneously lower level of $NSD_{spatial}$ with high bias in the K_1 image generated from the LSE-based 2TCM. When considering that NBias through the LSE-based 2TCM show an extremely high bias (i.e., 96.6 [%]), we can indirectly expect that the lower level of $NSD_{spatial}$ is caused by the local minimum issue rather than the improved performance of LSE.

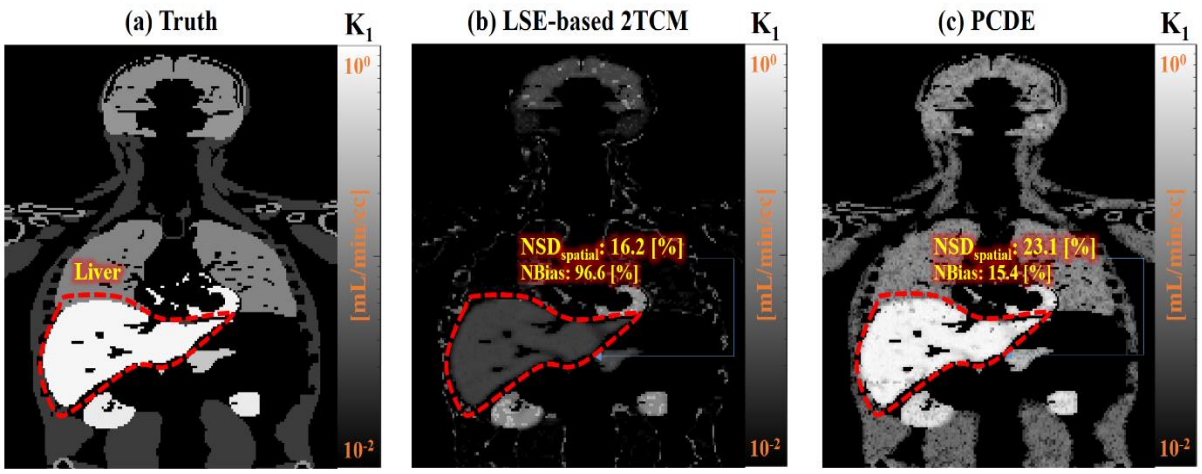

Figure 3- 12. Example of an erroneously lower level of $NSD_{spatial}$ with high bias in the LSE-based 2TCM K_1 image mainly due to the local minimum issue. (OSEM iterations=5, Noise realization index=1). Note that unlike $NSD_{spatial}$, each NBias values were calculated from all noise realizations.

For macro-parameters, there was no significant difference between the PCDE and LSE-based PGA. This was expected because the relative benefit of PCDE compared to the reference (i.e., LSE-based PGA) would not be significant because the macro-parameter estimation from the reference method already has good accuracy (i.e., NBias) and precision (i.e., NSD) owing to the linearized fit-type function for PGA[60,61].

In addition, we verified the improved overall visibility (i.e., overall SNR, overall $NSD_{spatial}$) and tumor detectability (i.e., CNR, RE_{TBR}) in the micro-parametric images, except for CNRs in k_2 images. For k_2 images, there was a negligible difference between the two methods (i.e., ≤ 0.5).

However, a high positive bias of the tumor, high negative bias of the background, and erroneously zero-like $NSD_{spatial}$ originating from the local minimum issue of LSE may highly mislead CNR value (i.e., erroneously high CNR), which cannot provide any actual benefit for tumor detectability on images. Thus, a comparison based solely on CNR may lead to incorrect conclusions regarding tumor detection capability.

Figure 3-13 shows the example of a misleading CNR and the necessity of RE_{TBR} for a fair comparison in this simulation study. Even though the CNR from the reference shows a slightly better CNR than that of PCDE (i.e., CNR_{ref}=1.8, CNR_{PCDE}=1.5), there is no actual relative benefit from the reference method in terms of tumor detection. Moreover, the relatively better CNR originates from high levels of bias in the liver tumor and background (i.e., highly negative bias) as shown in the figure.

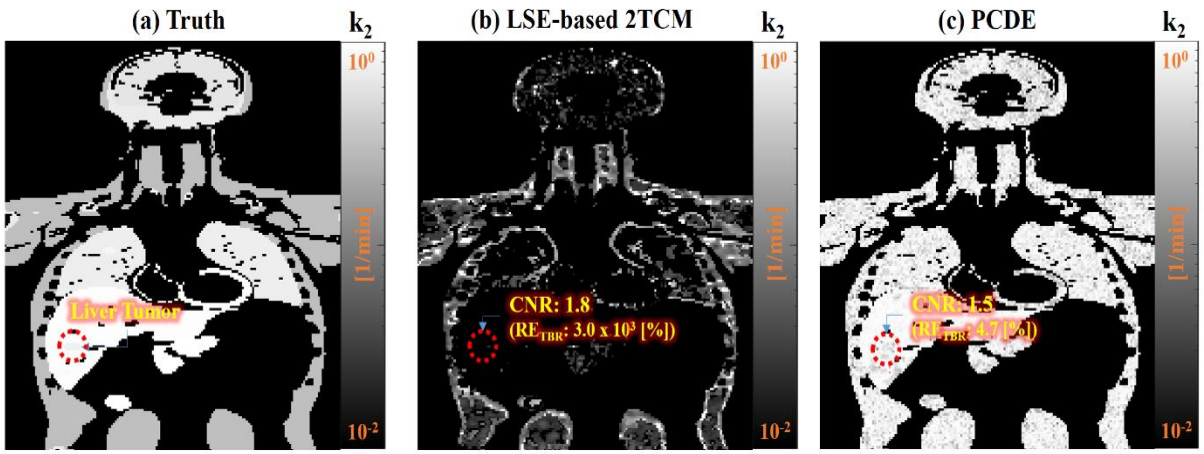

Figure 3- 13. Example of a misleading CNR and necessity of RE_{TBR} for a fair comparison. (a): Ground Truth. (b): LSE-based 2TCM. (c): PCDE. (OSEM iterations=5, Noise realization index=1, Kinetic parameter: k_2).

Therefore, in this study, we included RE_{TBR} as an auxiliary measure to minimize the possibility of incorrect conclusions regarding tumor detection capability. Considering that PCDE showed much lower RE_{TBR} values even for cases where the CNRs were quite similar (due to the misleading CNR

from the reference method), we expect improved tumor detectability through PCDE compared to that of the reference.

With micro-parametric images from PCDE (e.g., Figure 3-14), improving the overall SNR and $NSD_{spatial}$ would help identify suspicious regions in WB globally (i.e., global inspection). The improved CNR and RE_{TBR} performance would directly lead to improved tumor detectability locally within a particular organ (i.e., local inspection). For the macro-parameters (e.g., Figure 3-15), there were no significant differences in the overall visibility and tumor detectability between the two methods. This is understandable because the two methods had no significant differences in general image quality (i.e., NBias, NSD, and NRMSE).

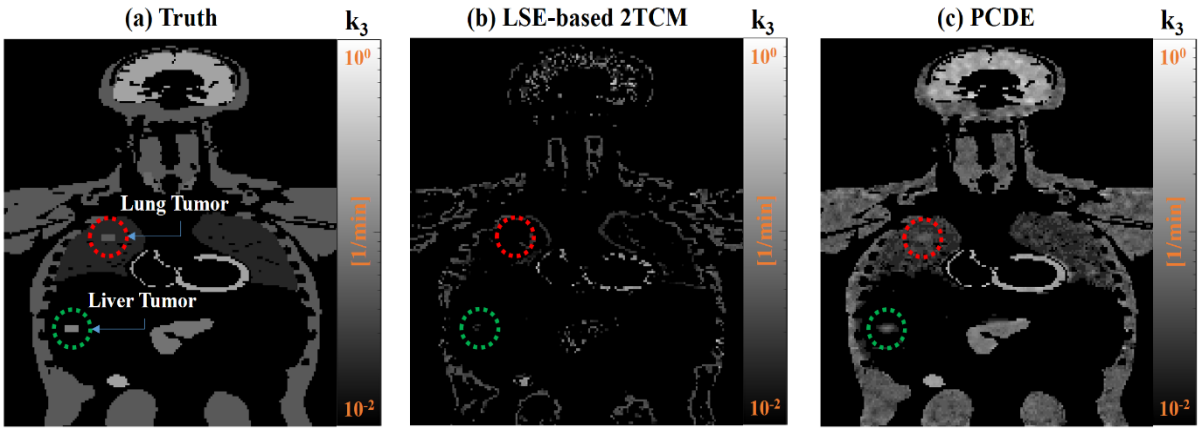

Figure 3- 14. Parametric k_3 images with five OSEM iterations. (a): Ground Truth. (b): LSE-based 2TCM. (c): PCDE. (OSEM iterations=5, Noise Realization index=1).

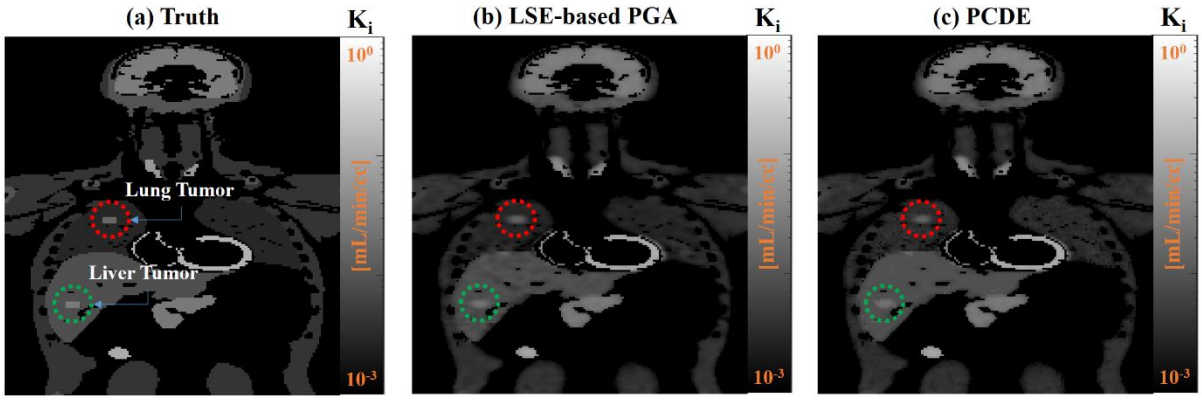

Figure 3- 15. Parametric K_i images with five OSEM iterations. (a): Ground Truth. (b): LSE-based PGA. (c): PCDE. (OSEM iterations=5, Noise Realization index=1).

Overall, our proposed PCDE method provides enhanced micro-parametric images in terms of general image quality, overall visibility, and tumor detectability.

This study contributes to typical PET scanner-based WB kinetic modeling (i.e., multi-pass protocols on a limited axial FOV) in three aspects:1) minimization of adverse effects of the previously optimized WB scan protocol for macro-parameter, 2) potential applicability for shorter scan durations, and 3) avoidance of the local minimum issues discussed above.

For the first point, the protocol proposed by Karakatsanis et al.[68,69] was optimized based on macro-parametric images (i.e., K_i) and was used 6 min after injection to scan the cardiac region. Because the macro-parameters of PGA only require data after the mechanism reaches kinetic equilibrium[68,88,89], the loss of early dynamics of TAC would not adversely affect parameter estimation. However, unlike macro-parameters, early dynamics are critical for micro-parameter estimation because they typically include near-peak data considerably influenced by micro-parameter combinations. Although the accuracy and precision of the micro-parameter estimation need to be improved further relative to those of the macro-parameter (i.e., Figure 3-7), it offers increased improvements for each micro-parameter compared to the common standard. This indicates a substantial reduction in the adverse effects of the protocol favorably optimized for macro-parameter estimation.

In addition, for the second point, the comprehensive comparison based on the multi-aspect of TAC can offer more stabilized parameter estimation (i.e., less variation of performance) from various image acquisition-related factors (e.g., the number of passes, time interval, voxel position, noise level, and type), compared to the case considering only one single factor (e.g., SSE for LSE). Therefore, we expect our proposed method to perform better even when using a dynamic PET dataset scanned only for 30 min, realistically achieving the shortest scan duration for a typical PET scanner-based WB kinetic modeling for micro-parameter estimation.

All results reported in this study are based on a simulated dynamic dataset scanned only 40 min PI, which is 5 min shorter than the optimal acquisition length suggested by Karakatsanis et al. (i.e., 45 min) and 20 min shorter than the typical time required for dynamic PET acquisition[62] for kinetic

modeling (i.e., 60 min). Hence, we can expect the promising applicability of the proposed method to studies involving shorter scan duration.

Moreover, the PCDE avoids the local minimum issue by systematically evaluating various aspects of TAC and selecting the best parameter combination, rather than relying on an iterative approach to find an optimal value. Consequently, unlike the LSE method, the PCDE does not necessitate an initial guess for parameter estimation. However, PCDE also uses curve fitting to model a measured TAC, but the later dynamics of TAC (e.g., >10 min after injection) can be well-fitted using a single exponential function (i.e., fit-type function: $\mathrm{c} - a \cdot e^{-bt}$, fit parameter: a, b, c), which can be an automatic process without a manual initial guess because of its negligible dependence on the initial values.

Tackling the local minimum issue is critical for the active use of kinetic modeling in clinics for two reasons. First, it is not necessary to set starting points for each voxel (i.e., voxel-wise computation) or ROIs (i.e., ROI-based computation). Compared to curve fitting for the later dynamics of TAC (i.e., a single exponential shape), curve fitting for the entire dynamics of TAC (i.e., a surge-like shape) is most likely to have starting point dependency, especially if near-peak data are missing either partially or completely. Thus, for clinical use, starting points must be set subtlety through repetition to minimize the adverse effects of the local minimum issue (i.e., finding a global minimum), which is time-consuming when performed for each voxel or ROI, preventing the routine application of kinetic modeling in the clinic. Second, by minimizing the starting point dependency, the interpersonal error of the estimated kinetic parameters can be considerably reduced, which is critical for the consistency of kinetic modeling results and large-scale data comparison across different institutions worldwide.

Nevertheless, a couple of limitations in our proposed method indicate the need for further studies. First, the computational speed of PCDE is approximately 1.1×10^{-3} s/voxel; therefore, approximately 2 h are needed to perform WB kinetic modeling for a typical volume size in the clinic (i.e., $256 \times 256 \times 409$) with plain hardware specifications (e.g., CPU: AMD Ryzen 9 5900HX, RAM: 32.0 GB, platform: MATLAB R2021b, resolution of estimated parameter: 0.01). For use in routine practice, at least 100 times the current computational speed (i.e., ~10^{-5} s/voxel)

is needed to complete the computation in a few minutes. Parallelized computation using a graphical processing unit (GPU) will allow us to achieve this.

Second, in this study, we limited the maximum allowable value of the micro-parameter to 1 (for K_1 and k_2) and 0.5 (for k_3), respectively. Although for ^{18}F-FDG, almost all micro-parameters for each ROI in WB were within the desired ranges[68,71], we need to broaden the range to increase applicability to diverse types of radiotracers.

Third, depending on a specific radiotracer of interest or research focus, the reversible uptake (i.e., $k_4 \neq 0$) may be of greater interest, than the irreversible process; hence, a performance test under the reversible process would be needed.

Therefore, with the addition of a reversible process and a broader range of parameters, we anticipate that the GPU-accelerated PCDE approach will enable the widespread use of typical PET scanner-based whole-body kinetic modeling for kinetic micro-parameters. This method ensures both reasonable computational time and compatibility with various types of radiotracers.

Furthermore, despite significant improvements via PCDE, the overall levels of NBias and NSD tend to be beyond 10% (i.e., near 20%), and non-negligible variations among ROIs exist (e.g., supplemental Figures 1-7), implying that the proposed method may still be insufficient for use in routine practice. We expect that the exploitation of de-noising techniques such as the finite Legendre transform-based low-pass filter with excellent de-noising performance for the exponential type curve (i.e., typical shape of TAC after peak) without the phase shift[90] and/or noise propagation pattern learning through machine/deep learning algorithms (i.e., noise propagation from the sinogram domain into image domain) could reduce the overall levels of NBias and NSD within 10%. Moreover, it can reduce variations among ROIs (i.e., consideration of different noise propagation patterns at each position).

Finally, a validation study based on real patient data should be conducted. We are actively collecting patient data (e.g., Clinical Trial ID: NCT04017104) categorized by a specific tumor detection mechanism such as ^{18}F-FDG by glucose metabolism[91], ^{18}F-DCFPyL and ^{68}Ga-HTK by targeting a prostate-specific membrane antigen (PSMA)[92,93], and ^{18}F-AmBF3 by targeting

somatostatin receptor 2 (SSTR2)[94]. We expect to perform a validation study based on real patient data in the near future.

Chapter 4. Application of the PCDE Method to Patient Datasets

In this chapter, we implemented our proposed method PCDE on patient datasets to further verify clinical applicability of the method. While we already verified improved performance in micro-parametric images compared to reference method (i.e., 2TCM) in previous chapter, the results were based on virtual dynamic datasets, which could have noise type, pattern, and level at least somewhat different from actual pattern on patient datasets. Hence, performance testing based on real patient datasets was further conducted focusing on 1) overall visibility, and 2) lesion detectability.

4.1. Information on Patient Datasets

We test our method on 8 patients for 4 different types of radiotracers (i.e., 2 patients for each tracer) as a pilot study. Table 4-1 shows the summary of characteristics of each radiotracer used in this study. In addition, dynamic scanning protocols for each tracer are summarized in Tables 4-2, 4-3, 4-4, and 4-5, respectively.

Table 4- 1. Summary of radiotracers used for our patient data.

Radiotracer type	Half-life	Mechanism
^{18}F-DCFPyL	109 min	Targeting PSMA
^{68}Ga-HTK	68 min	Targeting PSMA
^{18}F-FDG	109 min	Glucose metabolism
^{18}F-AmBF3	109 min	Targeting SSTR2

PSMA: prostate-specific membrane antigen, SSTR2: somatostatin receptor 2.

Table 4- 2. Dynamic scanning protocols for ^{18}F-DCFPyL.

Item	Patient #1	Patient #2

Injected activity	9.14 mCi	7.16 mCi
Scanner	GE Discovery MI	GE Discovery MI
Dimensions	256 x 256 x 409	256 x 256 x 409
Voxel size	2.73 x 2.73 x 2.8 mm^3	2.73 x 2.73 x 2.8 mm^3
Total acquisition time (cardiac + whole-body)	87 min	92 min
Image acquisition for whole-body	7-87 min	9-92 min
Time interval	5 min	5 min
# of passes	16	16
# of beds	6	6

Table 4- 3. Dynamic scanning protocols for ^{68}Ga-HTK.

Item	Patient #1	Patient #2
Injected activity	3.71 mCi	5.25 mCi
Scanner	GE Discovery MI	GE Discovery 690
Dimensions	192 x 192 x 409	192 x 192 x 335
Voxel size	2.73 x 2.73 x 2.8 mm^3	3.65 x 3.65 x 3.27 mm^3
Total acquisition time (cardiac + whole-body)	55 min	48 min
Image acquisition for whole-body	7-55 min	7-48 min
Time interval	7 min	14 min
# of passes	7	3
# of beds	6	9

Table 4- 4. Dynamic scanning protocols for ^{18}F-FDG.

Item	Patient #1	Patient #2
Injected activity	10.16 mCi	6.46 mCi
Scanner	GE Discovery 690	GE Discovery 690
Dimensions	192 x 192 x 299	192 x 192 x 263
Voxel size	3.65 x 3.65 x 3.27 mm^3	3.65 x 3.65 x 3.27 mm^3
Total acquisition time (cardiac + whole-body)	57 min	61 min
Image acquisition for whole-body	26-57 min	27-61 min

Time interval	6 min	6 min
# of passes	5	6
# of beds	8	7

Table 4- 5. Dynamic scanning protocols for ^{18}F-AmBF3.

Item	Patient #1	Patient #2
Injected activity	9.49 mCi	6.8 mCi
Scanner	GE Discovery 690	GE Discovery 690
Dimensions	192 x 192 x 263	192 x 192 x 299
Voxel size	3.65 x 3.65 x 3.27 mm^3	3.65 x 3.65 x 3.27 mm^3
Total acquisition time (cardiac + whole-body)	63 min	66 min
Image acquisition for whole-body	7-63 min	8-66 min
Time interval	6 min	7 min
# of passes	10	9
# of beds	7	8

4.2. Quantitative Evaluation Criteria

The quantitative evaluation of parametric images based on patient dynamic datasets was performed, including analysis of: 1) overall visibility relevant to the identification of suspicious lesions in WB (i.e., global inspection), and 2) overall lesion detectability within a particular organ (i.e., local inspection).

Similar to chapter 3 (i.e., performance test based on virtual dynamic datasets), overall SNR was used as a measure of the visibility, and overall CNR and TBR were used as a measure of lesion detectability. The metrics are defined as follows.

$$\mathrm{SNR} = \frac{\bar{f}_{ROI}}{\sigma_{ROI}} \tag{4.1}$$

$$\mathrm{CNR} = \frac{\left|\bar{f}_{ROI} - \bar{f}_{BKG.}\right|}{\sigma_{BKG.}} \tag{4.2}$$

$$\mathrm{TBR} = \frac{\bar{f}_{lesion}}{\bar{f}_{BKG.}} \tag{4.3}$$

where $\bar{f}_{ROI}$, $\bar{f}_{BKG.}$, and $\bar{f}_{lesion}$ denote the averaged voxel value of the ROI, background and lesion, respectively. σ_{ROI} and $\sigma_{BKG.}$ represent the standard deviation of all voxels in the ROI and background, respectively.

To evaluate overall performance, the overall SNR, CNR, and TBR were defined as the volume-weighted averages of the individual ROIs metrics[68,69]. The summarized ROI volumes of patients for each tracer are presented in Table 4-6, 7, 8, and 9, respectively.

Among 8 patients, 3 patients had tumors. Subsequently, overall CNR and TBR of one patient for each radiotracer was analyzed: 1) ^{18}F-DCFPyL: patient #1, 2) ^{68}Ga-HTK: patient #1, and 3) ^{18}F-FDG: patient #1. The ROIs of all lesions for each patient were defined and confirmed by a nuclear medicine physician.

Table 4- 6. Summary of ROI volumes of patients for ^{18}F-DCFPyL.

	ROI volume [cc]				
	Liver	Kidney	Salivary gland	Lesion 1	Lesion 2
Patient #1	1208.11	119.07	34.53	0.55	0.31
Patient #2	1246.76	94.48	23.37	none	

Table 4- 7. Summary of ROI volumes of patients for ^{68}Ga-HTK.

	ROI volume [cc]			
	Liver	Kidney	Salivary gland	Lesion 1
Patient #1	1109.23	92.01	14.56	1.34
Patient #2	933.82	144.23	21.00	none

Table 4- 8. Summary of ROI volumes of patients for ^{18}F-FDG.

	ROI volume [cc]							
	Liver	Kidney	Salivary gland	Lesion 1	Lesion 2	Lesion 3	Lesion 4	Lesion 5

Patient #1	1067.55	79.56	13.16	2.92	1.45	0.31	1.26	1.39
Patient #2	1549.15	49.68	20.69			none		

Table 4- 9. Summary of ROI volumes of patients for ^{18}F-AmBF3.

	ROI volume [cc]		
	Liver	Kidney	Salivary gland
Patient #1	1340.36	54.25	12.92
Patient #2	2125.46	87.43	18.57

4.3. Results

4.3.1. Overall Visibility

4.3.1.1. Kinetic Micro-parameters

The first three columns of Figure 4-1 show the overall visibility results of ^{18}F-DCFPyL for the parametric K_1, k_2, and k_3 images. The averaged overall SNR (i.e., average of individual patient's metric) increased by 1.19±0.25, 2.06±0.42, and 0.80±0.16 for the parametric K_1, k_2, and k_3 images, respectively.

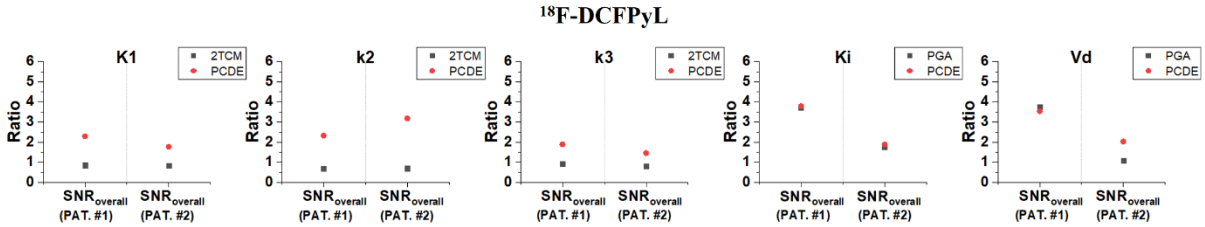

Figure 4- 1. Overall visibility in each parametric image. Micro-parameters: first three columns; Macro-parameters: last two columns. PAT.=patient. Radiotracer: ^{18}F-DCFPyL.

In addition, each first row of the Figures 4-2 and 4-3 shows examples of micro-parametric images (i.e., K_1, k_2, and k_3) for patient #1 and 2 injected with ^{18}F-DCFPyL, respectively. Overall, compared to 2TCM, better definitions with less noise via PCDE in all micro-parametric images were verified.

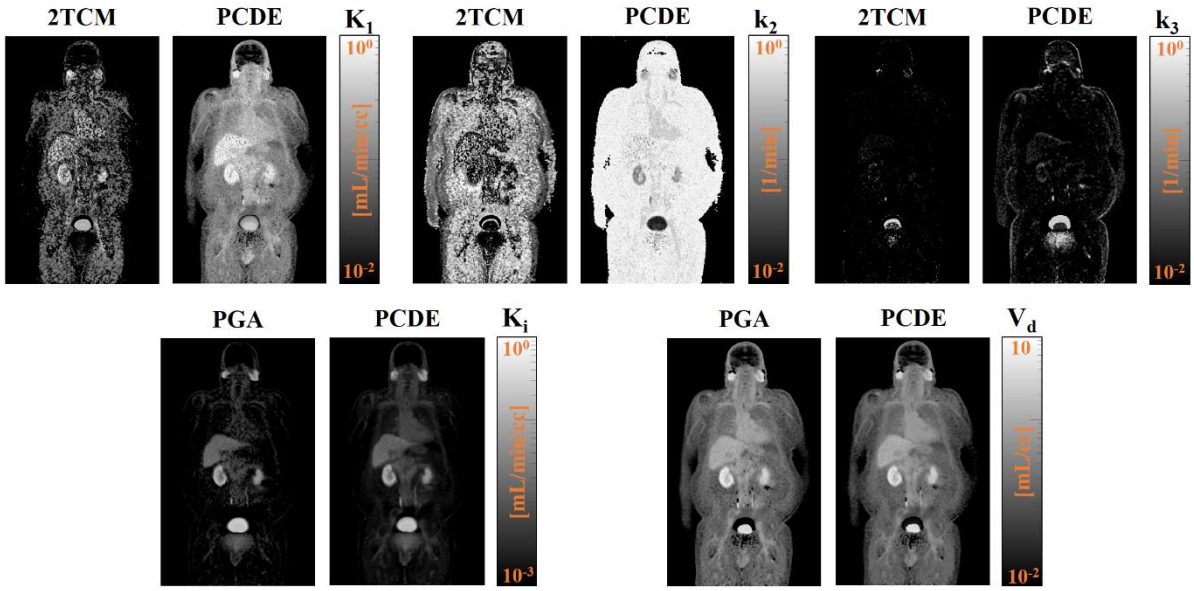

Figure 4- 2. Example of parametric images focusing on overall visibility. Micro-parameters (K_1, k_2, and k_3): the first row. Macro-parameters (K_i and V_d): the second row. Radiotracer: ^{18}F-DCFPyL (Patient #1). We showed results for conventional 2TCM approach vs. our proposed PCDE approach.

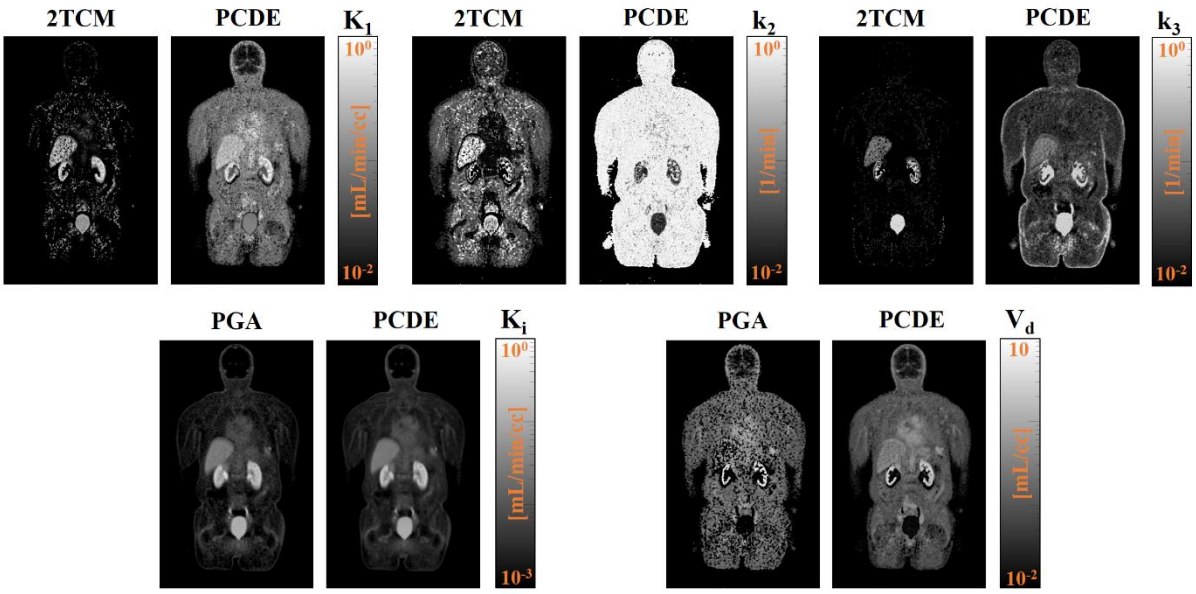

Figure 4- 3. Example of parametric images focusing on overall visibility. Micro-parameters (K_1, k_2, and k_3): the first row. Macro-parameters (K_i and V_d): the second row. Radiotracer: ^{18}F-DCFPyL (Patient #2). We showed results for conventional 2TCM approach vs. our proposed PCDE approach.

The first three columns of Figure 4-4 show the overall visibility results of ^{68}Ga-HTK for the parametric K_1, k_2, and k_3 images. The averaged overall SNR increased by 0.95±0.06, 1.41±0.04, and 0.55±0.20 for the parametric K_1, k_2, and k_3 images, respectively.

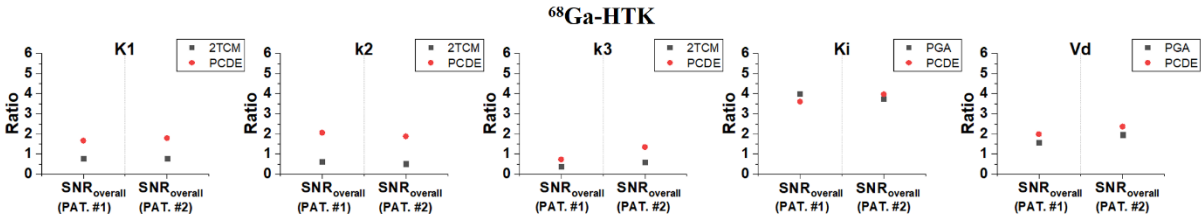

Figure 4- 4. Overall visibility in each parametric image. Micro-parameters: first three columns; Macro-parameters: last two columns. PAT.=patient. Radiotracer: ^{68}Ga-HTK.

In addition, each first row of the Figures 4-5 and 4-6 shows examples of micro-parametric images (i.e., K_1, k_2, and k_3) for patient #1 and 2 injected with ^{68}Ga-HTK, respectively. Overall, compared to 2TCM, better definitions with less noise via PCDE in all micro-parametric images were verified.

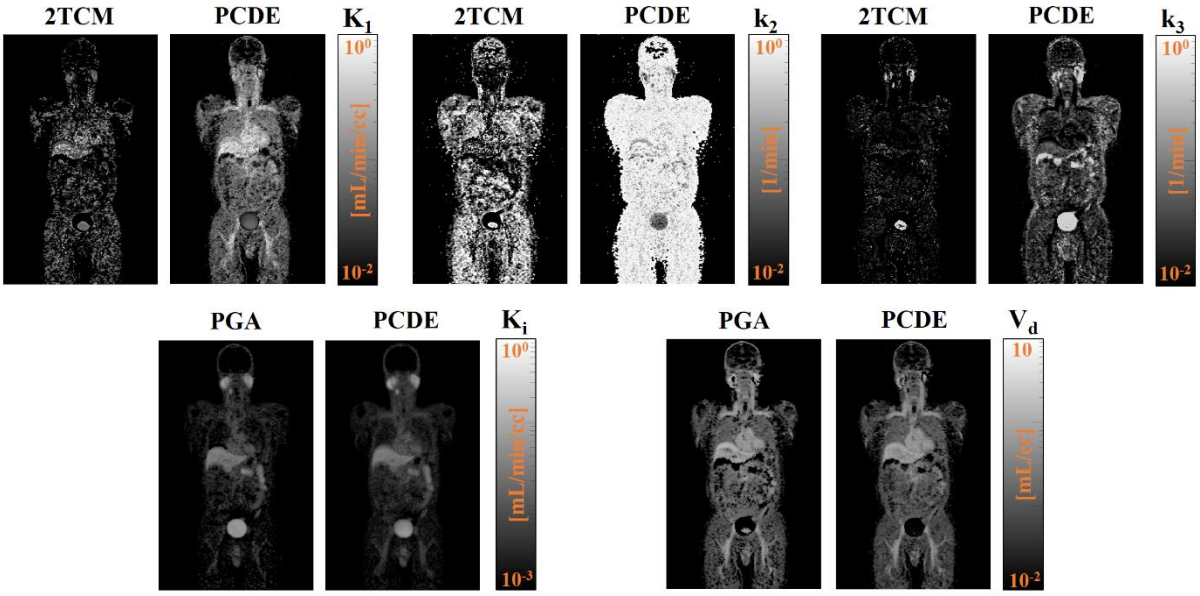

Figure 4- 5. Example of parametric images focusing on overall visibility. Micro-parameters (K_1, k_2, and k_3): the first row. Macro-parameters (K_i and V_d): the second row. Radiotracer: ^{68}Ga-HTK (Patient #1). We showed results for conventional 2TCM approach vs. our proposed PCDE approach.

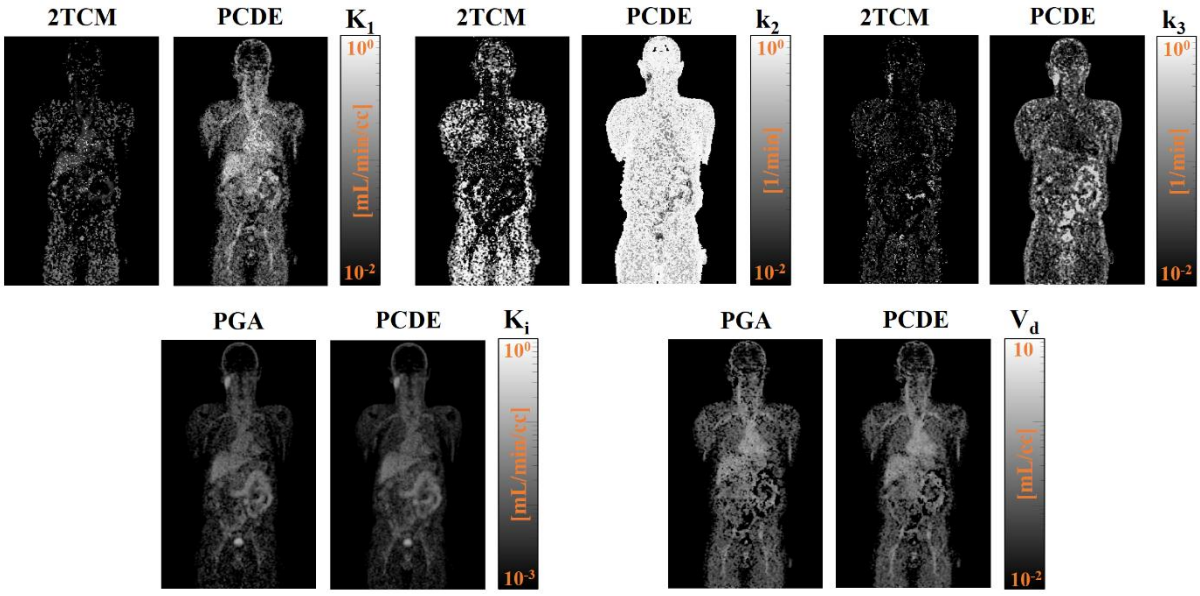

Figure 4- 6. Example of parametric images focusing on overall visibility. Micro-parameters (K_1, k_2, and k_3): the first row. Macro-parameters (K_i and V_d): the second row. Radiotracer: ^{68}Ga-HTK (Patient #2). We showed results for conventional 2TCM approach vs. our proposed PCDE approach.

The first three columns of Figure 4-7 show the overall visibility results of ^{18}F-FDG for the parametric K_1, k_2, and k_3 images. The averaged overall SNR increased by 2.00±0.21, 3.02±0.46, and 0.32±0.31 for the parametric K_1, k_2, and k_3 images, respectively.

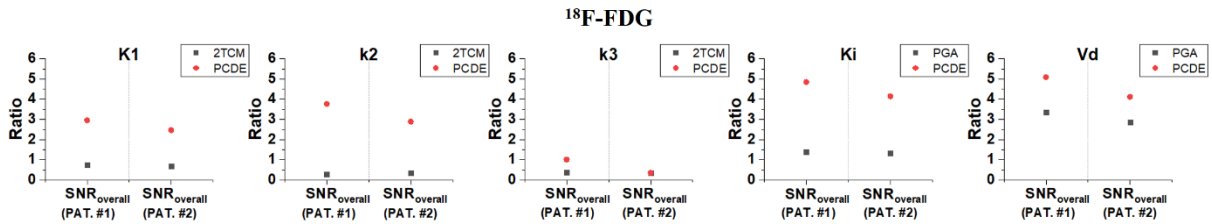

Figure 4- 7. Overall visibility in each parametric image. Micro-parameters: first three columns; Macro-parameters: last two columns. PAT.=patient. Radiotracer: ^{18}F-FDG.

In addition, each first row of the Figures 4-8 and 4-9 shows examples of micro-parametric images (i.e., K_1, k_2, and k_3) for patient #1 and 2 injected with ^{18}F-FDG, respectively. Overall, compared to 2TCM, better definitions with less noise via PCDE in all micro-parametric images were verified.

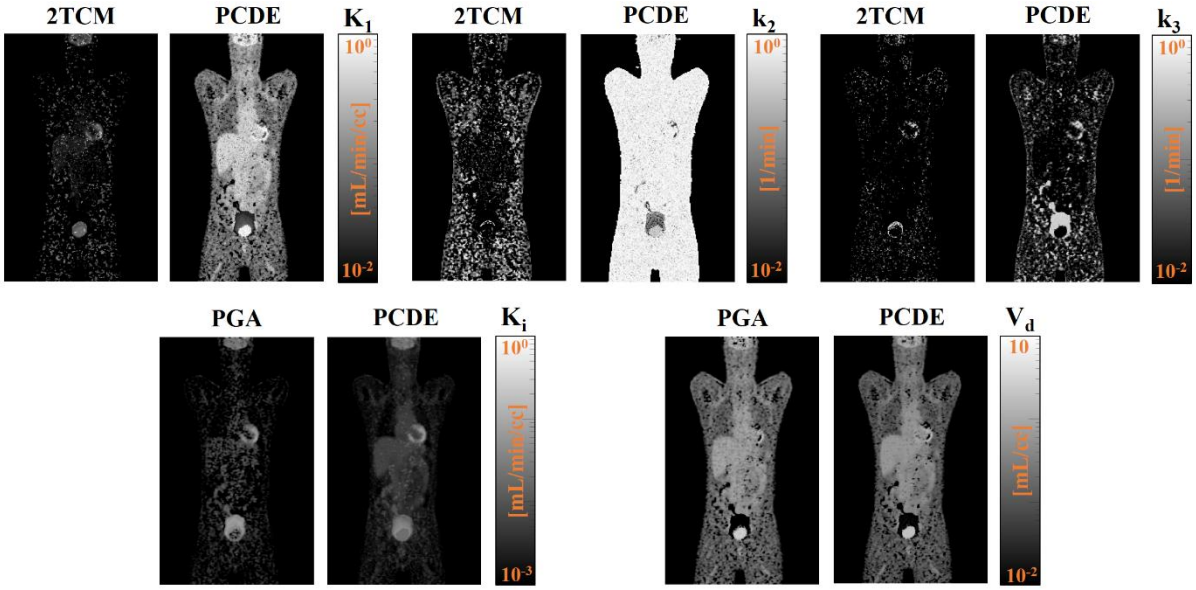

Figure 4- 8. Example of parametric images focusing on overall visibility. Micro-parameters (K_1, k_2, and k_3): the first row. Macro-parameters (K_i and V_d): the second row. Radiotracer: ^{18}F-FDG (Patient #1). We showed results for conventional 2TCM approach vs. our proposed PCDE approach.

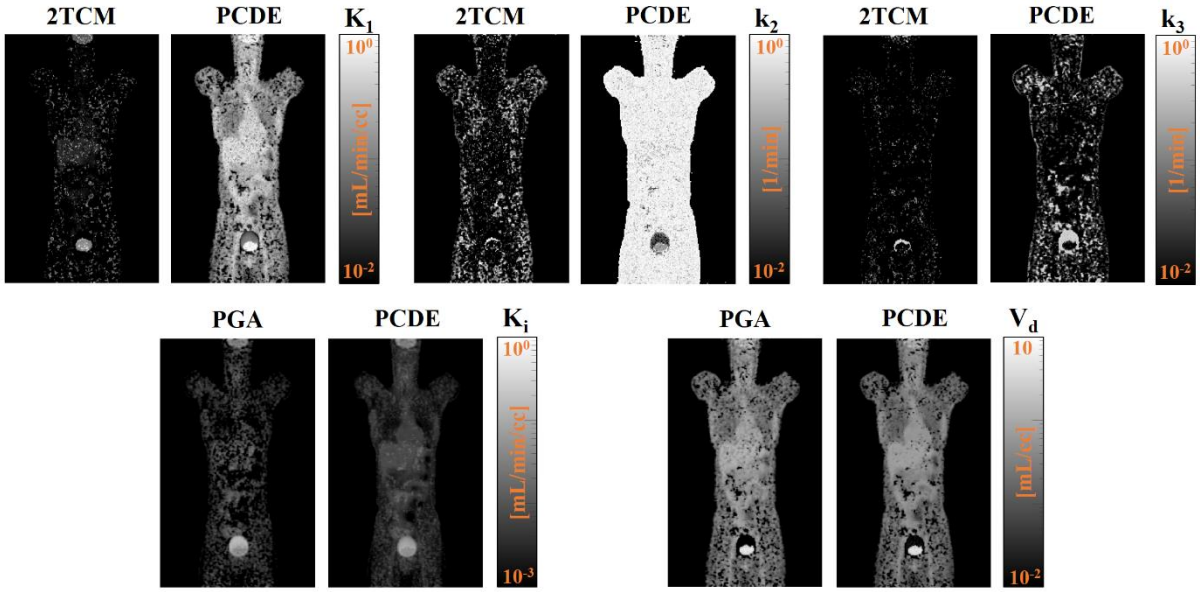

Figure 4- 9. Example of parametric images focusing on overall visibility. Micro-parameters (K_1, k_2, and k_3): the first row. Macro-parameters (K_i and V_d): the second row. Radiotracer: ^{18}F-FDG (Patient #2). We showed results for conventional 2TCM approach vs. our proposed PCDE approach.

The first three columns of Figure 4-10 show the overall visibility results of ^{18}F-AmBF3 for the parametric K_1, k_2, and k_3 images. The averaged overall SNR increased by 0.40±0.41, 0.61±0.38, and 0.47±0.10 for the parametric K_1, k_2, and k_3 images, respectively.

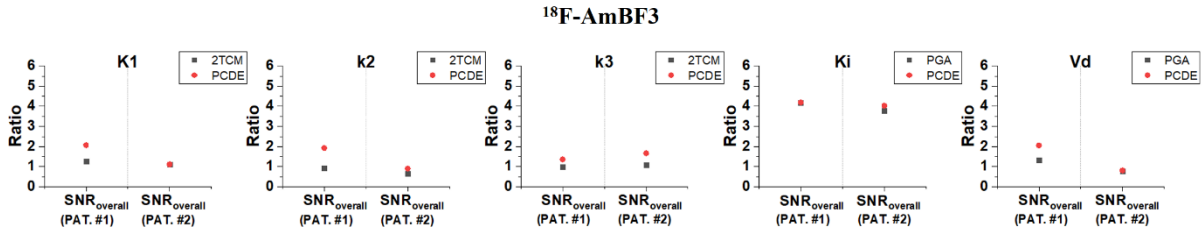

Figure 4- 10. Overall visibility in each parametric image. Micro-parameters: first three columns; Macro-parameters: last two columns. PAT.=patient. Radiotracer: ^{18}F-AmBF3.

In addition, each first row of the Figures 4-11 and 4-12 shows examples of micro-parametric images (i.e., K_1, k_2, and k_3) for patient #1 and 2 injected with ^{18}F-FDG, respectively. Overall, compared to 2TCM, better definitions with less noise via PCDE in all micro-parametric images were verified.

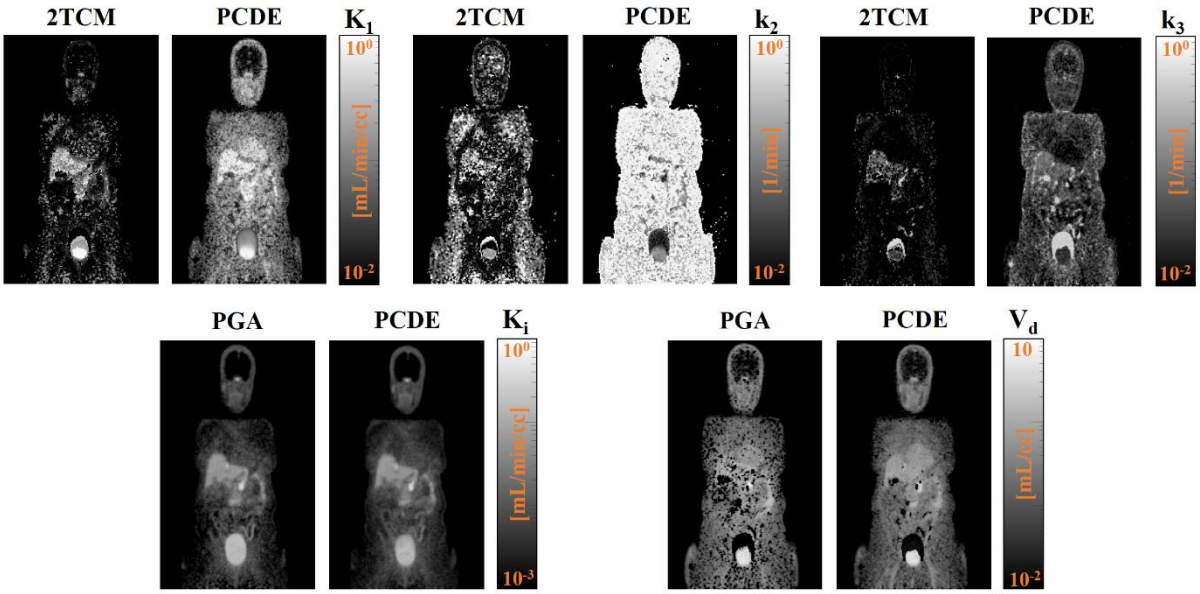

Figure 4- 11. Example of parametric images focusing on overall visibility. Micro-parameters (K_1, k_2, and k_3): the first row. Macro-parameters (K_i and V_d): the second row. Radiotracer: ^{18}F-AmBF3 (Patient #1). We showed results for conventional 2TCM approach vs. our proposed PCDE approach.

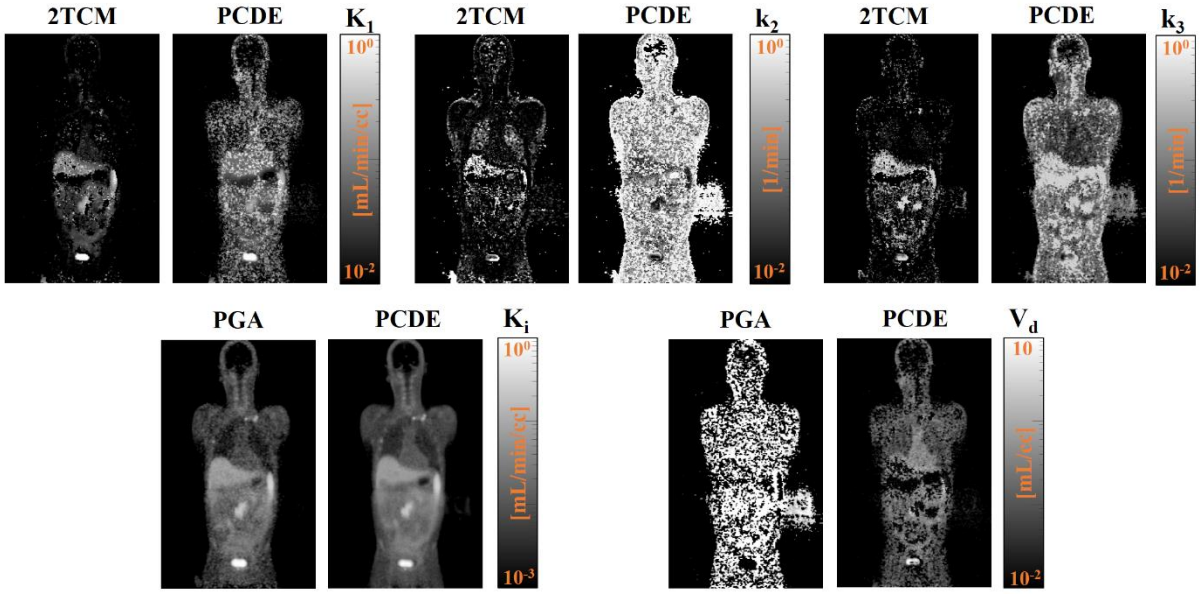

Figure 4- 12. Example of parametric images focusing on overall visibility. Micro-parameters (K_1, k_2, and k_3): the first row. Macro-parameters (K_i and V_d): the second row. Radiotracer: ^{18}F-AmBF3 (Patient #2). We showed results for conventional 2TCM approach vs. our proposed PCDE approach.

4.3.1.2. Kinetic Macro-parameters

The last two columns of Figure 4-1 show the overall visibility results of ^{18}F-DCFPyL for the parametric K_i and V_d images. The averaged overall SNR (i.e., average of individual patient's metric) increased by 0.09±0.03 and 0.37±0.58 for the parametric K_i and V_d images, respectively. In addition, each second row of the Figures 4-2 and 4-3 shows examples of macro-parametric images (i.e., K_i and V_d) for patient #1 and 2 injected with ^{18}F-DCFPyL, respectively. Overall, there were no visually significant differences between two methods (i.e., PGA vs. PCDE).

In addition, the last two columns of Figure 4-4 show the overall visibility results of ^{68}Ga-HTK for the parametric K_i and V_d images. The averaged overall SNR increased by -0.09±0.30 and 0.42±0.01 for the parametric K_i and V_d images, respectively. The minus sign represents the decrease in metric of interest. In addition, each second row of the Figures 4-5 and 4-6 shows examples of macro-parametric images (i.e., K_i and V_d) for patient #1 and 2 injected with ^{68}Ga-HTK, respectively. Overall, there were no visually significant differences between two methods (i.e., PGA vs. PCDE).

Furthermore, the last two columns of Figure 4-7 show the overall visibility results of ^{18}F-FDG for the parametric K_i and V_d images. The averaged overall SNR increased by 3.14±0.33 and 1.49±0.24 for the parametric K_i and V_d images, respectively. In addition, each second row of the Figures 4-8 and 4-9 shows examples of macro-parametric images (i.e., K_i and V_d) for patient #1 and 2 injected with ^{18}F-FDG, respectively. Overall, there were reletively larger level of differences between two methods (i.e., PGA vs. PCDE), compared to the results via ^{18}F-DCFPyL or ^{68}Ga-HTK, especially in parametric K_i images.

On top of that, the last two columns of Figure 4-10 show the overall visibility results of ^{18}F-AmBF3 for the parametric K_i and V_d images. The averaged overall SNR increased by 0.12±0.12 and 0.39±0.35 for the parametric K_i and V_d images, respectively. In addition, each second row of the Figures 4-11 and 4-12 shows examples of macro-parametric images (i.e., K_i and V_d) for patient #1 and 2 injected with ^{18}F-AmBF3, respectively. Overall, there were no visually significant differences between two methods (i.e., PGA vs. PCDE), except for the parametric V_d images for patient #2.

Overall, there were no substantial differences between the two methods in either type of parametric image. The differences in averaged overall SNR were within 0.50 except for the ^{18}F-FDG cases (i.e., increases in averaged $SNR_{overall}$: 3.14 and 1.49 for K_i and V_d, respectively).

4.3.2. Overall Lesion Detectability

4.3.2.1. Kinetic Micro-parameters

The first three columns of Figure 4-5 show the tumor detectability results of ^{18}F-DCFPyL in the parametric K_1, k_2, and k_3 images. The overall CNR increased by 2.54, 1.99, and 1.29, and the overall TBR increased by 1.21, 0.39, and 1.84 for the parametric K_1, k_2, and k_3 images, respectively, indicating excellent performance of our proposed method in both aspects simultaneously.

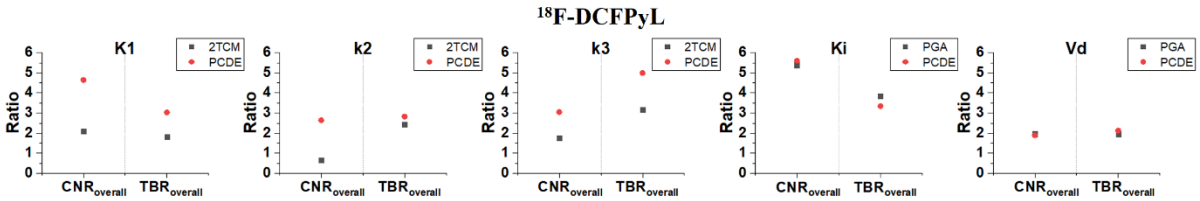

Figure 4- 13. Tumor detectability in each parametric image. Micro-parameters: first three columns; Macro-parameters: last two columns. Matrices: $CNR_{overall}$ and $TBR_{overall}$ (the # of lesions: 2). Radiotracer: ^{18}F-DCFPyL.

In addition, the Figures 4-14 presents examples of parametric K_1 and k_3 images via ^{18}F-DCFPyL, respectively. Compared to reference method (i.e., 2TCM), the enhanced lesion detectability was verified via PCDE.

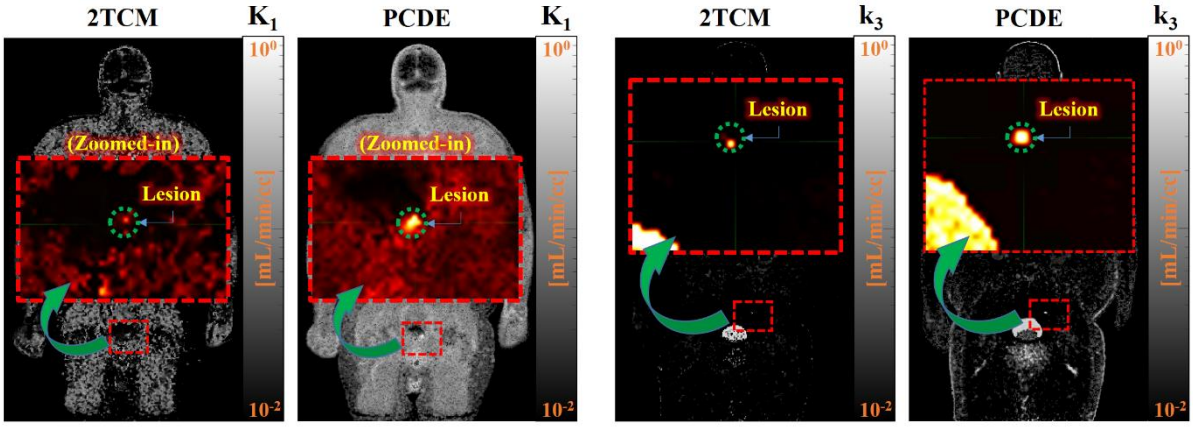

Figure 4- 14. Examples of parametric images focusing on lesion detectability. Micro-parameter: K_1 (lesion #1) and k_3 (lesion #2). Radiotracer: ^{18}F-DCFPyL (Patient #1).

In addition, the first three columns of Figure 4-6 show the tumor detectability results of ^{68}Ga-HTK in the parametric K_1, k_2, and k_3 images. The overall CNR increased by 0.50, 1.14, and 0.60, and the overall TBR increased by 0.36, 1.59, and 2.00 for the parametric K_1, k_2, and k_3 images, respectively.

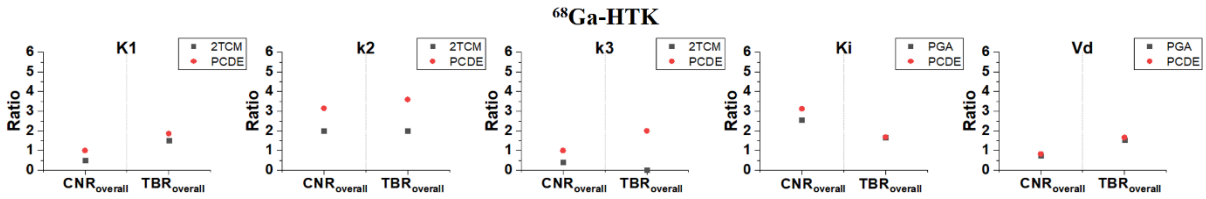

Figure 4- 15. Tumor detectability in each parametric image. Micro-parameters: first three columns; Macro-parameters: last two columns. Matrices: $CNR_{overall}$ and $TBR_{overall}$ (the # of lesions: 1). Radiotracer: ^{68}Ga-HTK.

In addition, the last two figures in Figure 4-16 present examples of parametric k_2 images via ^{68}Ga-HTK. Compared to reference method (i.e., 2TCM), the enhanced lesion detectability was verified via PCDE.

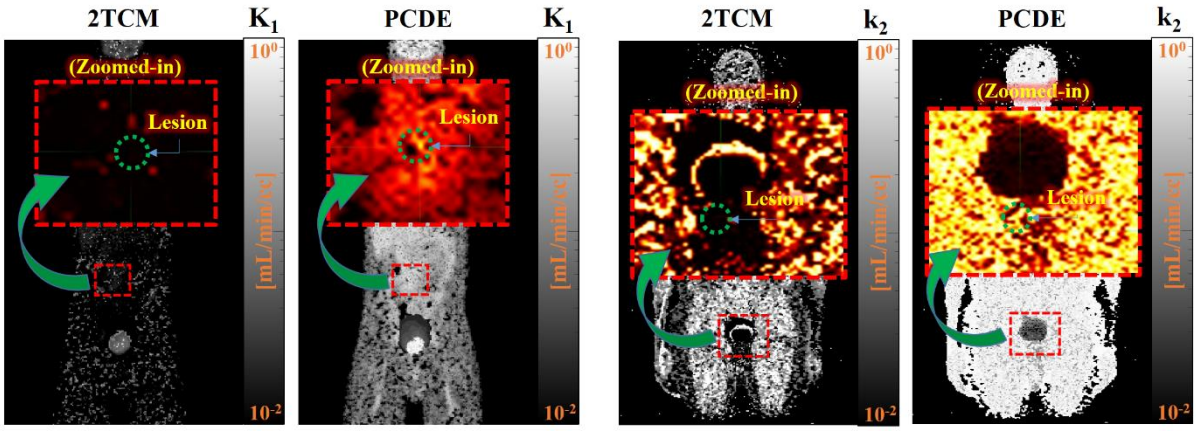

Figure 4- 16. Examples of parametric images focusing on lesion detectability. Micro-parameter: K_1 (lesion #2) and k_2 (lesion #1). Radiotracer: ^{18}F-FDG (Patient #1) and ^{68}Ga-HTK (Patient #1) for K_1 and k_2, respectively.

Furthermore, the first three columns of Figure 4-7 show the tumor detectability results of ^{18}F-FDG in the parametric K_1, k_2, and k_3 images. The overall CNR increased by 1.26, 0.88, and 0.25, and the overall TBR increased by 0.05, 0.28, and 0.28 for the parametric K_1, k_2, and k_3 images, respectively.

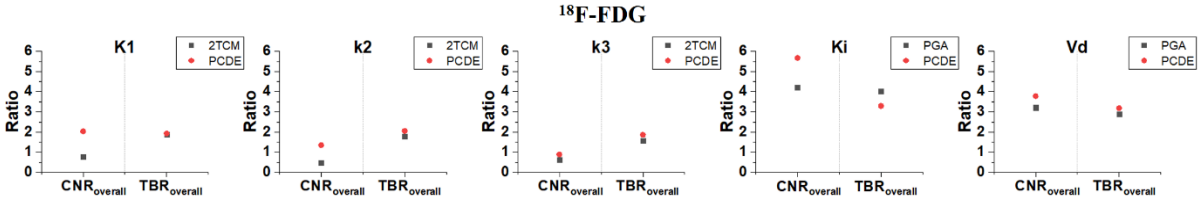

Figure 4- 17. Tumor detectability in each parametric image. Micro-parameters: first three columns; Macro-parameters: last two columns. Matrices: $CNR_{overall}$ and $TBR_{overall}$ (the # of lesions: 5). Radiotracer: ^{18}F-FDG.

In addition, the first two figures in Figure 4-16 present examples of parametric K_1 images via ^{18}F-FDG. Compared to reference method (i.e., 2TCM), the enhanced lesion detectability was verified via PCDE.

4.3.2.2. Kinetic Macro-parameters

The last two columns of Figure 4-13 show the tumor detectability results of ^{18}F-DCFPyL in the parametric K_i and V_d images. The overall CNR increased by 0.21 and -0.06, and the overall TBR increased by -0.49 and 0.16 for the parametric K_i and V_d images, respectively. The minus sign represents the decrease in metric of interest.

In addition, the last two columns of Figure 4-15 show the tumor detectability results of ^{68}Ga-HTK in the parametric K_i and V_d images. The overall CNR increased by 0.58 and 0.09, and the overall TBR increased by 0.03 and 0.13 for the parametric K_i and V_d images, respectively.

Furthermore, the last two columns of Figure 4-17 show the tumor detectability results of ^{18}F-FDG in the parametric K_i and V_d images. The overall CNR increased by 1.48 and 0.56, and the overall TBR increased by -0.73 and 0.28 for the parametric K_i and V_d images, respectively.

Overall, there were no substantial differences between the two methods in either type of parametric image. The differences in overall CNR were within 0.60, and the differences in overall TBR were 0.50 except for the ^{18}F-FDG cases (i.e., increase in $CNR_{overall}$ for K_i: 1.48, decrease in $TBR_{overall}$ for K_i: 0.73).

4.4. Discussion

As a pilot study, the comparison study was performed on real patient datasets (i.e., 8 patients in total), including analysis of: 1) overall visibility relevant to global inspection in WB, and 2) overall lesion detectability relevant to local inspection within a specific organ.

First, we verified that PCDE could improve the overall visibility (i.e., overall SNR) of micro-parametric images (i.e., each first three columns of Figures 4-1, 4-4, 4-7, and 4-10), which is relevant to the capability to identify suspicious lesions in WB globally.

For macro-parameters, there was no significant difference between the PCDE and LSE-based PGA (i.e., each last two columns of Figures 4-1, 4-4, 4-7, and 4-10), except for ^{18}F-FDG cases. Although the application of PCDE on patient datasets injected with ^{18}F-FDG seemingly shows substantial benefits in overall SNR even for macro-parameters (i.e., K_i: 3.14, V_d: 1.49) compared to the PGA method, it might be a coincidence and originate from the uncertainty of a point used for the scaling to generate a population-based input function. Normally, for accurate scaling, the scaling point should be a measured data through invasive blood sampling, which is considered as gold standard for the measurement of plasma input function and thus expected to provide more trustworthy data point compared to that derived from image. In this pilot study with ^{18}F-FDG, however, due to the absence of the data from blood sampling, the measured data used for the scaling was extracted from available PET image at earliest measurement time (i.e., ROI: left ventricle, post-injection time: ~30 min). Certainly, compared to the case using the invasive blood sampling for the scaling, the relatively larger uncertainty of the data measured from the image would lead to larger uncertainty of population-based input function, and thus might cause erroneously better results in parametric images.

In addition, with PCDE, we verified the improved lesion detectability (i.e., overall CNR and TBR) of micro-parameters, which would directly help to inspect a lesion locally in a particular organ. For macro-parameters, there were no significant differences in lesion detectability between the two methods (i.e., $CNR_{overall}$: within 0.60, $TBR_{overall}$: 0.50). This can be expectable by understanding the fact that the PGA is already sufficiently accurate for macro-parameter estimation because of exploitation of linearized fit-type function and thus it is hard to expect a substantial benefit from PCDE.

Overall, our proposed PCDE method provides enhanced micro-parametric images in terms of overall visibility (i.e., Figures 4-1, 4-4, 4-7, and 4-10) and lesion detectability (i.e., Figures 4-13, 4-15, and 4-17).

The proposed method PCDE is worthy to note in that it shows enhanced micro-parametric images when applying into not only virtual dynamic datasets (i.e., chap. 3) but also actual patient datasets (i.e., chap. 4), which implies a great potential to be implemented into routine practice in clinic.

Nevertheless, a few limitations of the study indicate the need for further studies: 1) lack of high number of patients analyzed in total, 2) differences in scanning protocols, and 3) need for future selection of the best compartmental model for each different radiotracer.

Overall, in this study, eight patients in total were analyzed to quantify overall visibility and among them only three patients were analyzed for lesion detectability. For each radiotracer, overall visibility and lesion detectability were evaluated by only two and one patient, respectively, except for ^{68}Ga-HTK case. Even though in this pilot study the PCDE shows improved overall SNR, CNR, and TBR simultaneously in micro-parametric images, it is pretty hasty to make a generalized conclusion due to the lack of the number of patients analyzed. Therefore, further validation study based on a greater number of patients should be conducted further to clearly judge the actual benefit of the proposed method.

Our institute is actively collecting more patient datasets through a clinical trial (i.e., Clinical Trial ID: NCT04017104): these include studies of ^{18}F-FDG (glucose metabolism), ^{18}F-DCFPyL and ^{68}Ga-HTK (prostate-specific membrane antigen (PSMA) targeted imaging), and ^{18}F-AmBF3 (somatostatin receptor 2 (SSTR2) targeted imaging). Hence, we expect to perform comparison/validation studies based on larger number of patient datasets for each tracer type.

The scanning protocol is a critical consideration in the level of accuracy and precision of the estimated parameters. The scanning protocols of patients analyzed (e.g., total image acquisition time, injected activity, et al.) vary for different radiotracer type and are even different among patients for thea same tracer (i.e., Table 4-2, 3, 4, and 5). To minimize the effect of scanning protocol itself, similar scanning protocols among patients would be desirable and we expect to achieve it by continuous and tight-knit discussions with clinical staffs such as nuclear medicine physicians, medical physicists and technicians at BC cancer.

A pre-requisite of kinetic modeling is to find an optimal compartmental model (e.g., the # of compartments, whether irreversible or reversible process, definitions of compartments, transport

relationship between compartments, et al.) for each tracer that best fits the data collected. In addition to the understanding/consideration of bio-chemical aspects of uptake process, the model selection can be quantitatively conducted based on a criterion such as the Akaike information criterion (AIC) and Bayesian information criterion (BIC). In this study, however, the irreversible uptake based on two tissue compartments was assumed for all tracer types without the model selection process, which might have a negative impact on parameter estimation (e.g., misleading and/or inaccurate outcomes).

For instance, the levels of overall visibility via both methods (i.e., reference and PCDE) were relatively lower for ^{18}F-AmBF3 cases (i.e., Figure 4- 4, 14, and 15), compared to that of other tracers regardless of parameter estimation methods used, and also the improvements of overall SNR via PCDE in micro-parametric images (i.e., Figure 4-4) were not significant (i.e., averaged $SNR_{overall}$ increase: 0.40, 0.61, and 0.47 for the parametric K_1, k_2, and k_3 images, respectively). In addition to that, for patient #2, the severely poor level of visibility in V_d images via PGA (i.e., Figure 4-15) was verified, which is very unlikely to exist if the radiotracer was distributed through irreversible uptake process. The relatively lower level of benefits of using PCDE in micro-parametric images and improbably poor visibility in macro-parametric images via PGA might originate from the large disparity in actual uptake of ^{18}F-AmBF3 and the assumed uptake process (i.e., irreversible uptake). In that sense, the further study based on AIC and/or BIC to find an optimal compartmental model for each radiotracer including ^{18}F-AmBF3 should be conducted.

Our proposed method PCDE is not limited to irreversible uptake processes and can be extendable to any type of compartmental model. Hence, performance testing on other types of compartmental model and further refinement to the method are possible and needed to ensure improved compatibility with various types of radiotracers.

Chapter 5. Conclusions and Future Studies

5.1. Summary and Findings

We compared the performance of kinetic parameter estimation between the common standard (LSE) and proposed PCDE method, focusing on general image quality, overall visibility, and tumor detectability. Although there were no significant differences in macro-parameter estimation, significant improvements in the micro-parameters were verified. PCDE can enable a typical PET scanner in dynamic WB imaging mode to reliably estimate kinetic micro-parameters, which has been so far very challenging owing to significant uncertainties in estimates when using LSE.

5.2. Contribution to the Field

Our work contributes to PET scanner-based WB kinetic modeling in three aspects: 1) minimization of adverse effects of the WB scan protocol previously optimized for macro-parameter, 2) potential applicability for shorter scan durations, and 3) avoidance of local minimum issues.

First of all, the protocol proposed by Karakatsanis et al. was optimized based on macro-parametric images (i.e., K_i) and was spent 6 min after injection to scan the cardiac region. Because the macro-parameters of PGA only require data after the kinetic process of interest reaches equilibrium state, the loss of early dynamics of TAC would not adversely affect parameter estimation. However, unlike macro-parameters, early dynamics are critical for micro-parameter estimation because they typically include near-peak data considerably influenced by micro-parameter combinations. PCDE showed improvements for each micro-parameter compared to the common standard. This indicates a substantial reduction in the adverse effects of the protocol favorably optimized for macro-parameter estimation.

Moreover, for the second point, the comprehensive comparison based on the multi-aspect of TAC can offer more stabilized parameter estimation (i.e., less variation of performance) from various image acquisition-related factors compared to the case considering only one single factor (e.g.,

SSE for LSE). Therefore, we expect our proposed method to perform better even when using a dynamic PET dataset scanned only for 30 min, realistically achieving the shortest scan duration for a typical PET scanner-based WB kinetic modeling for micro-parameter estimation.

All results reported in this study are based on a simulated dynamic dataset scanned only 40 min PI, which is 5 min shorter than the optimal acquisition length suggested by Karakatsanis et al. (i.e., 45 min) and 20 min shorter than the time typically required for dynamic PET acquisition for kinetic modeling (i.e., 60 min). Hence, we can expect the promising applicability of the proposed method to studies involving shorter scan duration.

Moreover, the PCDE avoids the local minimum issue by systematically evaluating various aspects of TAC and selecting the best parameter combination, rather than relying on an iterative approach to find an optimal value. Consequently, unlike the LSE method, the PCDE does not necessitate an initial guess for parameter estimation. However, PCDE also uses curve fitting to model a measured TAC, but the later dynamics of TAC can be well-fitted using a single exponential function which can be an automatic process without a manual initial guess because of its negligible dependence on the initial values.

5.3. Suggestions for Future Work

A couple of limitations in our proposed method indicate the need for further studies as follows: 1) reduction in computational time using parallel processing, 2) extension of compatibility with diverse types of radiopharmaceuticals, 3) further improvements in image quality, and 4) validation study based on larger pool of patient dataset.

First, the computational speed of PCDE is approximately 1.1×10^{-3} s/voxel; therefore, approximately 2 h are needed to perform WB kinetic modeling for a typical volume size in the clinic (i.e., $256 \times 256 \times 409$) with plain hardware specifications (e.g., CPU: AMD Ryzen 9 5900HX, RAM: 32.0 GB, platform: MATLAB R2021b, resolution of estimated parameter: 0.01). For use in routine practice, at least 100 times the current computational speed (i.e., ~10^{-5} s/voxel)

is needed to complete the computation in a few minutes. Parallelized computation using a graphical processing unit (GPU) will allow us to achieve this.

Second, in this study, we limited the maximum allowable value of the micro-parameter to 1 (for K_1 and k_2) and 0.5 (for k_3), respectively. Although for ^{18}F-FDG, almost all micro-parameters for each ROI in WB were within the desired ranges, we need to broaden the range to increase applicability to diverse types of radiotracers. Also, depending on a specific radiotracer of interest or research focus, the reversible uptake (i.e., $k_4 \neq 0$) may be of greater interest, than the irreversible process; hence, a performance test under the reversible process would be needed.

Furthermore, despite significant improvements via PCDE, the overall levels of NBias and NSD tend to be beyond 10% (i.e., near 20%), and non-negligible variations among ROIs exist, implying that the proposed method may still be insufficient for use in routine practice. We expect that the exploitation of de-noising techniques such as the finite Legendre transform-based low-pass filter with excellent de-noising performance for the exponential type curve (i.e., typical shape of TAC after peak) without the phase shift and/or noise propagation pattern learning through machine/deep learning algorithms (i.e., noise propagation from the sinogram domain into image domain) could reduce the overall levels of NBias and NSD within 10%. Moreover, it can reduce variations among ROIs (i.e., consideration of different noise propagation patterns at each position).

Finally, a validation study based on larger pool of patient dataset should be conducted. We are actively collecting patient data (e.g., Clinical Trial ID: NCT04017104) categorized by a specific tumor detection mechanism such as ^{18}F-FDG by glucose metabolism, ^{18}F-DCFPyL and ^{68}Ga-HTK by targeting a PSMA, and ^{18}F-AmBF3 by targeting SSTR2. We expect to perform a validation study based on larger pool of patient data in the near future.

Bibliography

1. Cherry SR, Sorenson JA, Phelps ME. *Physics in Nuclear Medicine*. 4th ed. Elsevier/Saunders; 2012.

2. Chandra R, Rahmim A. *Nuclear Medicine Physics: The Basics*. Eighth edition. Wolters Kluwer; 2018.

3. Zaidi H, ed. *Quantum Analysis in Nuclear Medicine Imaging*. Springer; 2005.

4. Rahmim A, Zaidi H. PET versus SPECT: strengths, limitations and challenges. *Nuclear Medicine Communications*. 2008;29(3):193-207. doi:10.1097/MNM.0b013e3282f3a515

5. Blankenberg FG, Strauss HW. Nuclear medicine applications in molecular imaging. *J Magn Reson Imaging*. 2002;16(4):352-361. doi:10.1002/jmri.10171

6. Rosenthal MS, Cullom J, Hawkins W, Moore SC, Tsui BMW, Yester M. Quantitative SPECT Imaging: A Review and Recommendations by the Focus Committee of the Society of Nuclear Medicine Computer and Instrumentation Council.

7. Holly TA, Abbott BG, Al-Mallah M, et al. Single photon-emission computed tomography. *J Nucl Cardiol*. 2010;17(5):941-973. doi:10.1007/s12350-010-9246-y

8. Jaszczak RJ, Coleman RE, Lim CB. SPECT: SINGLE PHOTON EMISSION COMPUTED TOMOGRAPHY.

9. Knoll GF. Single-photon emission computed tomography. *Proc IEEE*. 1983;71(3):320-329. doi:10.1109/PROC.1983.12590

10. Holman BL. Single-Photon Emission Computed Tomography (SPECT): Applications and Potential. *JAMA*. 1990;263(4):561. doi:10.1001/jama.1990.03440040100036

11. Groch MW, Erwin WD. Single-Photon Emission Computed Tomography in the Year 2001: Instrumentation and Quality Control. *JOURNAL OF NUCLEAR MEDICINE TECHNOLOGY*. 2001;29(1).

12. Schoder H, Erdi YE, Larson SM, Yeung HWD. PET/CT: a new imaging technology in nuclear medicine. *European Journal of Nuclear Medicine and Molecular Imaging*. 2003;30(10):1419-1437. doi:10.1007/s00259-003-1299-6

13. Gallamini A, Zwarthoed C, Borra A. Positron Emission Tomography (PET) in Oncology. *Cancers*. 2014;6(4):1821-1889. doi:10.3390/cancers6041821

14. Kubota K. From tumor biology to clinical PET: A review of positron emission tomography (PET) in oncology. *Ann Nucl Med*. 2001;15(6):471-486. doi:10.1007/BF02988499

15. Hillner BE, Siegel BA, Liu D, et al. Impact of Positron Emission Tomography/Computed Tomography and Positron Emission Tomography (PET) Alone on Expected Management of Patients With Cancer: Initial Results From the National Oncologic PET Registry. *JCO*. 2008;26(13):2155-2161. doi:10.1200/JCO.2007.14.5631

16. Townsend DW. Positron Emission Tomography/Computed Tomography. *Seminars in Nuclear Medicine*. 2008;38(3):152-166. doi:10.1053/j.semnuclmed.2008.01.003

17. Young I. Nuclear magnetic resonance imaging. Published online 1984.

18. van Geuns RJM, Wielopolski PA, de Bruin HG, Rensing BJ, Oudkerk M, de Feyter PJ. Basic Principles of Magnetic Resonance Imaging.

19. Bley TA, Wieben O, François CJ, Brittain JH, Reeder SB. Fat and water magnetic resonance imaging: Fat and Water MRI. *J Magn Reson Imaging*. 2010;31(1):4-18. doi:10.1002/jmri.21895

20. Reeder SB, Sirlin CB. Quantification of Liver Fat with Magnetic Resonance Imaging. *Magnetic Resonance Imaging Clinics of North America*. 2010;18(3):337-357. doi:10.1016/j.mric.2010.08.013

21. Dirix P, Haustermans K, Vandecaveye V. The Value of Magnetic Resonance Imaging for Radiotherapy Planning. *Seminars in Radiation Oncology*. 2014;24(3):151-159. doi:10.1016/j.semradonc.2014.02.003

22. Hathcock JT, Stickle RL. Principles and Concepts of Computed Tomography. *Veterinary Clinics of North America: Small Animal Practice*. 1993;23(2):399-415. doi:10.1016/S0195-5616(93)50034-7

23. Kalender WA. X-ray computed tomography. *Phys Med Biol*. 2006;51(13):R29-R43. doi:10.1088/0031-9155/51/13/R03

24. Battista JJ, Rider WD, Van Dyk J. Computed tomography for radiotherapy planning. *International Journal of Radiation Oncology*Biology*Physics*. 1980;6(1):99-107. doi:10.1016/0360-3016(80)90211-4

25. Forrest LJ. Computed Tomography Imaging in Oncology. *Veterinary Clinics of North America: Small Animal Practice*. 2016;46(3):499-513. doi:10.1016/j.cvsm.2015.12.007

26. Carter LM, Kesner AL, Pratt EC, et al. The Impact of Positron Range on PET Resolution, Evaluated with Phantoms and PHITS Monte Carlo Simulations for Conventional and Non-conventional Radionuclides. *Mol Imaging Biol*. 2020;22(1):73-84. doi:10.1007/s11307-019-01337-2

27. Schmitz RE, Alessio AM, Kinahan PE. The Physics of PET/CT scanners.

28. Klyuzhin IS. Deformable Motion Correction and Spatial Image Analysis in Positron Emission Tomography.

29. Doroudi S. The Bias-Variance Tradeoff: How Data Science Can Inform Educational Debates.

30. Jian Y, Planeta B, Carson RE. Evaluation of bias and variance in low-count OSEM list mode reconstruction. *Phys Med Biol*. 2015;60(1):15-29. doi:10.1088/0031-9155/60/1/15

31. Shepp LA, Vardi Y. Maximum Likelihood Reconstruction for Emission Tomography. *IEEE Trans Med Imaging*. 1982;1(2):113-122. doi:10.1109/TMI.1982.4307558

32. Lange K, Carson R. EM Reconstruction Algorithms for Emission and Transmission Tomography.

33. Kaufman L. Maximum likelihood, least squares, and penalized least squares for PET. *IEEE Trans Med Imaging*. 1993;12(2):200-214. doi:10.1109/42.232249

34. Nuyts J, Fessler JA. A penalized-likelihood image reconstruction method for emission tomography, compared to postsmoothed maximum-likelihood with matched spatial resolution. *IEEE Trans Med Imaging*. 2003;22(9):1042-1052. doi:10.1109/TMI.2003.816960

35. Hudson HM, Larkin RS. Accelerated image reconstruction using ordered subsets of projection data. *IEEE Trans Med Imaging*. 1994;13(4):601-609. doi:10.1109/42.363108

36. Hsiao IT, Rangarajan A, Khurd P, Gindi G. An accelerated convergent ordered subsets algorithm for emission tomography. *Phys Med Biol*. 2004;49(11):2145-2156. doi:10.1088/0031-9155/49/11/002

37. Comtat, Bataille F, Michel C, et al. OSEM-3D Reconstruction Strategies for the ECAT HRRT. In: *IEEE Symposium Conference Record Nuclear Science 2004.* Vol 6. IEEE; 2004:3492-3496. doi:10.1109/NSSMIC.2004.1466639

38. Bentourkia M, Zaidi H. Tracer Kinetic Modeling in PET. *PET Clinics*. 2007;2(2):267-277. doi:10.1016/j.cpet.2007.08.003

39. Gunn RN, Gunn SR, Turkheimer FE, Aston JAD, Cunningham VJ. Positron Emission Tomography Compartmental Models: A Basis Pursuit Strategy for Kinetic Modeling. *J Cereb Blood Flow Metab*. 2002;22(12):1425-1439. doi:10.1097/01.wcb.0000045042.03034.42

40. Li F, Joergensen JT, Hansen AE, Kjaer A. Kinetic modeling in PET imaging of hypoxia.

41. Ichise M, Meyer JH, Yonekura Y. An Introduction to PET and SPECT Neuroreceptor Quantification Models.

42. Acton PD, Zhuang H, Alavi A. Quantification in PET. *Radiologic Clinics of North America*. 2004;42(6):1055-1062. doi:10.1016/j.rcl.2004.08.010

43. Morris ED, Endres CJ, Schmidt KC, Christian BT, Jr RFM, Fisher RE. Kinetic Modeling in Positron Emission Tomography.

44. Carson RE. 6 Tracer Kinetic Modeling in PET. *Positron Emission Tomography*.

45. Hamberg LM, Hunter GJ, Alpert M, Choi NC, Babich JW, Fischman AJ. The Dose Uptake Ratio as an Index of Glucose Metabolism: Useful Parameter or Oversimplffication?

46. Keyes JW. SUV: Standard Uptake or Silly Useless Value?

47. Huang (Henry) Sung-Cheng. Anatomy of SUV. *Nuclear Medicine and Biology*. 2000;27(7):643-646. doi:10.1016/S0969-8051(00)00155-4

48. Lodge MA, Lucas JD, Marsden PK, Cronin BF, O'Doherty MJ, Smith MA. A PET study of 18 FDG uptake in soft tissue masses. *European Journal of Nuclear Medicine and Molecular Imaging*. 1999;26(1):22-30. doi:10.1007/s002590050355

49. Sugawara Y, Zasadny KR, Grossman HB, Francis IR, Clarke MF, Wahl RL. Germ Cell Tumor: Differentiation of Viable Tumor, Mature Teratoma, and Necrotic Tissue with FDG PET and Kinetic Modeling. *Radiology*. 1999;211(1):249-256. doi:10.1148/radiology.211.1.r99ap16249

50. Pantel AR, Viswanath V, Muzi M, Doot RK, Mankoff DA. Principles of Tracer Kinetic Analysis in Oncology, Part I: Principles and Overview of Methodology. *J Nucl Med*. 2022;63(3):342-352. doi:10.2967/jnumed.121.263518

51. Pantel AR, Viswanath V, Muzi M, Doot RK, Mankoff DA. Principles of Tracer Kinetic Analysis in Oncology, Part II: Examples and Future Directions. *J Nucl Med*. 2022;63(4):514-521. doi:10.2967/jnumed.121.263519

52. Lubberink M, Heurling K. Kinetic Modeling of Radiotracers. In: Lewis JS, Windhorst AD, Zeglis BM, eds. *Radiopharmaceutical Chemistry*. Springer International Publishing; 2019:501-514. doi:10.1007/978-3-319-98947-1_28

53. Stokke C, Gabiña PM, Solný P, et al. Dosimetry-based treatment planning for molecular radiotherapy: a summary of the 2017 report from the Internal Dosimetry Task Force. *EJNMMI Phys*. 2017;4(1):27. doi:10.1186/s40658-017-0194-3

54. Delforge J, Bottlaender M, Pappata S, Loc'h C, Syrota A. Absolute Quantification by Positron Emission Tomography of the Endogenous Ligand. *J Cereb Blood Flow Metab*. 2001;21(5):613-630. doi:10.1097/00004647-200105000-00016

55. Delforge J, Bendriem B. Concept of Reaction Volume in the In Vivo Ligand-Receptor Model.

56. Delforge J, Syrota A, Mazoyer BM. Experimental design optimisation: theory and application to estimation of receptor model parameters using dynamic positron emission tomography. *Phys Med Biol*. 1989;34(4):419-435. doi:10.1088/0031-9155/34/4/002

57. Delforge J, Syrota A, Mazoyer BM. Identifiability analysis and parameter identification of an in vivo ligand-receptor model from PET data. *IEEE Trans Biomed Eng*. 1990;37(7):653-661. doi:10.1109/10.55673

58. Laruelle M, Abi-Dargham A, Van Dyck CH, et al. Single photon emission computerized tomography imaging of amphetamine-induced dopamine release in drug-free schizophrenic subjects. *Proc Natl Acad Sci USA*. 1996;93(17):9235-9240. doi:10.1073/pnas.93.17.9235

59. Breier A, Su TP, Saunders R, et al. Schizophrenia is associated with elevated amphetamine-induced synaptic dopamine concentrations: Evidence from a novel positron emission tomography method. *Proc Natl Acad Sci USA*. 1997;94(6):2569-2574. doi:10.1073/pnas.94.6.2569

60. Sommariva S, Caviglia G, Sambuceti G, Piana M. Mathematical Models for FDG Kinetics in Cancer: A Review. *Metabolites*. 2021;11(8):519. doi:10.3390/metabo11080519

61. Patlak CS, Blasberg RG. Graphical Evaluation of Blood-to-Brain Transfer Constants from Multiple-Time Uptake Data. Generalizations. *J Cereb Blood Flow Metab*. 1985;5(4):584-590. doi:10.1038/jcbfm.1985.87

62. Dimitrakopoulou-Strauss A, Pan L, Sachpekidis C. Kinetic modeling and parametric imaging with dynamic PET for oncological applications: general considerations, current clinical applications, and future perspectives. *Eur J Nucl Med Mol Imaging*. 2021;48(1):21-39. doi:10.1007/s00259-020-04843-6

63. Rahmim A, Lodge MA, Karakatsanis NA, et al. Dynamic whole-body PET imaging: principles, potentials and applications. *Eur J Nucl Med Mol Imaging*. 2019;46(2):501-518. doi:10.1007/s00259-018-4153-6

64. Dahibom M, Hoffman E, Hoh CK, et al. Whole-Body Positron Emission Tomography: Part I. Methods and Performance Characteristics.

65. Hustinx R, Bénard F, Alavi A. Whole-body FDG-PET imaging in the management of patients with cancer. *Seminars in Nuclear Medicine*. 2002;32(1):35-46. doi:10.1053/snuc.2002.29272

66. Kubota K, Itoh M, Ozaki K, et al. Advantage of delayed whole-body FDG-PET imaging for tumour detection. *Eur J Nucl Med*. 2001;28(6):696-703. doi:10.1007/s002590100537

67. Boellaard R, O'Doherty MJ, Weber WA, et al. FDG PET and PET/CT: EANM procedure guidelines for tumour PET imaging: version 1.0. *Eur J Nucl Med Mol Imaging*. 2010;37(1):181-200. doi:10.1007/s00259-009-1297-4

68. Karakatsanis NA, Lodge MA, Tahari AK, Zhou Y, Wahl RL, Rahmim A. Dynamic whole-body PET parametric imaging: I. Concept, acquisition protocol optimization and clinical application. *Phys Med Biol*. 2013;58(20):7391-7418. doi:10.1088/0031-9155/58/20/7391

69. Karakatsanis NA, Lodge MA, Zhou Y, Wahl RL, Rahmim A. Dynamic whole-body PET parametric imaging: II. Task-oriented statistical estimation. *Phys Med Biol*. 2013;58(20):7419-7445. doi:10.1088/0031-9155/58/20/7419

70. Segars WP, Sturgeon G, Mendonca S, Grimes J, Tsui BMW. 4D XCAT phantom for multimodality imaging research: 4D XCAT phantom for multimodality imaging research. *Med Phys*. 2010;37(9):4902-4915. doi:10.1118/1.3480985

71. Liu G, Xu H, Hu P, et al. Kinetic metrics of 18F-FDG in normal human organs identified by systematic dynamic total-body positron emission tomography. *Eur J Nucl Med Mol Imaging*. 2021;48(8):2363-2372. doi:10.1007/s00259-020-05124-y

72. Feng D, Huang SC, Wang X. Models for computer simulation studies of input functions for tracer kinetic modeling with positron emission tomography. *International Journal of Bio-Medical Computing*. 1993;32(2):95-110. doi:10.1016/0020-7101(93)90049-C

73. Häggström I, Beattie BJ, Schmidtlein CR. Dynamic PET simulator via tomographic emission projection for kinetic modeling and parametric image studies: Dynamic PET simulator for kinetic modeling studies. *Med Phys*. 2016;43(6Part1):3104-3116. doi:10.1118/1.4950883

74. Berthon B, Häggström I, Apte A, et al. PETSTEP: Generation of synthetic PET lesions for fast evaluation of segmentation methods. *Physica Medica*. 2015;31(8):969-980. doi:10.1016/j.ejmp.2015.07.139

75. Johnson ML, Faunt LM. [1] Parameter estimation by least-squares methods. In: *Methods in Enzymology*. Vol 210. Elsevier; 1992:1-37. doi:10.1016/0076-6879(92)10003-V

76. Johnson ML, Frasier SG. [16] Nonlinear least-squares analysis. In: *Methods in Enzymology*. Vol 117. Elsevier; 1985:301-342. doi:10.1016/S0076-6879(85)17018-7

77. Johnson ML. Why, when, and how biochemists should use least squares. *Analytical Biochemistry*. 1992;206(2):215-225. doi:10.1016/0003-2697(92)90356-C

78. Overall JE, Spiegel DK. Concerning least squares analysis of experimental data. *Psychological Bulletin*. 1969;72(5):311-322. doi:10.1037/h0028109

79. Chen S, Billings SA, Luo W. Orthogonal least squares methods and their application to non-linear system identification. *International Journal of Control*. 1989;50(5):1873-1896. doi:10.1080/00207178908953472

80. Constable CG. Parameter estimation in non-Gaussian noise. *Geophys J Int*. 1988;94(1):131-142. doi:10.1111/j.1365-246X.1988.tb03433.x

81. Krikheli M, Leshem A. Finite sample performance of linear least squares estimation. Published online October 12, 2018. Accessed July 18, 2023. http://arxiv.org/abs/1810.06380

82. Kueng R, Driscoll B, Manser P, Fix MK, Stampanoni M, Keller H. Quantification of local image noise variation in PET images for standardization of noise-dependent analysis metrics. *Biomed Phys Eng Express*. 2017;3(2):025007. doi:10.1088/2057-1976/3/2/025007

83. Kraskov A, Stögbauer H, Grassberger P. Estimating mutual information. *Phys Rev E*. 2004;69(6):066138. doi:10.1103/PhysRevE.69.066138

84. Bennasar M, Hicks Y, Setchi R. Feature selection using Joint Mutual Information Maximisation. *Expert Systems with Applications*. 2015;42(22):8520-8532. doi:10.1016/j.eswa.2015.07.007

85. Ashraf C, Pfaendtner J. Assessing the Performance of Various Stochastic Optimization Methods on Chemical Kinetic Modeling of Combustion. *Ind Eng Chem Res*. 2020;59(43):19212-19225. doi:10.1021/acs.iecr.0c04009

86. Sámano V, Tirado A, Félix G, Ancheyta J. Revisiting the importance of appropriate parameter estimation based on sensitivity analysis for developing kinetic models. *Fuel*. 2020;267:117113. doi:10.1016/j.fuel.2020.117113

87. Kadrmas DJ, Oktay MB. Generalized separable parameter space techniques for fitting 1K-5K serial compartment models: Separable parameter space compartment modeling. *Med Phys*. 2013;40(7):072502. doi:10.1118/1.4810937

88. Zhou Y, Ye W, Brašić JR, Wong DF. Multi-graphical analysis of dynamic PET. *NeuroImage*. 2010;49(4):2947-2957. doi:10.1016/j.neuroimage.2009.11.028

89. Logan J. A review of graphical methods for tracer studies and strategies to reduce bias. *Nuclear Medicine and Biology*. 2003;30(8):833-844. doi:10.1016/S0969-8051(03)00114-8

90. Bao G, Schild D. Fast and Accurate Fitting and Filtering of Noisy Exponentials in Legendre Space. Brody JP, ed. *PLoS ONE*. 2014;9(3):e90500. doi:10.1371/journal.pone.0090500

91. Fletcher JW, Djulbegovic B, Soares HP, et al. Recommendations on the Use of ^{18}F-FDG PET in Oncology. *J Nucl Med*. 2008;49(3):480-508. doi:10.2967/jnumed.107.047787

92. Rowe SP, Macura KJ, Mena E, et al. PSMA-Based [18F]DCFPyL PET/CT Is Superior to Conventional Imaging for Lesion Detection in Patients with Metastatic Prostate Cancer. *Mol Imaging Biol*. 2016;18(3):411-419. doi:10.1007/s11307-016-0957-6

93. Verena A, Zhang Z, Kuo HT, et al. Synthesis and Preclinical Evaluation of Three Novel 68Ga-Labeled Bispecific PSMA/FAP-Targeting Tracers for Prostate Cancer Imaging. *Molecules*. 2023;28(3):1088. doi:10.3390/molecules28031088

94. Lau J, Pan J, Rousseau E, et al. Pharmacokinetics, radiation dosimetry, acute toxicity and automated synthesis of [18F]AmBF3-TATE. *EJNMMI Res*. 2020;10(1):25. doi:10.1186/s13550-020-0611-9

Appendices

Appendix A: Solving Differential Equations for 2TCM and Derivation of PGA formulas.

Solving Differential Equations for 2TCM and Derivation of PGA formulas

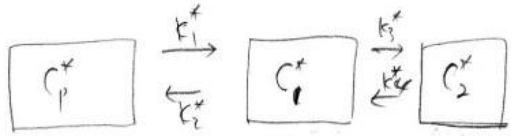

: three compartments model
: (= two tissue compartment model)

*: I will use this asterisk mark to differentiate the analogue's (e.g. radiotracer) parameters and concentrations from the original one's parameters and concentrations

If we define the radiotracer's influx & efflux rate & concentrations above, then we can get the formulas below, under the assumption that the change of concentration over time follows the first-order kinetics.

$$\Rightarrow \begin{cases} \dfrac{dC_1^*}{dt} = k_1^* C_p^* + k_4^* C_2^* - k_2^* C_1^* - k_3^* C_1^* = k_1^* C_p^* + k_4^* C_2^* - (k_2^* + k_3^*) C_1^* \\ \dfrac{dC_2^*}{dt} = k_3^* C_1^* - k_4^* C_2^* \end{cases}$$

⇒ We want to get C_1^* & C_2^*, so by using the characteristic of A Laplace transformation, we will get those things.

(Laplace transformation of a derivative)

$$\Rightarrow L[f'(t)] = s\underbrace{F(s)}_{L[f(t)]} - f(0)$$

$$\Rightarrow L[f''(t)] = s^2 F(s) - sf(0) - f'(0)$$

$$\Rightarrow L\left[\frac{dC_1^*}{dt}\right] = s \cdot \underbrace{L[C_1^*]}_{=\overline{C_1^*}} - \cancel{C_1^*(0)}^{\,0} = k_1^* L[C_p^*] + k_4^* L[C_2^*] - (k_2^* + k_3^*) L[C_1^*]$$

$$\Rightarrow s\overline{C_1^*} = k_1^* \overline{C_p^*} + k_4^* \overline{C_2^*} - (k_2^* + k_3^*)\overline{C_1^*} \quad \cdots (1)$$

$$\Rightarrow L\left[\frac{dC_2^*}{dt}\right] = s \cdot L[C_2^*] - \cancel{C_2^*(0)}^{\,0} = k_3^* L[C_1^*] - k_4^* \cdot L[C_2^*]$$

$$\Rightarrow s\overline{C_2^*} = k_3^* \overline{C_1^*} - k_4^* \overline{C_2^*} \quad \cdots (2)$$

If we use the relationship ① & ②, then

$$\Rightarrow \begin{cases} s\,\overline{c_1^*} = k_1^*\,\overline{c_p^*} + k_4^*\,\overline{c_2^*} - (k_2^* + k_3^*)\,\overline{c_1^*} & \cdots ① \\ s\,\overline{c_2^*} = k_3^*\,\overline{c_1^*} - k_4^*\,\overline{c_2^*} & \cdots ② \end{cases}$$

we can determine the relationship between $\overline{c_1^*}$ & $\overline{c_p^*}$ and $\overline{c_2^*}$ & $\overline{c_p^*}$

$$\Rightarrow (s + k_4^*)\,\overline{c_2^*} = k_3^*\,\overline{c_1^*} \Rightarrow \overline{c_2^*} = \frac{k_3^*}{s+k_4^*}\,\overline{c_1^*}$$

$$s\,\overline{c_1^*} = k_1^*\,\overline{c_p^*} + k_4^* \cdot \left[\frac{k_3^*}{s+k_4^*}\,\overline{c_1^*}\right] - (k_2^* + k_3^*)\,\overline{c_1^*}$$

$$= k_1^*\,\overline{c_p^*} + \left[\frac{k_3^* k_4^*}{s+k_4^*} - (k_2^* + k_3^*)\right] \cdot \overline{c_1^*}$$

$$= k_1^*\,\overline{c_p^*} + \left[\frac{k_3^* k_4^*}{s+k_4^*} - \frac{(s+k_4^*)(k_2^* + k_3^*)}{s+k_4^*}\right] \cdot \overline{c_1^*}$$

$$= k_1^*\,\overline{c_p^*} + \left[\frac{\cancel{k_3^* k_4^*} - (sk_2^* + sk_3^* + k_2^* k_4^* + \cancel{k_3^* k_4^*})}{s+k_4^*}\right] \cdot \overline{c_1^*}$$

$$= k_1^*\,\overline{c_p^*} - \left[\frac{(sk_2^* + sk_3^* + k_2^* k_4^*)}{s+k_4^*}\right] \cdot \overline{c_1^*}$$

$$\Rightarrow \left[s + \frac{sk_2^* + sk_3^* + k_2^* k_4^*}{s+k_4^*}\right] \cdot \overline{c_1^*} = k_1^*\,\overline{c_p^*}$$

$$\Rightarrow \overline{c_1^*} = \frac{k_1^*}{\left[s + \frac{sk_2^* + sk_3^* + k_2^* k_4^*}{s+k_4^*}\right]} \cdot \overline{c_p^*} = \frac{k_1^*(s+k_4^*)}{s(s+k_4^*) + sk_2^* + sk_3^* + k_2^* k_4^*} \cdot \overline{c_p^*}$$

$$= \left[\frac{k_1^*(s+k_4^*)}{s^2 + s(k_2^* + k_3^* + k_4^*) + k_2^* k_4^*}\right] \cdot \overline{c_p^*}$$

$$= \left[\frac{\Delta}{s+\alpha} + \frac{D}{s+\beta}\right] \cdot \overline{c_p^*} = \left[\frac{\Delta(s+\beta) + D(s+\alpha)}{s^2 + s(\alpha+\beta) + \alpha\beta}\right] \cdot \overline{c_p^*}$$

$$= \left[\frac{s(\Delta + D) + \Delta\beta + D\alpha}{s^2 + s(\alpha+\beta) + \alpha\beta}\right] \cdot \overline{c_p^*} \Rightarrow \begin{cases} \alpha + \beta = k_2^* + k_3^* + k_4^* \\ \alpha\beta = k_2^* k_4^* \\ \Delta + D = k_1^* \\ \Delta\beta + D\alpha = k_1^* k_4^* \end{cases}$$

2

$$\Rightarrow \begin{cases} \alpha+\beta = k_2^*+k_3^*+k_4^* \\ \alpha\beta = k_3^* k_4^* \end{cases}$$

$$\beta = \frac{k_2^* k_4^*}{\alpha} \Rightarrow \alpha + \frac{k_2^* k_4^*}{\alpha} = k_2^*+k_3^*+k_4^*$$

$$\Rightarrow \alpha^2 + k_2^* k_4^* = \alpha(k_2^*+k_3^*+k_4^*)$$

$$\Rightarrow \alpha^2 - \alpha(k_2^*+k_3^*+k_4^*) + k_2^* k_4^* = 0$$

$$\Rightarrow \alpha = \frac{(k_2^*+k_3^*+k_4^*) \pm \sqrt{(k_2^*+k_3^*+k_4^*)^2 - 4k_2^* k_4^*}}{2}$$

If we select α as $\alpha = \dfrac{(k_2^*+k_3^*+k_4^*) + \sqrt{(k_2^*+k_3^*+k_4^*)^2 - 4k_2^* k_4^*}}{2}$, then.

$$\beta = (k_2^*+k_3^*+k_4^*) - \alpha$$

$$= (k_2^*+k_3^*+k_4^*) - \left[\frac{(k_2^*+k_3^*+k_4^*) + \sqrt{(k_2^*+k_3^*+k_4^*)^2 - 4k_2^* k_4^*}}{2}\right]$$

$$= \frac{(k_2^*+k_3^*+k_4^*) - \sqrt{(k_2^*+k_3^*+k_4^*)^2 - 4k_2^* k_4^*}}{2}$$

$$\therefore \begin{cases} \alpha = \dfrac{\overbrace{(k_2^*+k_3^*+k_4^*)}^{C} + \sqrt{(k_2^*+k_3^*+k_4^*)^2 - 4k_2^* k_4^*}}{2} \\ \beta = \dfrac{(k_2^*+k_3^*+k_4^*) - \sqrt{(k_2^*+k_3^*+k_4^*)^2 - 4k_2^* k_4^*}}{2} \end{cases} \Rightarrow C \equiv k_2^*+k_3^*+k_4^*$$

$$\Rightarrow \begin{cases} \cdot\ \Delta + D = k_1^* \\ \cdot\ \Delta\beta + D\alpha = k_1^* k_4^* \end{cases}$$

$$\Rightarrow \begin{cases} \Delta + D = k_1^* \\ \Delta \cdot \left(\dfrac{C - \sqrt{C^2 - 4k_2^* k_4^*}}{2}\right) + D \cdot \left(\dfrac{C + \sqrt{C^2 - 4k_2^* k_4^*}}{2}\right) = k_1^* k_4^* \end{cases}$$

3

$$\Rightarrow \Delta\left(\frac{C-\sqrt{C^2-4k_2^*k_4^*}}{2}\right)+D\left(\frac{C+\sqrt{C^2-4k_2^*k_4^*}}{2}\right)=k_1^*k_4^*$$

$$\Rightarrow \frac{C}{2}(\Delta+D)-\frac{\Delta}{2}\sqrt{C^2-4k_2^*k_4^*}+\frac{D}{2}\sqrt{C^2-4k_2^*k_4^*}=k_1^*k_4^* \quad \& \; D=k_1^*-\Delta$$

$$\therefore \frac{C}{2}(k_1^*)-\frac{\Delta}{2}\sqrt{C^2-4k_2^*k_4^*}+\left(\frac{k_1^*-\Delta}{2}\right)\sqrt{C^2-4k_2^*k_4^*}=k_1^*k_4^*$$

If we define $\sqrt{C^2-4k_2^*k_4^*}$ as t, then

$$\Rightarrow \frac{C}{2}k_1^*-\frac{\Delta}{2}t+\left(\frac{k_1^*-\Delta}{2}\right)t=k_1^*k_4^*$$

$$\Rightarrow \frac{C}{2}k_1^*+\frac{k_1^*}{2}t-\Delta t=k_1^*k_4^*$$

$$\Rightarrow \Delta t=\frac{C}{2}k_1^*+\frac{k_1^*}{2}t-k_1^*k_4^*=k_1^*\left(\frac{C}{2}+\frac{t}{2}-k_4^*\right)$$

$$\Rightarrow \therefore \Delta=\frac{k_1^*}{t}\left(\frac{C}{2}+\frac{t}{2}-k_4^*\right), \text{ where } \left(\begin{array}{l} C\equiv k_2^*+k_3^*+k_4^* \\ t=\sqrt{C^2-4k_2^*k_4^*}\end{array}\right)$$

$$=\frac{k_1^*}{\underbrace{\sqrt{(k_2^*+k_3^*+k_4^*)^2-4k_2^*k_4^*}}_{=\alpha-\beta}}\left[\underbrace{\frac{(k_2^*+k_3^*+k_4^*)}{2}+\frac{\sqrt{(k_2^*+k_3^*+k_4^*)^2-4k_2^*k_4^*}}{2}}_{=\alpha}-k_4^*\right]$$

$$\therefore \begin{cases} \Delta=\dfrac{k_1^*}{\alpha-\beta}\left[\alpha-k_4^*\right] \\ D=k_1^*-\Delta=k_1^*-\dfrac{k_1^*}{\alpha-\beta}\left[\alpha-k_4^*\right]=k_1^*\left[1-\dfrac{(\alpha-k_4^*)}{\alpha-\beta}\right]=k_1^*\left[\dfrac{\alpha-\beta-\alpha+k_4^*}{\alpha-\beta}\right] \\ \quad =k_1^*\left(\dfrac{k_4^*-\beta}{\alpha-\beta}\right) \end{cases}$$

Now, finally, we can get formulas which is proper to proceed inverse Laplace transformation ⊕

4

$$\Rightarrow \begin{cases} \alpha = \dfrac{(k_2^*+k_3^*+k_4^*) + \sqrt{(k_2^*+k_3^*+k_4^*)^2 - 4k_2^* k_4^*}}{2}, \quad \beta = \dfrac{(k_2^*+k_3^*+k_4^*) - \sqrt{(k_2^*+k_3^*+k_4^*)^2 - 4k_2^* k_4^*}}{2} \\ \Delta = \dfrac{k_1^*}{\alpha-\beta}(\alpha - k_4^*), \quad D = k_1^*\left(\dfrac{k_4^* - \beta}{\alpha-\beta}\right) \end{cases}$$

$$\overline{C_1^*} = \left[\frac{\Delta}{s+\alpha} + \frac{D}{s+\beta}\right]\cdot \overline{C_p^*}$$

$$= \left[\frac{\frac{k_1^*}{\alpha-\beta}(\alpha-k_4^*)}{s+\alpha} + \frac{k_1^*\left(\frac{k_4^*-\beta}{\alpha-\beta}\right)}{s+\beta}\right]\cdot \overline{C_p^*}$$

$$= \left(\frac{k_1^*}{\alpha-\beta}\right)\left[\frac{\alpha-k_4^*}{s+\alpha} - \frac{\beta-k_4^*}{s+\beta}\right]\cdot \overline{C_p^*}$$

Then, now we can use the fact that

$$\because L^{-1}[F\cdot G] = f \otimes g \quad \left(\begin{array}{l}\text{where} \\ F = L[f] \\ G = L[g]\end{array}\right)$$

$$L^{-1}\left[\frac{1}{s+\alpha}\right] = e^{-\alpha t}\cdot \underline{u(t)}$$

unit step function

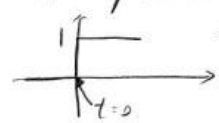

$$\Rightarrow \begin{cases} u(t) = 0, & t<0 \\ \quad = 1, & t\geq 0 \end{cases}$$

$$\Rightarrow L^{-1}[\overline{C_1^*}] = \frac{k_1^*}{\alpha-\beta} L^{-1}\left[\left[\left(\frac{\alpha-k_4^*}{s+\alpha}\right) - \left(\frac{\beta-k_4^*}{s+\beta}\right)\right]\cdot \overline{C_p^*}\right]$$

$$\Rightarrow C_1^* = \left(\frac{k_1^*}{\alpha-\beta}\right)\cdot L^{-1}\left[\left(\frac{\alpha-k_4^*}{s+\alpha}\right)\cdot \overline{C_p^*} - \left(\frac{\beta-k_4^*}{s+\beta}\right)\cdot \overline{C_p^*}\right]$$

$$= \left(\frac{k_1^*}{\alpha-\beta}\right)\cdot\left\{(\alpha-k_4^*)\cdot e^{-\alpha t}\otimes C_p^* - (\beta-k_4^*)e^{-\beta t}\otimes C_p^*\right\}$$

$$= \left(\frac{k_1^*}{\alpha-\beta}\right)\cdot\left\{\left[(\alpha-k_4^*)e^{-\alpha t} - (\beta-k_4^*)e^{-\beta t}\right]\otimes C_p^*\right\}$$

by using same way, we also can get C_2^*

5

We already know the relationship $\overline{C_2^*} = \frac{k_3^*}{s+k_4^*}\overline{C_1^*}$ & $\overline{C_1^*} = \left(\frac{k_1^*}{\alpha-\beta}\right)\left[\frac{\alpha-k_4^*}{s+\alpha} - \frac{\beta-k_4^*}{s+\beta}\right]\cdot\overline{C_p^*}$,

then,

$$\Rightarrow \overline{C_2^*} = \frac{k_3^*}{s+k_4^*}\cdot\left(\frac{k_1^*}{\alpha-\beta}\right)\left[\frac{\alpha-k_4^*}{s+\alpha} - \frac{\beta-k_4^*}{s+\beta}\right]\cdot\overline{C_p^*}$$

If we use inverse Laplace transformation, then

$$\Rightarrow L^{-1}\left[\overline{C_2^*}\right] = \left(\frac{k_1^* k_3^*}{\alpha-\beta}\right) L^{-1}\left[\left(\frac{1}{s+k_4^*}\right)\left(\frac{\alpha-k_4^*}{s+\alpha} - \frac{\beta-k_4^*}{s+\beta}\right)\cdot\overline{C_p^*}\right]$$

$$= \left(\frac{k_1^* k_3^*}{\alpha-\beta}\right)\cdot L^{-1}\left[\frac{(\alpha-k_4^*)}{(s+k_4^*)(s+\alpha)} - \frac{(\beta-k_4^*)}{(s+k_4^*)(s+\beta)}\right] \otimes L^{-1}\left[\overline{C_p^*}\right]$$

$$= \left(\frac{k_1^* k_3^*}{\alpha-\beta}\right)\cdot L^{-1}\left[\frac{(\alpha-k_4^*)}{(s+k_4^*)(s+\alpha)} - \frac{(\beta-k_4^*)}{(s+k_4^*)(s+\beta)}\right] \otimes C_p^*$$

If we use the fact $\Rightarrow L^{-1}\left[\frac{1}{(s+a)(s+b)}\right] = \frac{1}{a-b}\left(e^{-bt} - e^{-at}\right)$

$$= \left(\frac{k_1^* k_3^*}{\alpha-\beta}\right)\cdot\left\{(\alpha-k_4^*)\cdot\frac{1}{k_4^*-\alpha}\left(e^{-\alpha t} - e^{-k_4^* t}\right) - (\beta-k_4^*)\cdot\frac{1}{k_4^*-\beta}\left(e^{-\beta t} - e^{-k_4^* t}\right)\right\}\otimes C_p^*$$

$$= \left(\frac{k_1^* k_3^*}{\alpha-\beta}\right)\cdot\left\{-e^{-\alpha t} + \cancel{e^{-k_4^* t}} + e^{-\beta t} - \cancel{e^{-k_4^* t}}\right\}\otimes C_p^*$$

$$= \left(\frac{k_1^* k_3^*}{\alpha-\beta}\right)\cdot\left[e^{-\beta t} - e^{-\alpha t}\right]\otimes C_p^* = C_2^*$$

6

Now. We know C_1^* & C_2^* like below,

$$\begin{cases} C_1^*(t) = \left(\frac{k_1^*}{\alpha-\beta}\right)\left[(\alpha-k_4^*)e^{-\alpha t}-(\beta-k_4^*)e^{-\beta t}\right]\otimes C_p^* \\ C_2^*(t) = \left(\frac{k_1^* k_3^*}{\alpha-\beta}\right)\left[e^{-\beta t}-e^{-\alpha t}\right]\otimes C_p^* \\ \text{where, } \alpha = \frac{(k_2^*+k_3^*+k_4^*)+\sqrt{(k_2^*+k_3^*+k_4^*)^2-4k_3^*k_4^*}}{2}, \quad \beta = \frac{(k_2^*+k_3^*+k_4^*)-\sqrt{(k_2^*+k_3^*+k_4^*)^2-4k_3^*k_4^*}}{2} \end{cases}$$

If compartment #1 and compartment #2 are not physically differentiable states, then, the total concentration should be sum of them

$$\therefore C_{tot}^*(t) = C_1^*(t) + C_2^*(t)$$

$$= \left(\frac{k_1^*}{\alpha-\beta}\right)\left[(\alpha-k_4^*)e^{-\alpha t}-(\beta-k_4^*)e^{-\beta t}\right]\otimes C_p^* + \left(\frac{k_1^* k_3^*}{\alpha-\beta}\right)\left[e^{-\beta t}-e^{-\alpha t}\right]\otimes C_p^*$$

$$= \left(\frac{k_1^*}{\alpha-\beta}\right)\cdot\left[\alpha e^{-\alpha t}-k_4^* e^{-\alpha t}-\beta e^{-\beta t}+k_4^* e^{-\beta t}+k_3^* e^{-\beta t}-k_3^* e^{-\alpha t}\right]\otimes C_p^*$$

$$= \left(\frac{k_1^*}{\alpha-\beta}\right)\cdot\left[(\alpha-k_4^*-k_3^*)e^{-\alpha t}+(-\beta+k_4^*+k_3^*)e^{-\beta t}\right]\otimes C_p^*$$

$$= \left(\frac{k_1^*}{\alpha-\beta}\right)\left[(\alpha-k_3^*-k_4^*)e^{-\alpha t}-(\beta-k_3^*-k_4^*)e^{-\beta t}\right]\otimes C_p^*$$

total concentration of RO1 or VOI with the two tissue compartments model

But, we are interesting in the case with irreversible tissue at the end, $(k_4^*=0)$

So, let's dealing with the issue.

7

If $k_4^* \neq 0$

$$\Rightarrow C^*_{tot}(t) = \left(\frac{k_1^*}{\alpha-\beta}\right)\left[(\alpha - k_3^* - k_4^*)e^{-\alpha t} - (\beta + k_3^* - k_4^*)e^{-\beta t}\right] \otimes C_p^*$$

If $k_4^* = 0$ (case of our interest)

$$\Rightarrow \alpha = \frac{(k_2^*+k_3^*+k_4^*) + \sqrt{(k_2^*+k_3^*+k_4^*)^2 - 4k_2^*k_4^*}}{2} \Rightarrow \alpha_{k_4^*=0} = \frac{(k_2^*+k_3^*)+(k_2^*+k_3^*)}{2} = \underline{k_2^*+k_3^*}$$

$$\beta = \frac{(k_2^*+k_3^*+k_4^*) - \sqrt{(k_2^*+k_3^*+k_4^*)^2 - 4k_2^*k_4^*}}{2} \Rightarrow \beta_{k_4^*=0} = \frac{(k_2^*+k_3^*)-(k_2^*+k_3^*)}{2} = \underline{0}$$

$$\therefore C^*_{tot\_k_4^*=0}(t) = \left(\frac{k_1^*}{k_2^*+k_3^*}\right)\left[(k_2^*+\cancel{k_3^*}-\cancel{k_3^*})e^{-(k_2^*+k_3^*)t} + k_3^*\right] \otimes C_p^*$$

$$= \left(\frac{k_1^*}{k_2^*+k_3^*}\right)\left[k_2^* \cdot e^{-(k_2^*+k_3^*)t} + k_3^*\right] \otimes C_p^*$$

$$= \frac{k_1^* k_2^*}{k_2^*+k_3^*} e^{-(k_2^*+k_3^*)t} \otimes C_p^* + \frac{k_1^* k_3^*}{k_2^*+k_3^*} \otimes C_p^*$$

total concentration of ROI or voxel with the two tissue compartments model (with irreversible tissue compartment)

$\Rightarrow$ However, there is possibility that some blood part is included in our ROI or voxel. In this case, we also need to add the concentration due to blood part. If we express the situation mathematically,

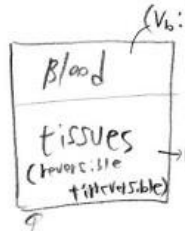

$$\Rightarrow C^*_{measured}(t) = (1-V_b)C^*_{tot\_k_4^*=0}(t) + V_b \cdot C_p^*$$

8

$$\Rightarrow C^{*}_{measured}(t) = (1-V_b)\, C^{*}_{tot\_k_4^*=0}(t) + V_b \cdot C_p^{*}(t)$$

$$= (1-V_b)\cdot\Big[\underbrace{\frac{k_1^* k_2^*}{k_2^*+k_3^*} e^{-(k_2^*+k_3^*)t} \otimes C_p^{*}}_{①} + \underbrace{\frac{k_1^* k_3^*}{k_2^*+k_3^*} \otimes C_p^{*}}_{②}\Big] + V_b \cdot C_p^{*}$$

total measured concentration of ROI or voxel with two tissue compartments model (with irreversible tissue) + (with partial volume of blood)

If time goes by enoughly, then all compartments could be in equlibrium. In eq. state of system, time t is generally very big relatively than rate constants (e.g. $k_1^*, k_2^*, k_3^*, k_4^*$), and plasma input function C_p^* could be dealt with as constant.

Then, formulas ① & ② could be approximated like below.

for ①

$$\Rightarrow e^{-(k_2^*+k_3^*)t} \otimes C_p^{*} = \int_0^t C_p^{*}(\tau)\cdot e^{-(k_2^*+k_3^*)(-\tau+t)}\, d\tau = \int_0^t C_p^{*}(\tau)\cdot e^{(k_2^*+k_3^*)\tau}\cdot e^{-(k_2^*+k_3^*)t}\, d\tau$$

$$= e^{-(k_2^*+k_3^*)t}\cdot\int_0^t C_p^{*}(\tau)\cdot e^{(k_2^*+k_3^*)\tau}\, d\tau$$

if we define the plasma input function at eq. state of syst. as C_p^{*eq} (varied very little, so we consider the function as constant.)

$$\approx C_p^{*eq}(t)\cdot e^{-(k_2^*+k_3^*)t}\cdot\int_0^t e^{(k_2^*+k_3^*)\tau}\, d\tau$$

$$\approx C_p^{*eq}(t)\cdot e^{-(k_2^*+k_3^*)t}\cdot\frac{1}{(k_2^*+k_3^*)}\Big[e^{(k_2^*+k_3^*)\tau}\Big]_0^t = C_p^{*eq}(t)\cdot e^{-(k_2^*+k_3^*)t}\cdot\frac{1}{(k_2^*+k_3^*)}\left(e^{(k_2^*+k_3^*)t}-1\right)$$

$$= C_p^{*eq}(t)\cdot\frac{1}{(k_2^*+k_3^*)} - \frac{C_p^{*eq}(t)}{(k_2^*+k_3^*)}\cdot e^{-(k_2^*+k_3^*)t} \overset{\text{if } t\to\infty \text{ for eq.}}{\approx} \frac{C_p^{*eq}(t)}{(k_2^*+k_3^*)} \qquad ⑨$$

for ②

$$\Rightarrow 1 \otimes C_p^* = \int_0^t C_p^*(\tau)\cdot 1\, d\tau = \int_0^t C_p^*(\tau)\, d\tau$$

$$\approx \int_0^t C_p^{*eq}(\tau)\, d\tau \quad \text{in eq. state of system.}$$

∴ In eq state of system.

$$\Rightarrow C^*_{measured}(t) \approx (1-V_b)\left[\frac{k_1^* k_2^*}{k_2^*+k_3^*}\cdot\frac{C_p^{*eq}(t)}{k_2^*+k_3^*} + \frac{k_1^* k_2^*}{k_2^*+k_3^*}\int_0^t C_p^{*eq}(\tau)\, d\tau\right] + V_b\cdot C_p^{*eq}(t)$$

If we devide the $C^*_{measured}(t)$ with $C_p^{*eq}(t)$, commonly called appaent distribution volume

$$\Rightarrow \frac{C^*_{measured}(t)}{C_p^{*eq}(t)} \approx (1-V_b)\left[\frac{k_1^* k_2^*}{(k_2^*+k_3^*)^2} + \frac{k_1^* k_3^*}{k_2^*+k_3^*}\cdot\frac{\int_0^t C_p^{*eq}(\tau)\, d\tau}{C_p^{*eq}(t)}\right] + V_b\cdot \cancel{C_p^{*eq}(t)}$$

← ~~Stretched~~ stretched time

= apparent ~~volume~~ dist. volume.

$\boxed{Q1}$

If we assume that $V_b = 0$ ⇒ there is no part of blood in the ROI or voxel

↳ why we have to ??

$$\Rightarrow \frac{C^*_{measured}(t)}{C_p^{*eq}(t)} \approx \frac{k_1^* k_3^*}{k_2^*+k_3^*}\cdot\frac{\int_0^t C_p^{*eq}(\tau)\, d\tau}{C_p^{*eq}(t)} + \frac{k_1^* k_2^*}{(k_2^*+k_3^*)^2}$$

$\boxed{Q2}$

what is physical meaning ?

why ??

if we define $\frac{k_1^* k_3^*}{k_2^*+k_3^*} \equiv k_i$ & $\frac{k_1^* k_2^*}{(k_2^*+k_3^*)^2} \equiv V$

(net influx rate constant) (volume of distribution)

Then, $\frac{C^*_{measured}(t)}{C_p^{*eq}(t)} \approx k_i \frac{\int_0^t C_p^{*eq}(\tau)\, d\tau}{C_p^{*eq}(t)} + V$: patlak analysis (linearization of relationship).

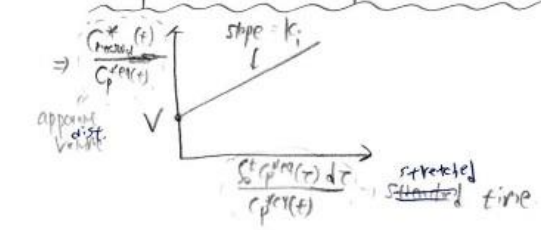

10

$$\Rightarrow \frac{C^*_{measured}(t)}{C_p^{*eq}(t)} \approx k_i \frac{\int_0^t C_p^{*eq}(\tau)\,d\tau}{C_p^{*eq}(t)} + V \quad : \text{patlak analysis}$$

$\boxed{Q3}$

If we assume that V is negligible, then

why? meaning of negligible V ?

$$\Rightarrow \frac{C^*_{measured}(t)}{C_p^{*eq}(t)} \approx k_i \frac{\int_0^t C_p^{*eq}(\tau)\,d\tau}{C_p^{*eq}(t)} \Rightarrow C^*_{measured}(t) \approx k_i \cdot \int_0^t C_p^{*eq}(\tau)\,d\tau$$

$$\therefore k_i \approx \frac{C^*_{measured}(t)}{\int_0^t C_p^{*eq}(\tau)\,d\tau}$$

If we assume that the integral of plasma input function is similar to the total injected activity per body weight W, then

$$\therefore k_i \approx \frac{C^*_{measured}(t)}{\int_0^t C_p^{*eq}(\tau)\,d\tau} \approx \frac{C^*_{measured}(t)}{A/W} \equiv SUV$$

//.

//

Appendix B: Conceptual Meaning of PGA parameters.

Conceptual Meaning of PGA parameters (regarding why $\frac{k_1^* k_2^*}{(k_2^*+k_3^*)^2} = V_i$)

(Volume of dist.)

In patlak analysis, the formula would be given as follows,

$$\frac{C^*_{measured}(t)}{C_p^{*eq}(t)} \approx \underbrace{\left(\frac{k_1^* k_2^*}{k_2^*+k_3^*}\right)}_{\text{(slope : net influx rate constant (from plasma to comp. \#2))}} \cdot \frac{\int_0^t C_p^{*eq}(\tau)\,d\tau}{C_p^{*eq}(t)} + \underbrace{\frac{k_1^* k_2^*}{(k_2^*+k_3^*)^2}}_{\text{(intercept)}}$$

But, by definition, $\frac{C^*_{measured}(t)}{C_p^{*eq}(t)}$ could be expressed as follows,

$$\Rightarrow \frac{C^*_{measured}(t)}{C_p^{*eq}(t)} = \frac{C_1^*(t)}{C_p^{*eq}(t)} + \frac{C_2^*(t)}{C_p^{*eq}(t)}$$

$$\approx \underbrace{\frac{C_1^{*eq}(t)}{C_p^{*eq}(t)}}_{\text{(contribution by comp. \#1)}} + \underbrace{\frac{C_2^*(t)}{C_p^{*eq}(t)}}_{\text{(contribution by comp \#2)}}$$

(under the assumption of k_1^* & $k_2^* \gg k_3^*$, and in eq. $\Rightarrow C_1^*(t) \approx C_1^{*eq}(t)$: almost constant)

Then, when considering the point that the slope of patlak formula means net influx rate constant (from plasma to comp. #2), conceptually it is reasonable to think that

$$\underbrace{\left(\frac{k_1^* k_2^*}{k_2^*+k_3^*}\right) \cdot \frac{\int_0^t C_p^{*eq}(\tau)\,d\tau}{C_p^{*eq}(t)} \approx \frac{C_2^*(t)}{C_p^{*eq}(t)}}_{\text{Contribution by Comp. \#2}} \quad \& \quad \underbrace{\frac{k_1^* k_2^*}{(k_2^*+k_3^*)^2} \approx \frac{C_1^{*eq}(t)}{C_p^{*eq}(t)}}_{\text{Contribution by Comp. \#1}}$$

$$\left(\because \left(\frac{k_1^* k_2^*}{k_2^*+k_3^*}\right) \cdot \int_0^t C_p^{*eq}(\tau)\,d\tau \approx C_2^*(t)\right)$$

Then, why they give the quantity $\frac{k_1^* k_2^*}{(k_2^*+k_3^*)^2}$ the physical meaning (i.e., Volume of dist.)?

⇒ To make a reasonable guess, I think we need to understand clear meaning of "Volume of dist."

Then, what is the meaning of "Volume of dist."?

In brief, it is neither a spread volume in the body nor a spread volume of ROI (or Vad)

The real meaning is a relative ratio of spread volume which has same concentration with plasma's. (to be continued)

$\Rightarrow$

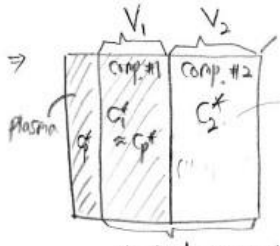

$\rightarrow C_2^* \approx 0$ (if $k_1^* \,\&\, k_2^* \gg k_3^*$)

- total volume of comp.#1 (V_1) + comp.#2 (V_2) $\equiv V_t$
- total activity in the total volume $V_t \equiv A_t$
- volume of comp.#1 $\equiv V_1$

Then, $\frac{C_1^*}{C_p^*}$ could be explessed as follows.

$$\Rightarrow \frac{C_1^*(t)}{C_p^*(t)} \approx \frac{\frac{A_t}{V_t}}{\frac{A_t}{V_1}} = \frac{V_1}{V_t}$$

$$\boxed{\therefore \frac{C_1^*(t)}{C_p^*(t)} \approx \frac{V_1}{V_t} : \text{definition of "Volume of dist."}}$$

$\Leftarrow$ (it is ratio, thus unitless!)

$\therefore$ When considering the definition of "Volume of dist.", conceptually we can roughly say that $\frac{C_1^{*m}(t)}{C_p^*(t)}$ is the volume of dist.

($\because$ actually, $C_p^*(t) \neq C_1^{*m}(t)$)

BTW, we already know that $\frac{k_1^* k_2^*}{(k_2^* + k_3^*)^2} \approx \frac{C_1^{*m}(t)}{C_p^{*m}(t)}$, conceptually.

$\therefore$ We can roughly call the quantity $\frac{k_1^* k_2^*}{(k_2^* + k_3^*)^2}$ as "Volume of dist."

(this is my rough expectation on why they give $\frac{k_1^* k_2^*}{(k_2^* + k_3^*)^2}$ the physical meaning!)

2

In brief, by conceptual study, the patlak formula could be expressed as follows.

$$\frac{C^*_{measured}(t)}{C_p^{*eq}(t)} \approx \underbrace{\frac{C_2^*(t)}{C_p^{*eq}(t)}}_{\text{by comp \#2}} + \underbrace{\frac{C_1^{*eq}(t)}{C_p^{*eq}(t)}}_{\text{by comp. \#1}}$$

$$\approx k_i \cdot \frac{\int_0^t C_p^{*eq}(\tau)\,d\tau}{C_p^{*eq}(t)} + V$$

↳ patlak formula !!

(where slope $k_i \equiv \frac{k_1^* k_2^*}{k_2^* + k_3^*}$: net influx rate constant (from plasma to comp. #2)

intercept $V \equiv \frac{k_1^* k_2^*}{(k_2^* + k_3^*)^2}$: volume of distribution)

$\boxed{\text{However}}$, mathematically, I guess the conceptual study is not correct !!

I will prove my opinion by showing that $k_i \cdot \frac{\int_0^t C_p^{*eq}(\tau)\,d\tau}{C_p^{*eq}(t)} \neq \frac{C_2^*(t)}{C_p^{*eq}(t)}$.

(In other words, $k_i \cdot \frac{\int_0^t C_p^{*eq}(\tau)\,d\tau}{C_p^{*eq}(t)}$ is a mixture of contributions of comp. #1 and #2)

<proof>

→ General sol. of reversible two tissue comp. model

$$\Rightarrow \begin{cases} C_1^*(t) = \left(\frac{k_1^*}{\alpha - \beta}\right)\left[(\alpha - k_4^*)e^{-\alpha t} - (\beta - k_4^*)e^{-\beta t}\right] \otimes C_p^* \\ C_2^*(t) = \left(\frac{k_1^* k_3^*}{\alpha - \beta}\right)\left[e^{-\beta t} - e^{-\alpha t}\right] \otimes C_p^* \\ \alpha = \frac{(k_2^* + k_3^* + k_4^*) + \sqrt{(k_2^* + k_3^* + k_4^*)^2 - 4k_2^* k_4^*}}{2} \\ \beta = \frac{(k_2^* + k_3^* + k_4^*) - \sqrt{(k_2^* + k_3^* + k_4^*)^2 - 4k_2^* k_4^*}}{2} \end{cases}$$

But, we want the case $k_4^* = 0$ (irreversible comp. #2)

$\therefore \begin{cases} \alpha = k_2^* + k_3^* \\ \beta = 0 \end{cases} \Rightarrow$ In this case,

$$\boxed{\begin{aligned} C^*_{1|k_4^*=0}(t) &= \frac{k_1^*}{k_2^* + k_3^*}\left[(k_2^* + k_3^*)e^{-(k_2^* + k_3^*)t}\right] \otimes C_p^* \\ C^*_{2|k_4^*=0}(t) &= \frac{k_1^* k_3^*}{k_2^* + k_3^*}\left[1 - e^{-(k_2^* + k_3^*)t}\right] \otimes C_p^* \end{aligned}}$$

(Sol. of the case $k_4^* = 0$)

we allready know the approximated formulas of these

$$\left\{ \begin{array}{l} e^{-(k_2^*+k_3^*)t} \otimes C_p^* \approx \dfrac{C_p^{*eq}(t)}{(k_2^*+k_3^*)} \\ 1 \otimes C_p^* \approx \int_0^t C_p^{*eq}(\tau)\, d\tau \end{array} \right\}$$

in almost eq. state of system (between plasma & comp. #1)

⇒ Then,

$$C^*_{1\_k_4^*=0}(t) = k_1^* e^{-(k_2^*+k_3^*)t} \otimes C_p^*$$

$$\approx k_1^* \frac{C_p^{*eq}(t)}{(k_2^*+k_3^*)} = \frac{k_1^*}{k_2^*+k_3^*} C_p^{*eq}(t)$$

$$C^*_{2\_k_4^*=0}(t) = \frac{k_1^* k_3^*}{k_2^*+k_3^*}\left[1 - e^{-(k_2^*+k_3^*)t}\right] \otimes C_p^*$$

$$= \frac{k_1^* k_3^*}{k_2^*+k_3^*}\left[1 \otimes C_p^* - e^{-(k_2^*+k_3^*)t} \otimes C_p^*\right]$$

$$\approx \frac{k_1^* k_3^*}{k_2^*+k_3^*}\left[\int_0^t C_p^{*eq}(\tau)\, d\tau - \frac{C_p^{*eq}(t)}{(k_2^*+k_3^*)}\right]$$

$$\approx \frac{k_1^* k_3^*}{k_2^*+k_3^*}\int_0^t C_p^{*eq}(\tau)\, d\tau - \frac{k_1^* k_3^*}{(k_2^*+k_3^*)^2} C_p^{*eq}(t)$$

By mathematical study

$$\therefore \boxed{\begin{array}{l} \dfrac{C^*_{1\_k_4^*=0}(t)}{C_p^{*eq}(t)} \approx \dfrac{k_1^*}{k_2^*+k_3^*} \\ \dfrac{C^*_{2\_k_4^*=0}(t)}{C_p^{*eq}(t)} \approx \dfrac{k_1^* k_3^*}{k_2^*+k_3^*} \cdot \dfrac{\int_0^t C_p^{*eq}(\tau)\, d\tau}{C_p^{*eq}(t)} - \dfrac{k_1^* k_3^*}{(k_2^*+k_3^*)^2} \end{array}}$$

another term

But, in our previous conceptual study

$$\frac{C^*_{2\_k_4^*=0}(t)}{C_p^{*eq}(t)} \approx \frac{k_1^* k_3^*}{k_2^*+k_3^*} \cdot \frac{\int_0^t C_p^{*eq}(\tau)\, d\tau}{C_p^{*eq}(t)}$$

⇒ there is difference!! logically

∴ the conceptual study is understandable, but strictly speaking mathematically it is not correct!!

4